An Updated High Precision Measurement of the Neutral Pion Lifetime via the Primakoff Effect

December 10, 2007

THIS ALL NEEDS TO BE UPDATED

Brazilians, new Kharkov people, Bitao

A. Ahmidouch, S. Danagoulian (spokesperson),
A. Gasparian (spokesperson and contact person), C. Jackson, S. Mtingwa, J. Underwood
North Carolina A&T State University, Greensboro, NC

E. Clinton, R. Hicks, D. Lawrence, R. Miskimen (spokesperson)
University of Massachusetts, Amherst, MA

D. Dale (spokesperson), M. Gabrielyan, B. Hu, W. Korsch, A. Teymurazyan, P. Zolnierczuk
University of Kentucky, Lexington, KY

A. Afanasev, E. Chudakoff, H. Egiyan, R. Ent, V. Gyurjyan, M. Ito, J.P. Chen,
Y. Sharabian, E. Smith
Thomas Jefferson National Accelerator Facility, Newport News, VA

K. Baker, M. Christy, J. Goity, P. Gueye, C. Keppel, L. Tang, L. Yuan
Hampton University, Hampton, VA

L. Gan, M. Alexanian, T. Black
University of North Carolina at Wilmington, Wilmington, NC

A.M. Bernstein, D. Hasell, S. Kowalski, R. Suleiman
Massachusetts Institute of Technology, Cambridge, MA

D. Sober, H. Crannell, R. Hakobyan
The Catholic University of America, Washington, DC

J. Ball, M. Dugger, E. Pasyuk, B.G. Ritchie
Arizona State University, Tempe, AZ

R. Minehart, B. Stevens
University of Virginia, Charlottesville, VA

A. Asratyan, O. Chernyshov, G. Davidenko, A. Dolgolenko, G. Dzyubenko, A. Evdokimov,
V. Goryachev, A. Kamenskii, M. Kubantsev, I. Larin, V. Matveev, V. Semyachkin,
A. Sitnikov, V. Verebryusov, V. Vishnyakov
Institute for Theoretical and Experimental Physics, Moscow, Russia

Yu. Goncharenko, V. Kubarovsky, A. Meschanin, L. Soloviev, A. Vasiliev
Institute for High Energy Physics, Protvino, Russia

M. Khandaker, V. Punjabi, C. Salgado
Norfolk State University, Norfolk, VA

A. Glamazdin, A. Omelaenko, ++++++++
Kharkov Institute of Physics and Technology, Kharkov, Ukraine

P.L. Cole
University of Texas at El Paso, El Paso, TX

A. Nathan
University of Illinois, Urbana, IL

C. Li, Z. Liu, S. Lu, J. Yuan, J. Zhou, S. Zhou, X. Zhu
Chinese Institute of Atomic Energy, Beijing, China

J. He
Institute of High Energy Physics, Chinese Academy of Sciences, Beijing, China

W. Briscoe
George Washington University, Washington, DC

I. Aznauryan, S. Gevorgyan, A. Margaryan, K. Egiyan,
H. Voskanyan, A. Ketikyan, A. Shahinyan, A. Petrosyan
Yerevan Physics Institute, Yerevan, Armenia

B. Milbrath
Eastern Kentucky University, Richmond, KY

A.I. Fix, V.A. Tryasuchev
Tomsk Polytechnical University, Tomsk, Russia

M. Elaasar
Southern University at New Orleans, New Orleans, LA

Contents

Abstract

The PrimEx Collaboration has proposed to perform a high precision measurement on the two photon decay width of the neutral pion ($\Gamma_{\pi^0\to\gamma\gamma}$). This measurement will provide a stringent test of the predictions of the U(1) axial anomaly in quantum chromodynamics. The first experimental data set was collected in 2004. A new level of experimental precision has been achieved by using a high intensity and high resolution photon tagging facility in Hall B of Jefferson Lab, and by developing and constructing a state-of-the-art, high resolution electromagnetic calorimeter. A preliminary result on the π^0 lifetime with a precision of $\sim 3\%$ was released at the American Physical Society April meeting in 2007 through an invited presentation as well as at an American Institute of Physics press conference. The desired precision on this measurement is driven by the precision of recently available theoretical calculations performed both in the context of chiral perturbation theory and the QCD sum rule approach. Here, we discuss the analysis status on the existing data and the improvement which can be made with a future run, and thereby request an extension of the π^0 lifetime measurement from PAC 33 to reach the ultimate goal of $\simeq$1.4% accuracy.

1 Motivation

An effect of color confinement in quantum chromodynamics (QCD) is that traditional perturbation theory breaks down at large distances and low energies. A quantitative understanding of the strong interaction in this region remains one of the greatest intellectual challenges in physics. Symmetries of QCD in the chiral limit (massless quark limit) provide a promising framework for resolving this problem. As the lightest particle in the hadron spectrum, the neutral pion represents the most sensitive platform to study fundamental symmetry issues in quantum chromodynamics at low energy. Spontaneous chiral symmetry breaking gives birth to the π^0 as one of the Goldstone particles and the chiral axial anomaly primarily determines the π^0 lifetime. As such, a precision measurement of the lifetime of the π^0 will provide a fundamental test of QCD at the confinement scale.

2 Theoretical Developments

The two-photon decay mode of the π^0 reveals one of the most profound symmetry issues in quantum chromodynamics, namely, the explicit breaking of a classical symmetry by the quantum fluctuations of the quark fields coupling to a gauge field[1]. This phenomenon, called anomalous symmetry breaking, is of pure quantum mechanical origin. In QCD, there are several observable phenomena that originate from anomalies. One is connected with the couplings of the quarks to the gluons. This is the so called axial anomaly by which the conservation of the axial U(1) symmetry of the classical Lagrangian of QCD is broken even in the limit where two or more quarks are massless, and the so called anomalous divergence of the corresponding axial-vector current becomes proportional to the product $\vec{E}^a \cdot \vec{B}^a$ of the chromo-electric and chromo-magnetic fields. The axial anomaly of interest to us involves the corresponding coupling of the quarks to photons[2]. In the limit of exact isospin symmetry, the π^o couples only to the isotriplet axial-vector current $\bar{q} I_3 \gamma_\mu \gamma_5 q$, where $q = (u,\ d)$, and I_3 is the third isospin generator. If we limit ourselves to two quark flavors, the electromagnetic current is given by $\bar{q}(1/6 + I_3/2)\gamma_\mu q$. When coupling to the photon, the isosinglet and isotriplet components of the electromagnetic current lead to an anomaly that explicitly breaks the symmetry associated with the axial-vector current $\bar{q}\ I_3\ \gamma_\mu \gamma_5\ q$, and this in turn directly affects the coupling of the π^o to two photons. The conservation of the axial U(1) current, to which the η' meson couples, as well as the $\bar{q}\frac{1}{2}\lambda_8 \gamma_\mu \gamma_5 q$, to which the η meson couples, are similarly affected by the electromagnetic field.

In the limit of vanishing quark masses, the anomaly leads to the $\pi^0 \to \gamma\gamma$ decay amplitude [1, 2]:

$$\mathcal{A}(\pi^0 \to \gamma\gamma) = \frac{\alpha_{em}}{4\pi F_\pi} \epsilon_{\mu\nu\rho\sigma} k^\mu k'^\nu \epsilon^{*\rho} \epsilon^{*\sigma}, \tag{1}$$

or the reduced amplitude,

$$A_{\gamma\gamma} = \frac{\alpha_{em}}{\pi F_\pi} = 2.513 \cdot 10^{-2} GeV^{-1} \tag{2}$$

where $F_\pi = 92.42 \pm 0.25 MeV$ [3] is the pion decay constant, and k and ϵ are respectively photon momenta and polarization vectors.

The width of the $\pi^o \to \gamma\gamma$ decay predicted by this amplitude is

$$\Gamma = M_\pi^3 \frac{|A_{\gamma\gamma}|^2}{64\pi} = 7.725 \pm 0.044 eV, \tag{3}$$

with a 0.6% uncertainty due to the experimental error in F_π. The crucial aspect of this expression is that it has no free parameters that need to be determined phenomenologically. In addition, since the mass of the π^0 is the smallest in the hadron spectrum, higher order corrections to this prediction are small and can be calculated with a sub-percent accuracy.

The current experimental value is 7.84 ± 0.56 eV[3] and is in good agreement with the predicted value with the chiral limit amplitude. This number is an average of several experiments[3] which are discussed in Appendix I. The error of 7% quoted by the Particle Data Book is most likely too low since each of the quoted experiments appears to have understated their errors and also, as can be seen in figure 1, from the much larger dispersion between the different measurements. Even at the 7% level, the accuracy is not sufficient for a test of such a fundamental quantity, and in particular for the new calculations which take the finite quark masses into account. The level of precision of $\simeq 1.4\%$, which is the goal of *PrimEx*, will satisfy these requirements.

The decay amplitude given above is exact only in the chiral limit, *i.e.*, when the $u-$ and $d-$quark masses vanish. In this case, the anomaly is saturated by the π^o pole and the result for the decay amplitude given above is exact. However, the current-quark masses are non-vanishing and are approximately $m_u \simeq 4MeV$ and $m_d \simeq 7MeV$[6]. There are two sources of corrections due to this explicit breaking of chiral symmetry. The first and dominant one results from a combined effect that involves the corrections to the decay constants (because of isospin breaking there is a decay constant matrix in the subspace of the π^0, η and η') and an isospin breaking mixing that gives the physical π^0 a non-vanishing component along the pure U(3) states η and η'. In the absence of isospin breaking this source of chiral symmetry breaking boils down to merely replacing the value of F_π in the chiral limit by the measured value determined from π^+ decay[4, 5]. The second source of corrections is due to the fact that the saturation of the matrix elements of the divergence of the axial current also involves excited mesonic states when chiral symmetry is broken by quark masses. This effect is estimated using QCD sum rules[11] and turns out to be much smaller than the mixing effects.

Stimulated by the *PrimEx* project, several new theoretical calculations have been published in recent years, and are shown in figure1. The first two independent calculations of the chiral corrections have been performed in the combined framework of chiral perturbation theory (ChPT) and the $1/N_c$ expansion up to $\mathcal{O}(p^6)$ and $\mathcal{O}(p^4 \times 1/N_c)$ in the decay amplitude[7][8]. The η' is explicitly included in the analysis as it plays as important a role as the η in the mixing effects. It was found that the decay width is enhanced by about 4% with respect to the value stated in equation (1). This enhancement is almost entirely due to the mixing effects. The result of this next-to-leading order analysis is $\Gamma_{\pi^o \to \gamma\gamma} = 8.10$ eV with an estimated uncertainty of less than 1%. Another theoretical calculation based on QCD sum rules[9], also inspired by the *PrimEx* experiment, has recently been published with a theoretical uncertainty less than 1.5%. Here, the only input parameter to the calculation is the eta width. The measurement of the decay width of π^0 with a comparable precision will provide an important test of the fundamental QCD predictions.

The proposed measurement at the $\simeq$1.4% accuracy level fills an important experimental gap, namely a precision verification of the predictions of the axial anomaly and the chiral corrections to the decay rate. The so-called "direct" method of determination of $\Gamma_{\pi^0\to\gamma\gamma}$ lies below the prediction of the axial anomaly[14] and is therefore even more in disagreement with the new predictions which are based on both next-to-leading order chiral theory[7][8] and QCD sum rules[9]. This makes the *PrimEx* experiment even more compelling. It is indeed extremely important that effects of chiral symmetry breaking by the $u-$ and $d-$quark masses, which can be rather precisely predicted theoretically, can actually be experimentally tested thanks to the projected level of precision of *PrimEx*. This would indeed be one of the most precise tests of fundamental aspects of QCD, namely anomalies and chiral symmetry breaking by quark masses, ever achieved.

3 Neutral Pion Photoproduction via the Primakoff Effect

We plan to use quasi-monochromatic photons of energy 4.6-5.7 GeV from the Hall B photon tagging facility to measure the absolute cross section of small angle π^o photoproduction from the Coulomb field of complex nuclei. The invariant mass and angle of the pion will be reconstructed by detecting the π^o decay photons from the $\pi^o\to\gamma\gamma$ reaction.

For unpolarized photons, the Primakoff cross section is given by[43]:

$$\frac{d^3\sigma_P}{d\Omega} = \Gamma_{\gamma\gamma}\frac{8\alpha Z^2}{m^3}\frac{\beta^3 E^4}{Q^4}|F_{e.m.}(Q)|^2 sin^2\theta_\pi \tag{4}$$

where $\Gamma_{\gamma\gamma}$ is the pion decay width, Z is the atomic number, m, β, θ_π are the mass, velocity and production angle of the pion, E is the energy of incoming photon, Q is the momentum transfer to the nucleus, and $F_{e.m.}(Q)$ is the nuclear electromagnetic form factor, corrected for final state interactions of the outgoing pion.

As the Primakoff effect is not the only mechanism for pion photoproduction at high energies, some care must be taken to isolate it from competing processes. In particular, the full cross section is given by:

$$\frac{d^3\sigma}{d\Omega_\pi} = \frac{d\sigma_P}{d\Omega} + \frac{d\sigma_C}{d\Omega} + \frac{d\sigma_I}{d\Omega} + 2\cdot\sqrt{\frac{d\sigma_P}{d\Omega}\cdot\frac{d\sigma_C}{d\Omega}}cos(\phi_1+\phi_2) \tag{5}$$

where the Primakoff cross section, $\frac{d\sigma_P}{d\Omega}$, is given by equation (4). The nuclear coherent cross section is given by:

$$\frac{d\sigma_C}{d\Omega} = C\cdot A^2|F_N(Q)|^2 sin^2\theta_\pi \tag{6}$$

and the incoherent cross section is:

$$\frac{d\sigma_I}{d\Omega} = \xi A(1-G(Q))\frac{d\sigma_H}{d\Omega} \tag{7}$$

where A is the nucleon number, $Csin^2\theta_\pi$ is the square of the isospin and spin independent part of the neutral meson photoproduction amplitude on a single nucleon, $|F_N(Q)|$ is the

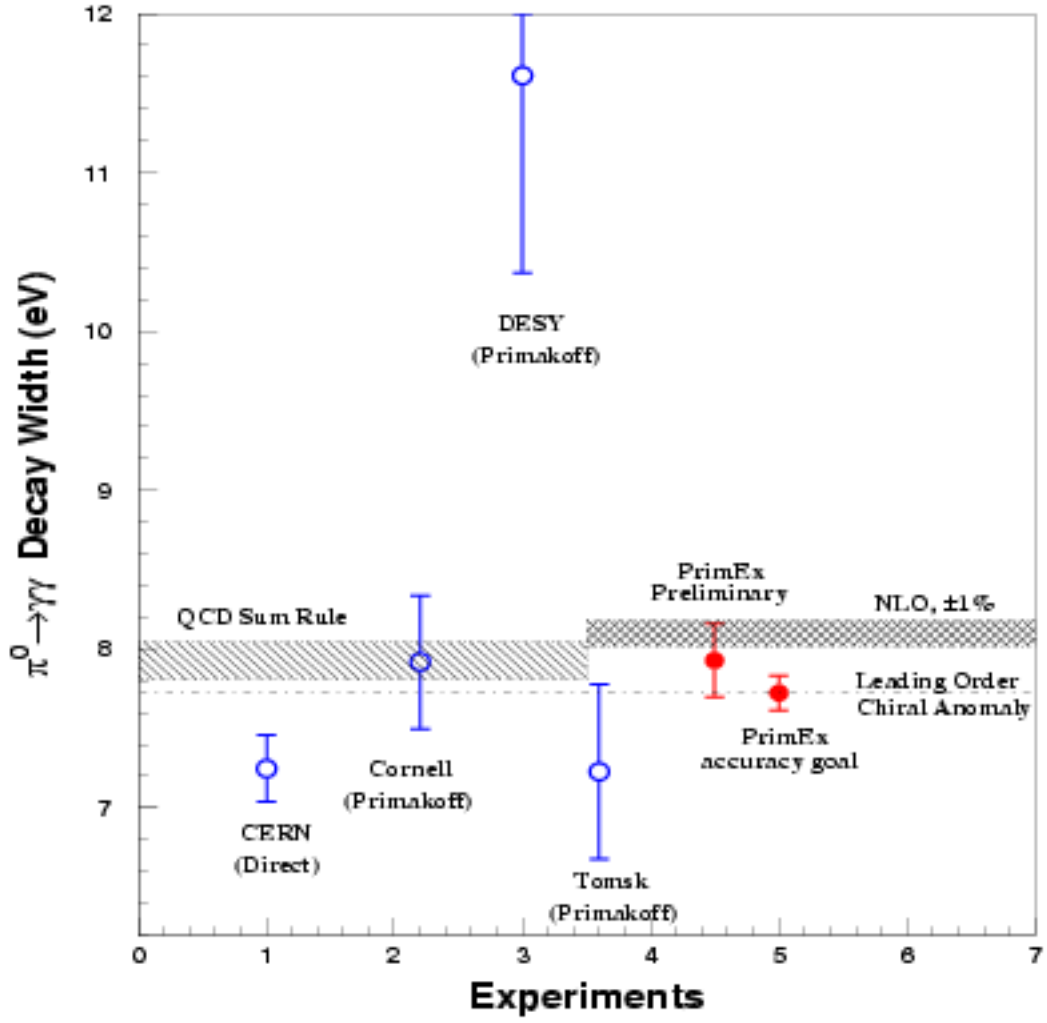

Figure 1: $\pi^o \to \gamma\gamma$ decay width in eV. The dashed horizontal line is the leading order prediction of the axial anomaly (equation 3)[1, 2].The left hand side shaded band is the recent QCD sum rule prediction and the right hand side shaded band is the next-to-leading order chiral theory predictions. The experimental results with errors are for : (1) the direct method[14]; (2, 3, 4) the Primakoff method [44, 43, 18]; (5) the preliminary result from the first *PrimEx* data set; (6) the expected error for the final goal of the *PrimEx* experiment, arbitrarily plotted to agree with the leading order prediction.

form factor for the nuclear matter distribution in the nucleus, (corrected for final state interactions of the outgoing pion), ξ is the absorption factor of the incoherently produced pions, $1 - G(Q)$ is a factor which reduces the cross section at small momentum transfer due to the Pauli exclusion principle, and $\frac{d\sigma_N}{d\Omega}$ is the π^o photoproduction cross section on a single nucleon. The relative phase between the Primakoff and nuclear coherent amplitudes without final state interactions is given by ϕ_1, and the phase shift of the outgoing pion due to final state interactions is given by ϕ_2.

Kinematical considerations enable one to separate the Primakoff effect from other photo-pion production mechanisms. The Primakoff cross section is zero for pions emitted along the incident photon direction, has a sharp maximum at an angle $\theta_\pi \sim m_\pi^2/2E_\pi^2$, and falls rapidly to zero at larger angles. It is proportional to Z^2, and its peak value is roughly proportional to E^4. The nuclear coherent cross section for spin zero nuclei is also zero in the forward direction, but has a broad maximum outside the angular region of the Primakoff effect, and falls at larger angles as shown in figure 2, where the amplitudes are normalized to the Cornell data[44], and distortion effects are included. The angular dependence of Primakoff signal is different from the background processes, allowing $\Gamma(\pi^0 \rightarrow \gamma\gamma)$ to be extracted from a fit to the angular distribution of photo-produced π^0. Measurements of the nuclear effects at larger angles are necessary to determine the unknown parameters in the production mechanism and thus make an empirical determination of the nuclear contribution in the Primakoff peak region. Consequently, this experiment requires a π^o detector with good angular resolution to eliminate nuclear coherent production, and good energy resolution in the decay photon detection will enable an invariant mass cut to suppress multi-photon backgrounds.

The production of neutral pions via the Primakoff effect is primarily an electromagnetic phenomenon and, therefore, can be accurately calculated. The main features of the Primakoff effect listed above will be used to test the accuracy of our data: (1) We will take data with sufficient angular resolution to check the shape of the Primakoff peak after the coherent nuclear and nuclear-Primakoff interference amplitudes, which will be determined empirically by larger angle data, have been subtracted; (2) two spin zero targets (^{12}C, ^{208}Pb) will be used. These have form factors which have been well studied by electron scattering experiments, and can be used to test the Z^2 dependence of the cross section; and (3) the E^4 dependence of the peak cross section will be measured in the energy range from 4.6 to 5.7 GeV. The study of the Primakoff peak as a function of these three variables should add a great deal of confidence to the measurement, and can be used to empirically determine the systematic errors.

We submitted our first proposal(E-99-014) to PAC15 in Dec 1998. It was approved by PAC15 and reconfirmed in jeopardy review later by PAC22 with an "A" rating. The first experiment on two targets (^{12}C and ^{208}Pb) was performed in 2004. The preliminary result demonstrates that we are able to control the systematic errors with designed precision and more beam time is needed to reach the proposed goal of $\sim 1.4\%$ accuracy. In the following sections, we will describe what we have achieved in the first *PrimEx* experiment and what we can improve in the future runs.

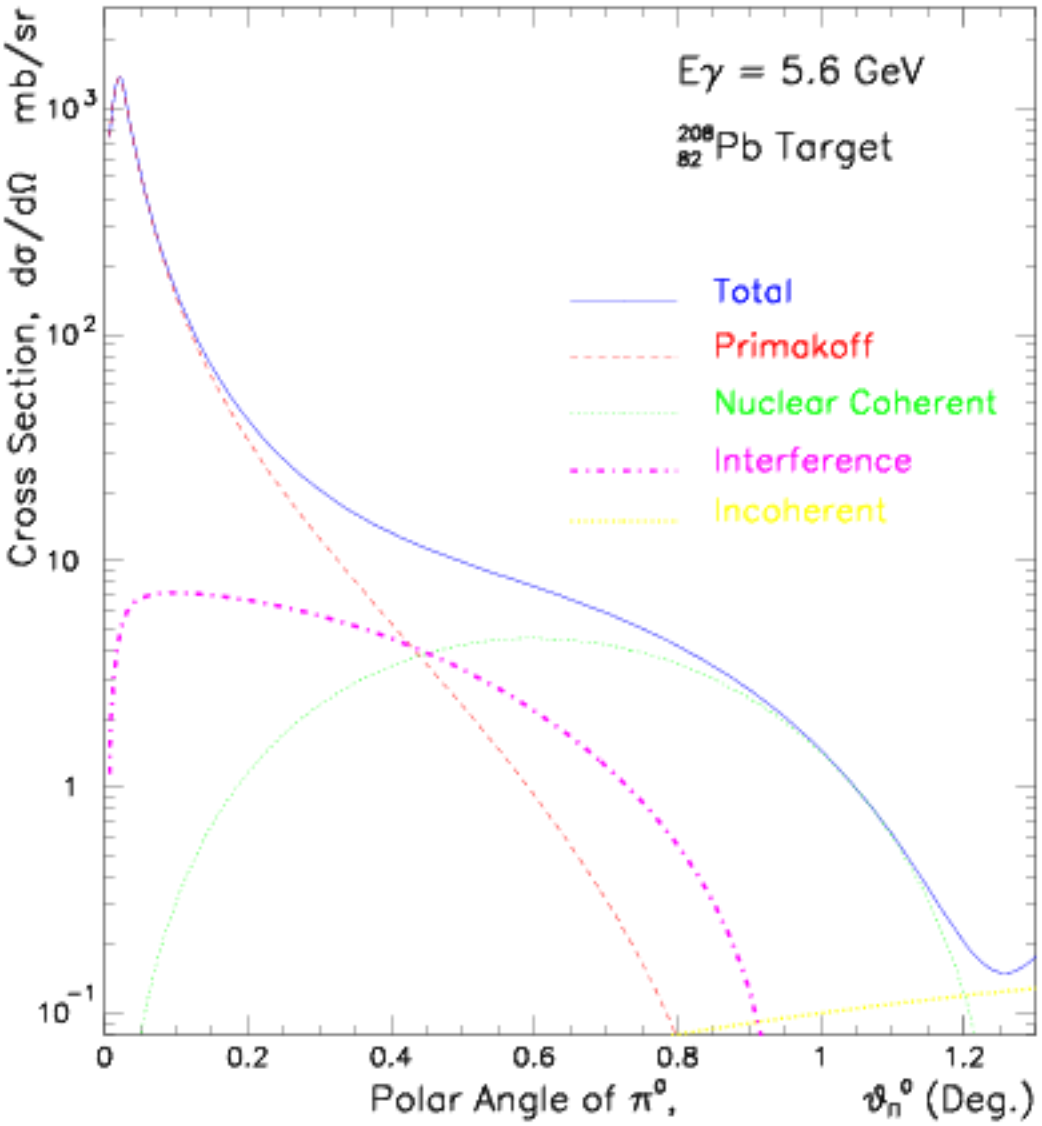

Figure 2: Angular behavior of the electromagnetic and nuclear π^o photoproduction cross sections for ^{208}Pb in the 6.0 GeV energy range.

4 Instrumentation and Experimental Techniques – Current Status and Planned Upgrades

With strong support from Jefferson Lab and a $1 million Major Research Instrumentation award (MRI, PHY-0079840) from the National Science Foundation, the *PrimEx* experimental setup was developed and constructed (See figure 3). The primary experimental equipment includes: (1) the existing Hall B photon tagger for tagged photon beam; and new development of (2) 5% radiation length solid π^o production targets (^{12}C, and ^{208}Pb); (3) a pair production luminosity monitor located just downstream of the π^o production target; (4) a 1m $\times$ 1m high resolution hybrid calorimeter (HYCAL) with a plastic scintillator charged particle veto for detecting π^0 decay photons; (5) a scintillator fiber based photon beam profile and position detector located behind HYCAL for on-line beam position monitor. Here, we describe the performance of this equipment during the first PrimEx run in 2004.

4.1 Targets

We propose to use two targets in this experiment, ^{12}C and ^{208}Pb. The carbon target is approximately 380 mil thick (5% R.L.) and uses Highly Ordered/Oriented Pyrolitic Graphite (HOPG) as the target material. The lead target is a rolled metal target approximately 12 mils thick (5% R.L.) and uses 99% enriched ^{208}Pb as the target material. The uncertainties in the effective areal densities of the carbon and lead targets are 0.05% and 0.43%, respectively. Both targets were utilized in the first *PrimEx* run. The methodology for mapping the effective areal densities of the targets ($atoms/cm^2$) and the estimated errors are described in an Appendix to this proposal.

4.2 The neutral pion detector

4.2.1 Charged particle veto detector

The veto counter system consists of twelve scintillation paddles with dimensions $120 \times 10 \times 0.5cm^3$ which cover the front face of the HYCAL calorimeter. The purpose of the veto counters is to reject charged particle backgrounds incident on the calorimeter. They are designed to have good efficiency for charged particle detection, and be sufficiently thin so that the probability for photon conversion in the paddles is small. Light is collected from both ends of the paddles using XP2262B PMTs from Photonis and tube bases from Vorg Electronics. The time difference between flight times to the two PMTs is used find the longitudinal coordinate (y) of the hit. The counters were wrapped with an inner layer of Tyvek, and an outer layer of black Tedlar. During the first *PrimEx* run, the PMT gains were matched using special runs where e^+e^- pairs produced at the target were swept into the veto paddles by the pair spectrometer magnet, and we propose to take similar data during our next run. The time-walk effects due to varying signal sizes were observable, but were found to be small and had little effect on the y-position resolution. The veto y-positions, which were calculated from the time difference between the top and bottom PMTs, were calibrated against the hit positions given by HYCAL. The average resolution was determined to be

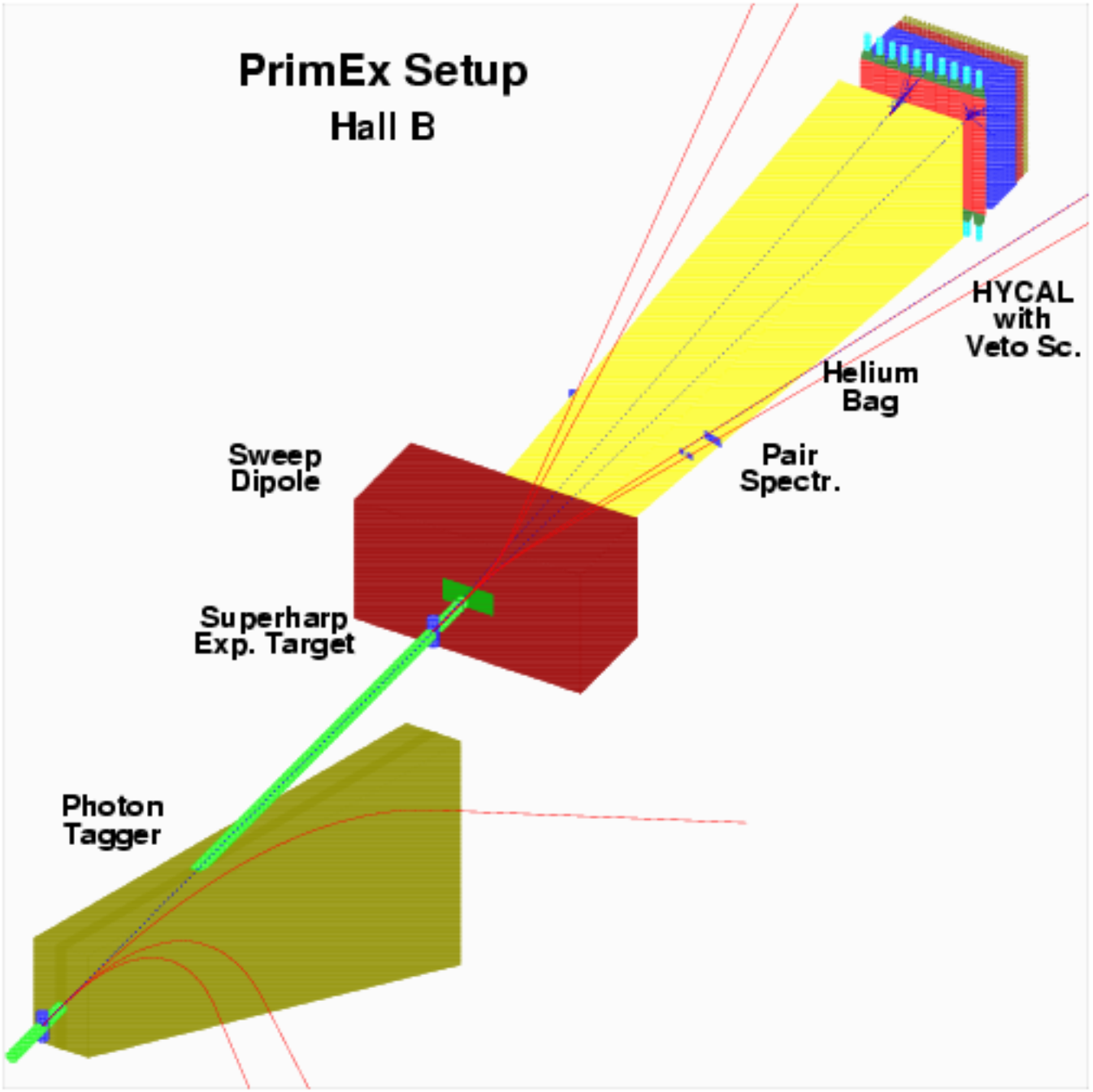

Figure 3: Layout of the *PrimEx* experimental setup.

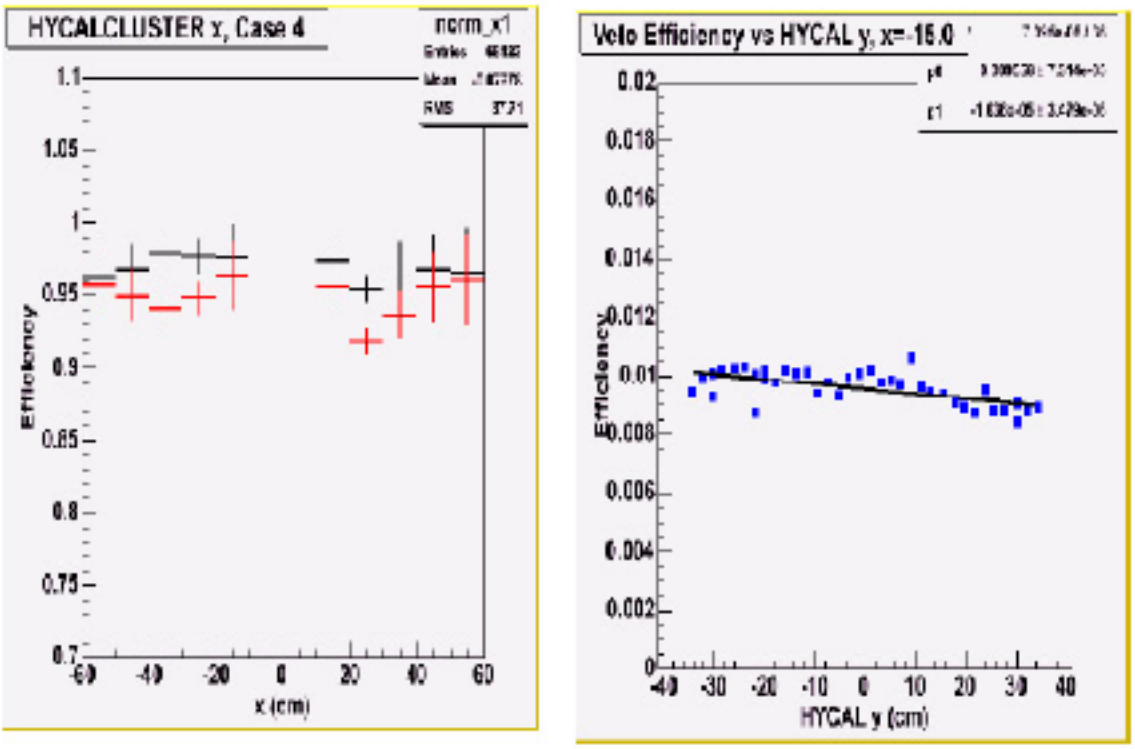

Figure 4: *Left* Charged particle detection efficiency. The black points are from matching the veto counters with HYCAL by x position and timing. The red data have additional matching in y position. *Right* Neutral particle misidentification probability for veto counter centered at $x = -15cm$ as a function of y. The black line is a linear fit.

$\pm 4.5cm$, which is within the tolerance of the experiment and corresponds to the width of the counters.

The pair production runs were also analyzed for the charged-particle efficiency. The efficiencies were determined by dividing the number of particles detected by a veto counter by the number of particles detected in the region of HYCAL covered by the acceptance of the given veto. Figure 4 shows that the charged-particle efficiency for the veto counters is approximately 95%. For the neutral misidentification analysis, data with low intensity photon beams incident on each veto counter were utilized. Figure 5 (left) shows the neutral misidentification probability for the counter at $x = -15cm$ *versus* the y-position given by HYCAL. The plot shows that the conversion probability is low ($\sim$ 1%) and constant over the length of the counter. The other eleven counters show similar results.

Figure 5 (right) presents "hybrid" mass distributions taken during the 2004 run with the veto cut not applied, and then applied. The hybrid mass is closely related to the two-photon invariant mass distribution, and includes information on the elasticity of the event. In applying the veto cut, there was a requirement that the veto x-y coordinate should match the hit position in HYCAL, and also that there is a timing correlation between the veto counter and HYCAL. The plots are at π° angles which range from the Primakoff peak to

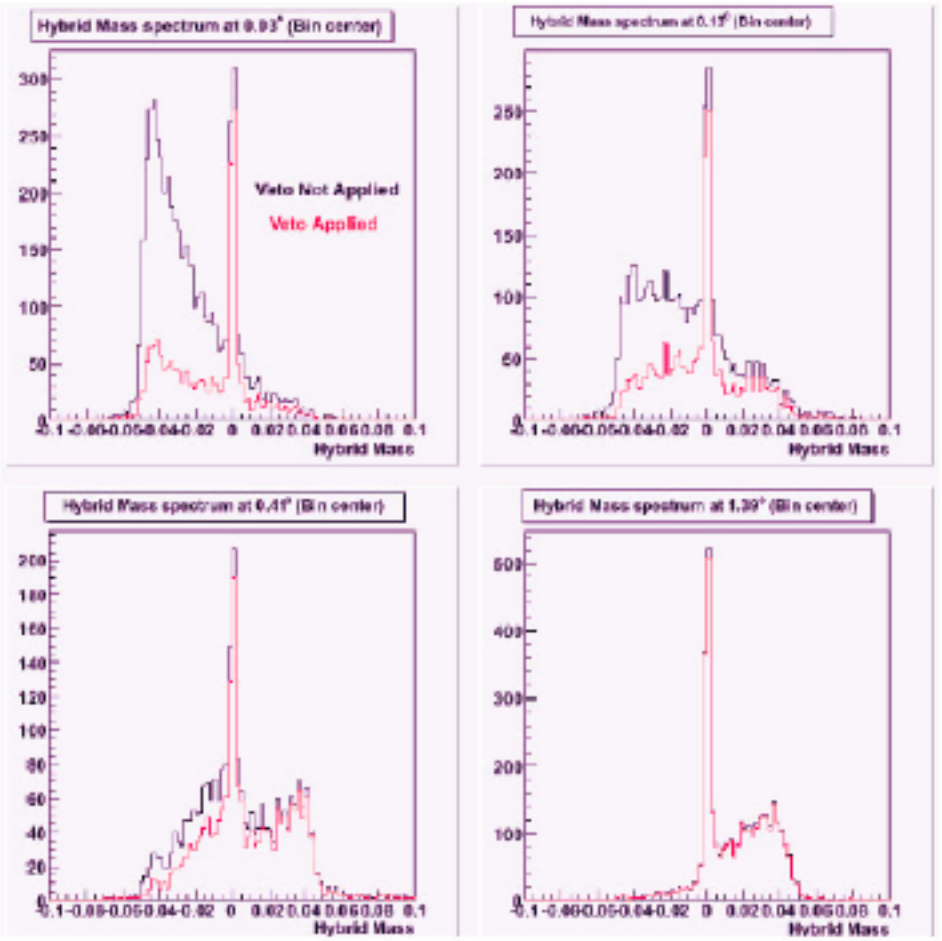

Figure 5: Hybrid mass spectra at angles of 0.03, 0.13, 0.41, and 1.39 degrees without a veto cut (black), and with a veto cut (red).

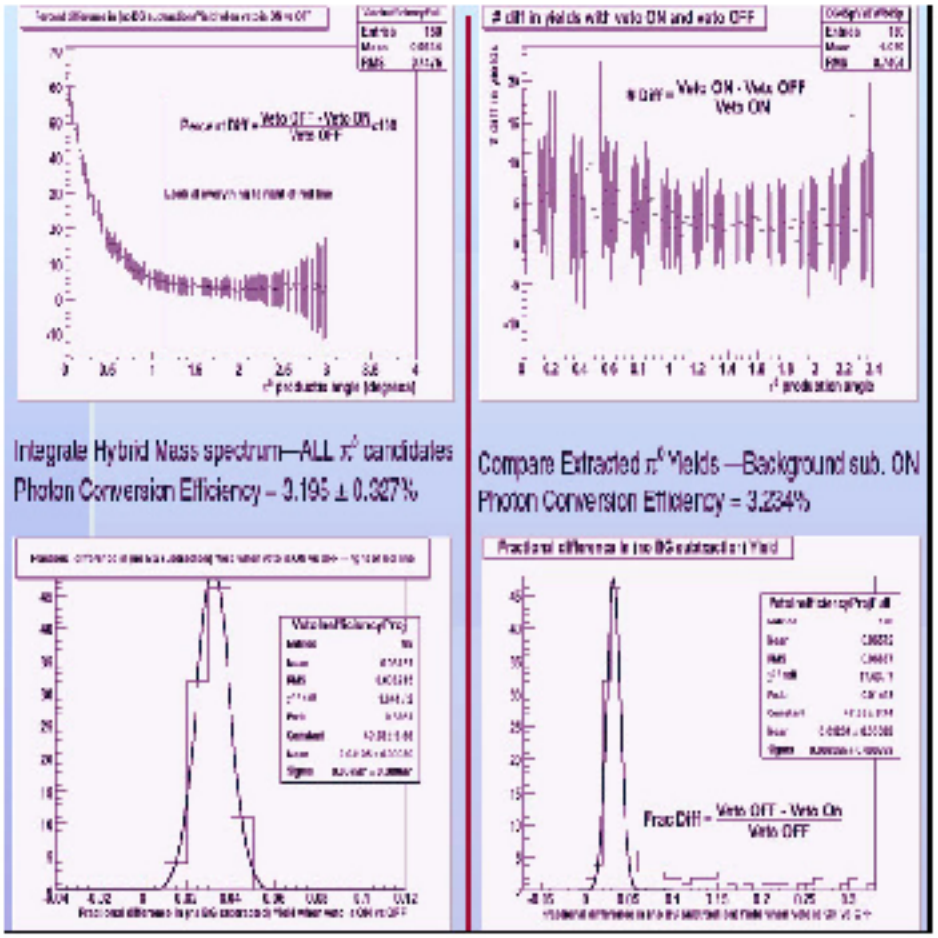

Figure 6: Measuring the veto counter photon conversion efficiency for π^o events.

the nuclear coherent region. The figure shows there is a very significant reduction in the background under the π^o mass peak when the veto cut is applied at low angles.

In our π^o analysis effort to date, we have used a global average derived from the π^o analysis to account for photon conversion in the veto counters. We have investigated two methods for obtaining a global average from the data. The first involves integrating the hybrid mass distributions, examples of which are shown in figure 5, without and with the veto cut applied. The percent deviation with the veto cut applied is plotted as a function of angle in the top-left plot of figure 6. Note that figure 5 indicates the veto has a progressively weaker effect on the hybrid mass distributions, and this is borne out in the top-left plot of figure 6, where the veto "effect" asymptotically approaches 3.20% at large angles. The second approach to fixing the average effect of photon conversion involves finding the number of events in the hybrid mass peaks without and with the veto cut applied. The percentage difference as a function of angle is plotted on the top-right plot of figure 6, and those data points are summed into a histogram on the bottom-right plot of figure 6. From this distribution, the average veto conversion effect on the π^o analysis is estimated at 3.23%, which is in good agreement with method #1.

4.2.2 The hybrid electromagnetic calorimeter *HYCAL*

At the incident photon energies of this experiment ($E_\gamma = 4.6 - 5.7$ GeV), the Primakoff cross section peaks at extremely small angles ($\theta_{peak} \simeq 0.02°$). Therefore, in order to identify and extract the Primakoff amplitude, the experimental setup must have sufficient angular resolution for detecting forward produced pions. The pions are identified by detecting the decay photons ($\pi^0 \rightarrow \gamma\gamma$) in the multi-channel electromagnetic calorimeter. Good invariant mass resolution in the $\gamma\gamma$ system is also required for the selection of pions from the experimental background. These kinematical variables have strong dependence on both the position and energy measurement accuracies of the calorimeter. In addition, the kinematical constraints imposed by the knowledge of the initial photon energy provided by the tagging system results in a significant improvement of the angular resolution and invariant mass. The combination of the photon tagging facility and high resolution calorimetry is one of the important advantages of our experiment over the previous Primakoff type of experiments. It provides significantly improved invariant mass resolution, which is important for the clean identification of photoproduced pions and high resolution in production angle to extract the Primakoff amplitude from the competing background nuclear processes. A precision experiment also requires a large geometrical coverage for the decay photons. At these energies, in order to detect 70% of the events the calorimeter must have over $1 \times 1\ m^2$ cross-sectional size at a distance of 7 m from the production target. To optimize cost and performance, we have made a decision to construct a hybrid type of calorimeter combining traditional lead glass shower detectors and newly developed high resolution $PbWO_4$ crystal scintillators. The lead glass part of the calorimeter was made of TF-1 GAMS-type Cherenkov detectors ($3.82 \times 3.82 \times 45.0$ cm^3 in size) and was provided by our collaborators from IHEP, Protvino Russia. Each lead glass was wrapped in aluminized Mylar and viewed with FEU-84 PMT's. These detectors have been used in many other experiments and their characteristics are well understood. They provide stable performance with a moderate resolutions in both position and energy. For the high resolution crystal part of the calorimeter we have done extensive R&D work to select the crystal type, the manufacturer and the detector structure. In the past few decades, $PbWO_4$ has became a popular inorganic scintillator material for precision and compact electromagnetic calorimetry in high and medium energy physics experiments. The performance characteristics of the $PbWO_4$ crystals before our beam tests had been well known mostly for high energies (>10 GeV)[28] and at energies below one GeV[29]. In order to check the performance of the crystals at the few GeV region and to select the manufacturer, we carried out beam tests with a 6×6 prototype detector consisting of crystals from two different manufacturers: Bogoroditsk (BTCP), Russia and Shanghai (SIC), China. The upper 3×6 section of the detector was assembled from crystals made in Russia, and the bottom section consists of Chinese crystals from SIC. The scintillation light from the electromagnetic shower was detected with Hamamatsu R4125HA photomultiplier tubes coupled to the back of the crystals with optical grease. The prototype detector was moved by remote control in two dimensions perpendicular to the secondary electrons, which were selected by the *PrimEx*/Hall B dipole magnet and the scintillating telescopes. An x and y coordinate scintillation fiber detector (2 mm in fiber size) was used in front of the detector to define the impact points of the electrons. The performance of the crystal prototype was studied with secondary electrons with energies from $E_e = 2$ to 4 GeV. Results on energy and position res-

olution, and the dependence of crystal detector response on radiation rate were presented at the Calor-2002 International Conference[31]. We have procured 1250 crystal modules from SIC based on the high performance they exhibited in these tests as well as the comparatively lower price per crystal, which was achieved through our collaborators in China (Chinese Institute of Atomic Energy, CIAE). This has enabled us to increase the number of crystals in the calorimeter by more than a factor of two over that envisioned in the original proposal and funded by the NSF MRI award. The increased size of the crystal detectors significantly enhanced the high resolution part of the calorimeter and played a critical role for the π^0 decay width extraction in the current experiment. Each crystal arrived at JLab from the manufacturer was first tested for mechanical properties (visual inspection and dimensions at four points). A typical distribution of measured sizes at the front of the crystals from one shipment is shown in Figure 7. For those crystals that satisfied the mechanical specifications, the optical transmission *versus* wavelength was measured using the JLab Detector Group's spectrophotometer. Typical transmission spectra are shown in Figure 8 and Figure 9.

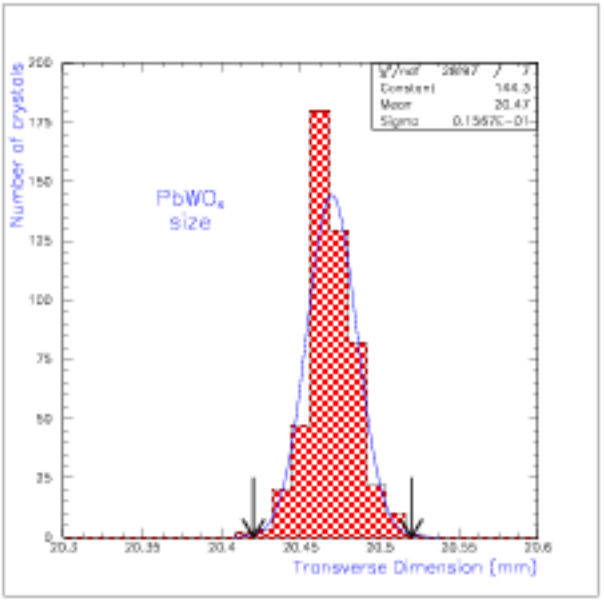

Figure 7: Distribution of front size of crystals from one shipment. Tolerance in size is shown by arrows.

Two important criteria have been set for the lead tungstate detector module development: to optimize the light collection from the back side of the crystal and to minimize the mechanical structure in the transverse dimensions. A complete module of the $PbWO_4$ crystal detector is shown in Figure 10. The scintillation light from the electromagnetic shower in the crystals was detected with Hamamatsu R4125HA photomultiplier tubes (PMT) coupled to the back with optical grease. Each crystal was first wrapped in $\sim$63μm VM-2000 reflector (from 3M), then with a 38.1 μm black Tedlar for optical isolation between the blocks. The

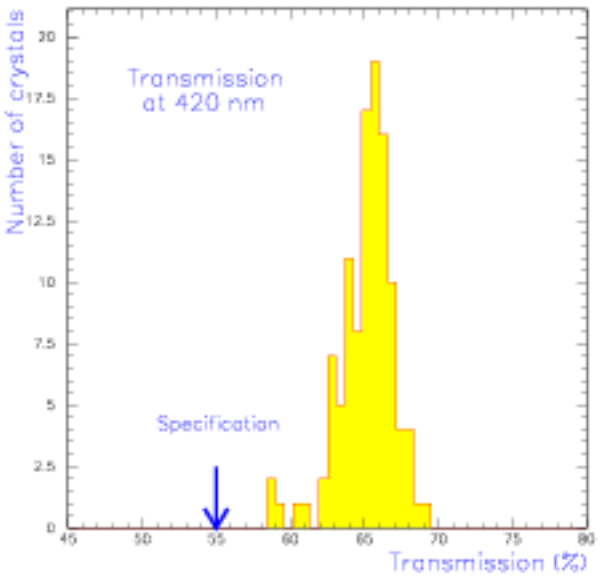

Figure 8: Optical transmission of crystals at 420 nm.

PMT housings were attached to the crystals with two specially designed brass flanges on the front and back of the crystals, stretched with two 25 μm brass strips.

One of the challenging problems of the hybrid type calorimeters is the potential deterioration of the energy and position resolutions at the boundary region between the two types of radiators (for HYCAL, $PbWO_4$ crystals and lead-glass detectors). The difference in electromagnetic shower development both in longitudinal and lateral directions in $PbWO_4$ and lead glass also requires optimization of the position of the crystal radiators along the lead glass blocks. The first experimental results for the calorimeter characteristics *versus* the crystal z-position for 10-70 GeV electrons have been presented in [33]. Since the longitudinal development of the shower is energy dependent, the optimization of the z-position is energy dependent as well. We have performed extensive Monte Carlo simulations to define the optimum z-position of the $PbWO_4$ radiators along the lead glass blocks for the HYCAL calorimeter. These simulations, which are cross-checked with the experimental data from Ref.[33], showed that for the few GeV energy region the optimum for the z-position is within the 7-10 cm interval. In order to investigate the performance of the calorimeter at the transition region between the $PbWO_4$ crystals and lead glass detectors, and, also to check the calorimeter's engineering concepts in real conditions, a prototype hybrid calorimeter (HYCAL-0) was constructed and tested in 2002 using the intense tagged photon beam. It consisted of 96 lead glass and 77 lead tungstate shower detectors and was assembled in a light-tight iron frame maintained at a stable temperature of $T = 11°C$. After the two stages of prototyping and successive beam tests, the *PrimEx* collaboration constructed and assembled 1152 $PbWO_4$ crystal shower detectors and 576 lead glass Cherenkov counters as

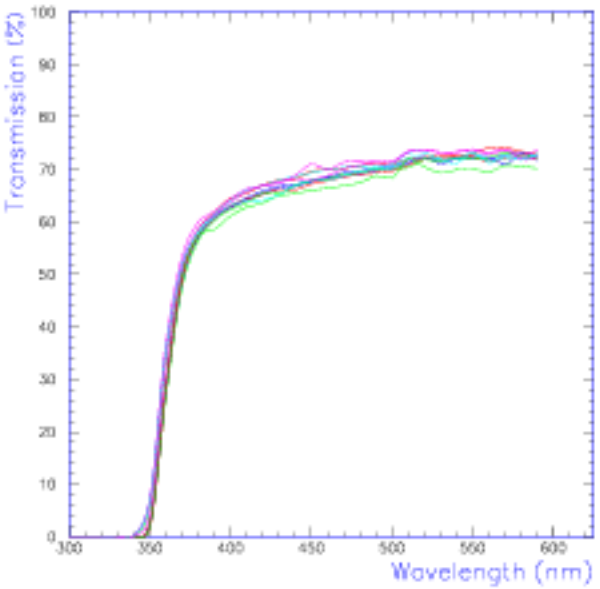

Figure 9: Typical optical transmission of crystals *versus* wavelength.

described above (116 $\times$ 116 cm^2 area). All individual detector modules have been stacked in a specially designed light-tight iron frame, as shown in Figure 11. The light yield of the crystal is highly temperature dependent ($\sim$ 2%/°C). In order to keep the detector array at a stable temperature, the detector assembly was surrounded by thick copper plates with circulating coolants. Temperature stability at the level of $\Delta T = \pm 0.1$°C was achieved during the entire period of data collection. To optimize the shower leakage in the transition region the lead tungstate detector assembly, which is in the central part of the calorimeter, is shifted downstream of the lead glass modules by 10 cm. Four crystal detectors are removed from the central part of the calorimeter (4.1 $\times$ 4.1 cm^2 hole in size) for the passage of the incident photon beam through the calorimeter.

The calorimeter is furnished with rear end readout electronics, with signal cables (two from each channel, for anode and dynode signals), high voltage cables and fiber optics cables to the front part of the calorimeter for gain monitoring system. After 300 ns delay, the anode signals were digitized by means of a 14-bit charge-sensitive ADC (LeCroy 1881M, integration width=240 ns). The positive dynode signals ware summed group by group to form a total sum from the entire calorimeter for the trigger organization as described in the next sections.

4.3 The Calorimeter Frame and Transporter

The individual modules of the HYCAL are assembled in a rectangular box inside of the calorimeter frame. The entire assembly weighs over five tons, and is movable in both horizontal and vertical directions in order to place each module in the beam for energy

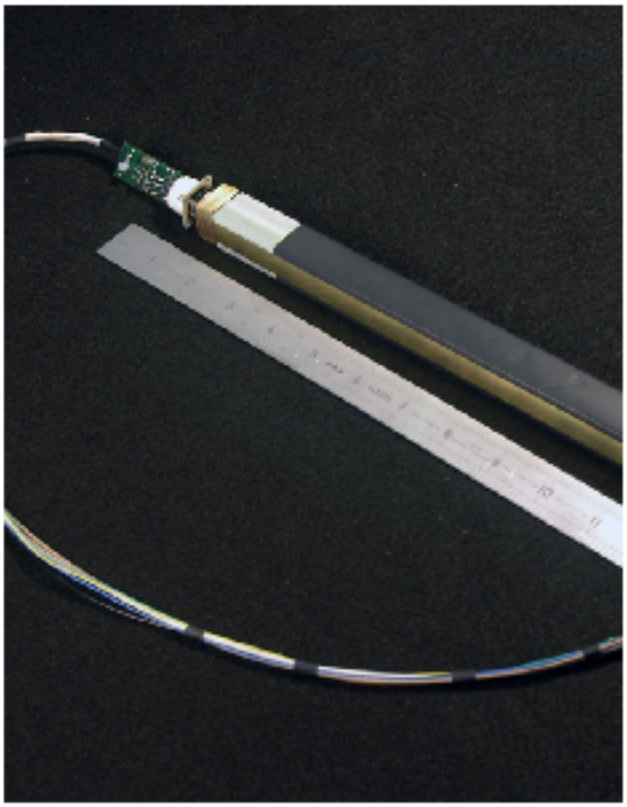

Figure 10: A single $PbWO_4$ crystal shower detector module.

calibration. The transporter, shown in figure 4.2.2, has been designed and constructed to provide movement of the entire assembly of the support frame with detectors and thermo-stabilization system, the delay cables, the gain monitoring system mounted on the bottom of the HYCAL frame and the veto counters on the front of the HYCAL.

The calorimeter is remotely movable so that during the calibration and checkout of each module it can be positioned in the beam of tagged photons with an accuracy of $\pm 2mm$. A schematic drawing of this system is shown in figure 13. After the calibration and channel by channel checkout procedure, the calorimeter was moved to a specially designed support stand for the experiment. A drawing of the calorimeter in the data taking position is shown in figure 14. In this configuration, the accuracy of positioning the detector transverse to the beam is $\pm 0.7mm$. In addition, this system also provides the capability to move the detector along the beam line for the different Z-position from the physical target.

When the calorimeter is not being used in the beam, the transporter system provides positioning of the entire calorimeter a few meters above the beam center, on Level 2 of the Hall B beam line. In addition to storage, this configuration allows the HYCAL to be available for re-assembly, maintenance, and testing with cosmic rays.

4.4 Performance of the Calorimeter

As mentioned above, the calibration of the HYCAL was performed with a low intensity tagged photon beam of selected energies ($E_\gamma = 0.5 - 5.5$ GeV), irradiating the centers of

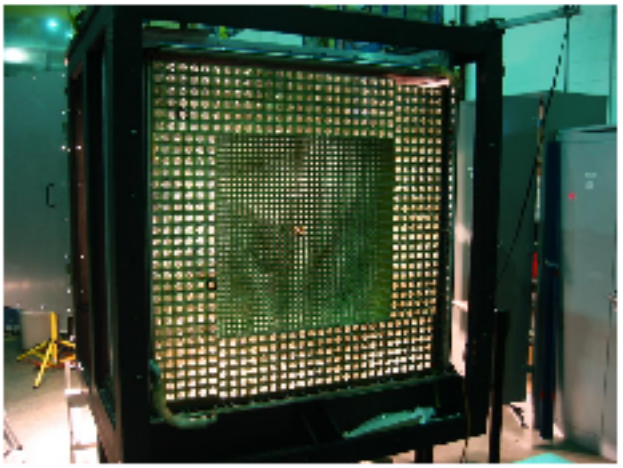

Figure 11: Front view of the HYCAL Calorimeter with all modules in place and before installation of fiber optics cables on front of each channel for the gain monitoring system.

each detector module while the calorimeter was in the transporter configuration. Then, a tagged photon beam was scanned across the boundary with 2 mm step size to get data for the position and energy resolutions for the both type of detectors, as well as for the transition region between them.

The reconstructed energy distribution for the 4.3 GeV electrons is shown in figure 15 for three different calibrated ADC sums: the central module; the inner section comprising 3×3 crystals and the array of 6×6 crystals. The energy resolution is obtained using a Gaussian fit of the 6×6 distribution. As can be seen from the figure, an excellent energy resolution of $\sigma_E/E = 1.3\%$ has been achieved for 4.3 GeV. The measured energy resolution *versus* initial photon energy is shown in figure 16. The resolution of the lead glass part of detector is shown in figure 17 for lead tungstate.

Using the data from the transition region, the energy resolution of the shower cluster was extracted as a function of position. Dependence of the energy resolution *versus* photon impact position is shown in Figure 18. Degradation in resolution as the photon beam passes from the last lead tungstate module to the lead glass region is evident and well described by the Monte Carlo simulation. Figure 18 (bottom) shows the relative reconstructed total energy for the same transition region. The $\sim 3\%$ dip at the interface predominantly arises from shower leakage from the uncovered backs and sides of the lead glass blocks.

The impact coordinates of the electromagnetic particles incident on the segmented hodoscopic calorimeters are determined from the energy deposition of the electromagnetic shower in several neighboring counters. In the case of the $PbWO_4$ crystals, the transverse size of the shower is about two times smaller than that in lead glass. As a result, the position resolution in the $PbWO_4$ detector with an optimal cell size should be about twice smaller than that of lead glass detectors. To maximize the position resolution, we have optimized the crystals' transverse dimensions, and have selected them to be 2.05×2.05 cm^2. This size is comparable to the Molière radius (2.2 cm) of the crystal material.

The distribution of the reconstructed coordinates for 4.3 GeV electrons hitting a crystal cell boundary is shown in Figure 19. The linear dependence of the reconstructed coordinates

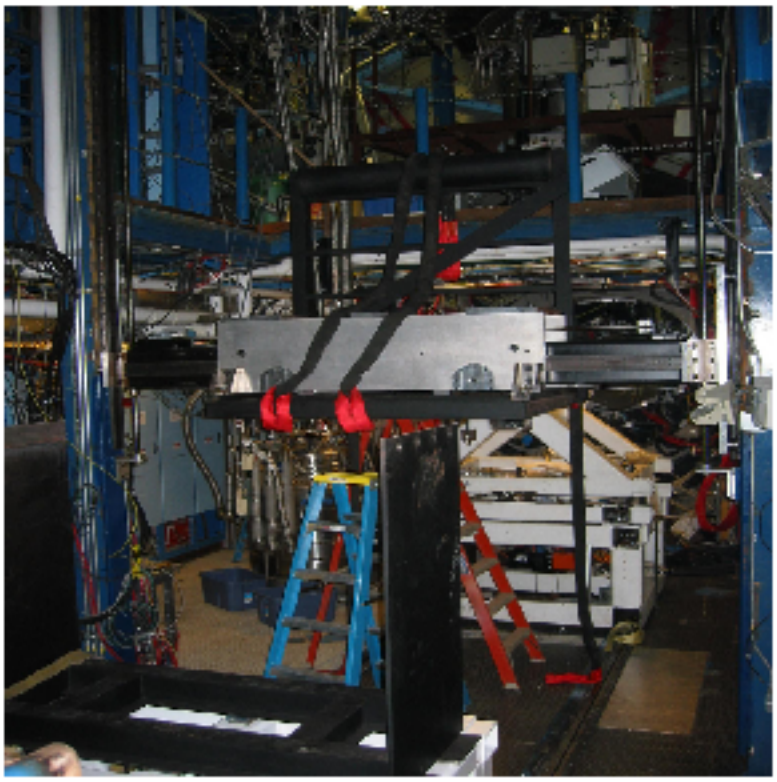

Figure 12: The HYCAL transporter in Hall B.

obtained from a logarithmically weighted average of the cell signals *versus* the impact positions is shown in Figure 20. As is well known, there is a rather strong correlation between the position resolution (σ_x) and the point at which the incoming electrons or photons hit the detector face. The bottom plot of the figure shows this dependence for the $PbWO_4$ crystals. The σ_x is smaller (1.28 mm) near the edge of the cell and increases to 2.1 mm at the cell center.

Similar to the energy reconstruction, one can expect degradation in the position resolution in the transition region as the photon beam passes from the last lead tungstate crystal module to the lead glass region. This dependence is shown in Figure 21. Though the simple center-of-gravity reconstruction exhibits typical oscillation of reconstructed *versus* impact position with a relatively larger amplitude, the corrected logarithmic method shows a good linear transition from lead tungstate to lead glass regions.

Good position and energy resolutions achieved for the HYCAL calorimeter provided critical improvements in both two gamma invariant mass and production angle reconstructions. As an example, in Figure 22 is shown the two gamma invariant mass distribution extracted from the experimental data set for one angular bin only. An excellent resolution of $\sigma_{\gamma\gamma}$ =2.3 MeV provided precision extraction of events over the experimental background.

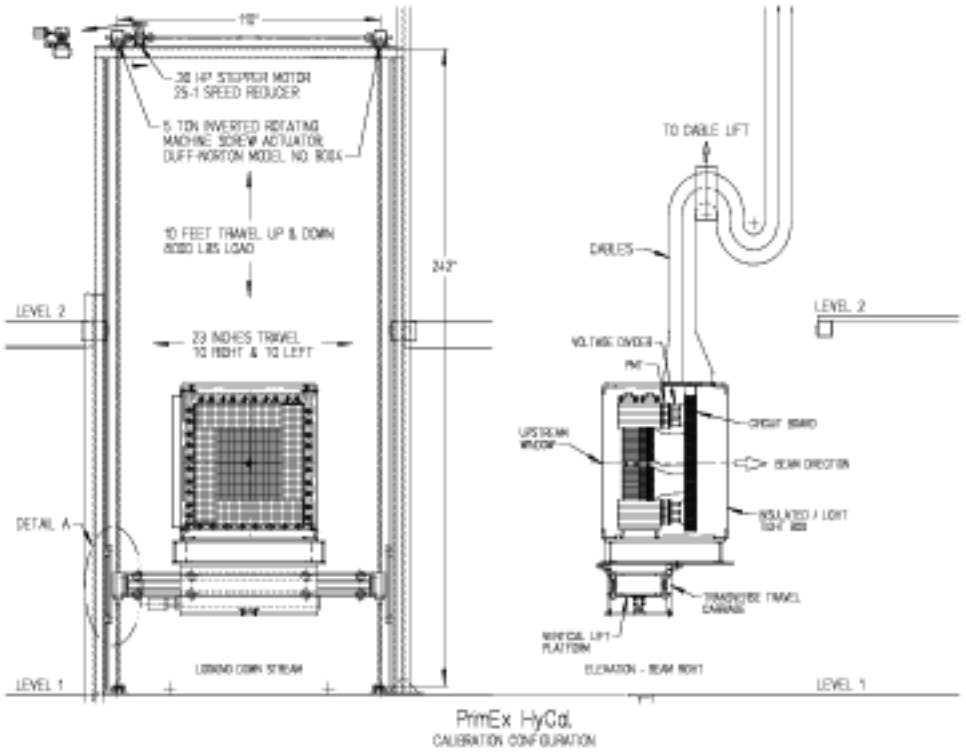

Figure 13: The HYCAL mounted on its transporter.

4.5 HYCAL Gain Monitoring System

To control the stability of gains for each channel of the calorimeter during the long data taking periods, a gain monitoring system was developed and constructed This system is based on feeding light pulses from a central LED based light source distributed by fiber optics cables to the front part of each module. The main components of the Light Monitoring System (LMS) are: (1)a light source, (2) a mixing box, (3) a light distribution system, (4)filter wheel, (5)reference detectors and (5) a dedicated data acquisition system. The optical components and the reference detectors, as shown in Figure 23, are mounted in a thermally insulated box whose temperature is controlled at a level of 0.1°C.

Long term stability tests of the prototype LMS system, as well as several beam tests, have been performed to finalize the design and characteristics of the system. For this tests, the light intensity was monitored with a PIN photodiode and three reference PMTs. In figure 24, top picture, the distribution of the ratio, PMT_1/PMT_3, for the period of time of 540 hours is shown. The same ratio plotted versus time, is presented in the bottom picture.

During the data taking period it was observed that the LMS reference detectors are somewhat sensitive to the change of magnetic field from the pair spectrometer dipole. This change of signals was observed on the level of 1.5% on the reference PMT signals [31]. We plan to fix this problem by adding more magnetic insulation and/or try to replace the PMTs on the reference detectors with less sensitive photodetectors.

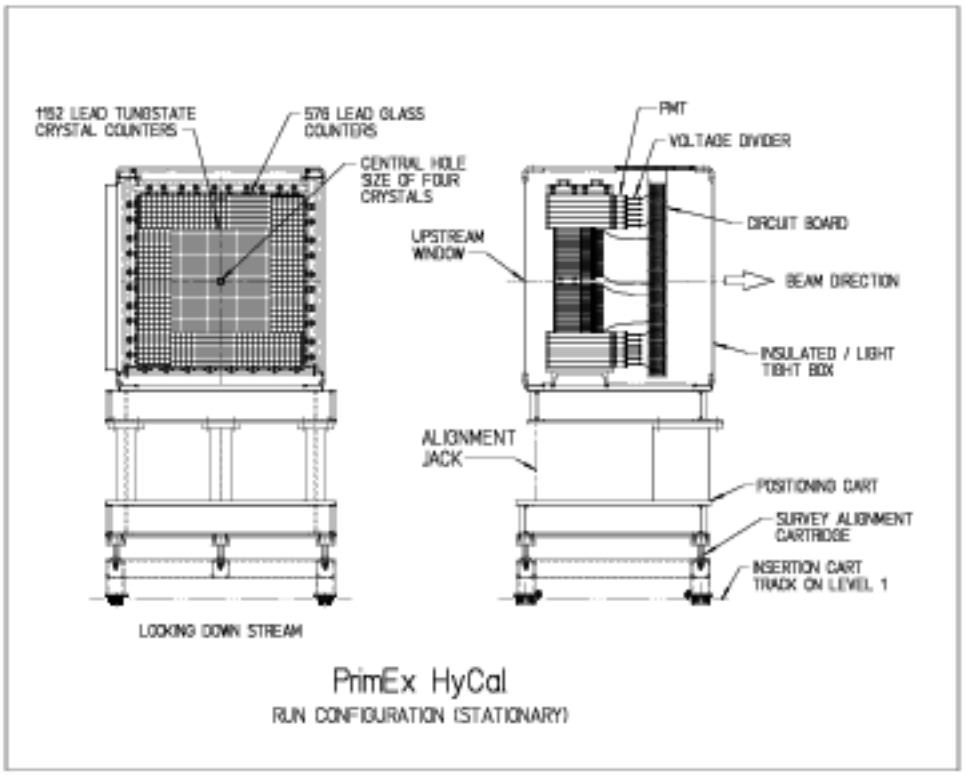

Figure 14: The HYCAL detector on its support stand in the run configuration.

4.6 Luminosity monitoring

The primary advantages of the *PrimEx* experiment over the previous Primakoff experiments arise from the use of the Jefferson Lab Hall-B photon tagging facility to carefully control systematic errors and reduce backgrounds. First, the tagging technique allows for a significantly more accurate knowledge of the photon flux. Second, due to the energy dependence of the Primakoff cross section, it is critical to have a good knowledge of the absolute photon beam energy.

In order to determine the energy of the decaying π^0, each event is recorded in coincidence with a signal from the tagger. The experimental cross section for neutral pion photo-production is given by:

$$\frac{d\sigma}{d\Omega} = \frac{dY_{\pi^0}^{tagged}}{N_{\gamma}^{tagged} \cdot \epsilon \cdot t \cdot d\Omega} \tag{8}$$

where $d\Omega$ is the element of solid angle of the pion detector, $dY_{\pi^0}^{tagged}$ is the yield of tagged π^o's within solid angle $d\Omega$, t is the target thickness, ϵ is a factor accounting for geometrical acceptance and energy dependent detection efficiency and N_{γ}^{tagged} is the number of *tagged* photons on the target.

The number of tagged photons per post bremsstrahlung electron can be measured in a calibration run by removing the physics target and placing a lead-glass total absorption counter (TAC) directly in the photon beam. Assuming that the total absorption counter is 100% efficient in detecting photons in the energy range relevant for the experiment, the

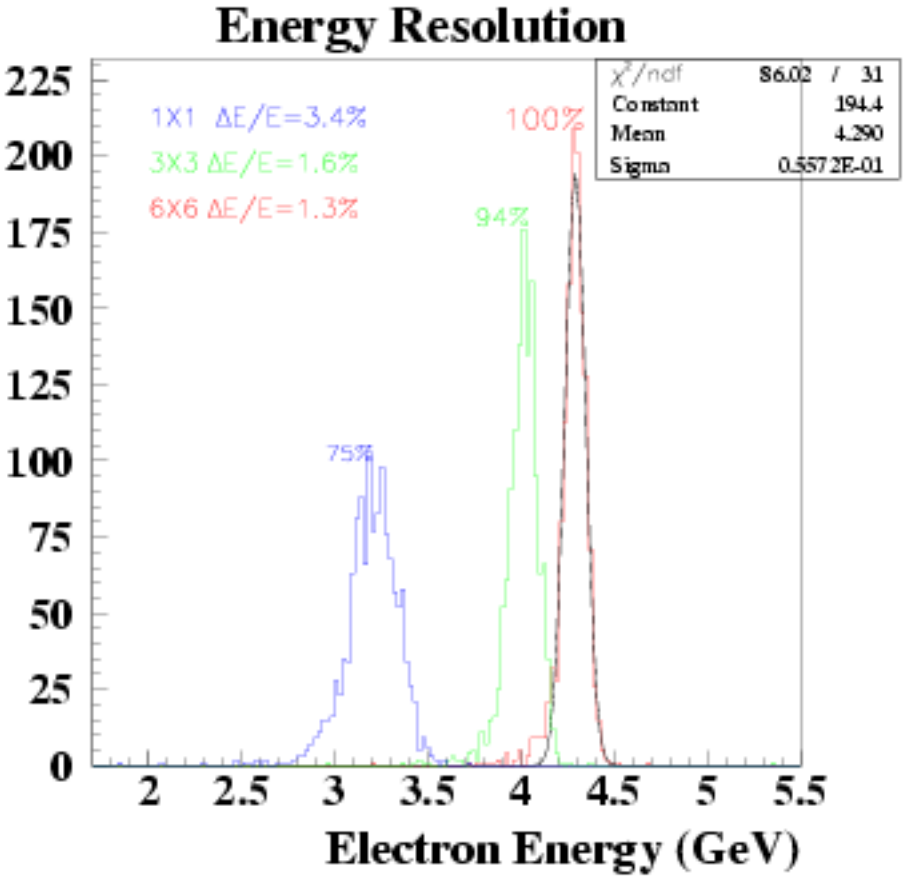

Figure 15: Energy response of a $PbWO_4$ crystal array to 4.3 GeV electrons. Left peak: single crystal; center peak: 3×3 array; right peak: 6×6 array.

ratio of Tagger·TAC coincidences to the number of tagger hits, the so called absolute tagging ratio, is then recorded:

$$R_{absolute} = \frac{N_{\gamma e}^{TAC}}{N_e}|_{calibration} \tag{9}$$

where $N_{\gamma e}^{TAC}$ is the number of photons registered by the TAC in coincidence with a tagging signal and N_e is the number of electrons registered in tagging counters.

Knowing this ratio, one can determine the tagged photon flux in the data taking run by counting the number of post bremsstrahlung electrons in the tagging counters:

$$N_\gamma^{tagged}|_{experiment} = N_e|_{experiment} \times R_{absolute} \tag{10}$$

The use of the total absorption counter to calibrate the number of tagged photons per electron in the tagger provides an absolute normalization of the photon flux incident on the π^0 production target. However, these measurements can be performed only at intervals between the data taking. Also in the calibration run, the rate of the total absorption counter

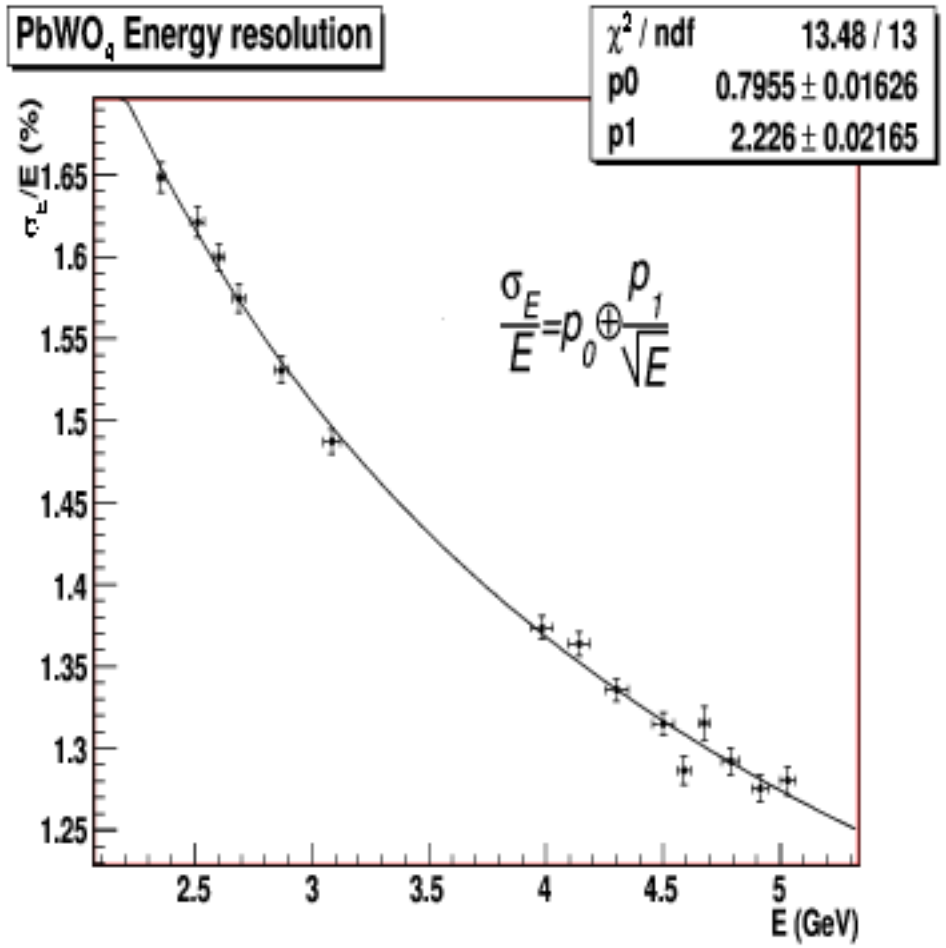

Figure 16: Measured energy resolution *versus* photon beam energy for the $PbWO_4$ part of the calorimeter.

is limited, and therefore, the tagging ratio can only be measured at a rate which is reduced by a factor of about one thousand as compared to the data taking run. A pair production luminosity monitor was constructed which is able to measure the relative tagged photon flux over a range of all relevant intensities, and operate continuously throughout the data taking runs. The PS uses the physics target as a converter to measure the ratio of the number of $\gamma + A \rightarrow A + e^+ + e^-$ reactions in coincidence with a tagging signal to the number of hits in the tagging counters (see Equation 11),

$$R_{relative} = \frac{N^{PS}_{e^+e^-e}}{N_e}. \tag{11}$$

While this is a relative number, its absolute normalization can be fixed with the TAC. The advantages of the pair spectrometer are that it can operate over the entire range of intensities (of both the flux calibration and data taking runs) and has a smooth, relatively flat acceptance in E_γ covering the entire tagging range.

The main contribution to the error bar in the *PrimEx* measurement comes from the knowledge of the photon flux. To achieve the desired precision in the measurement of the

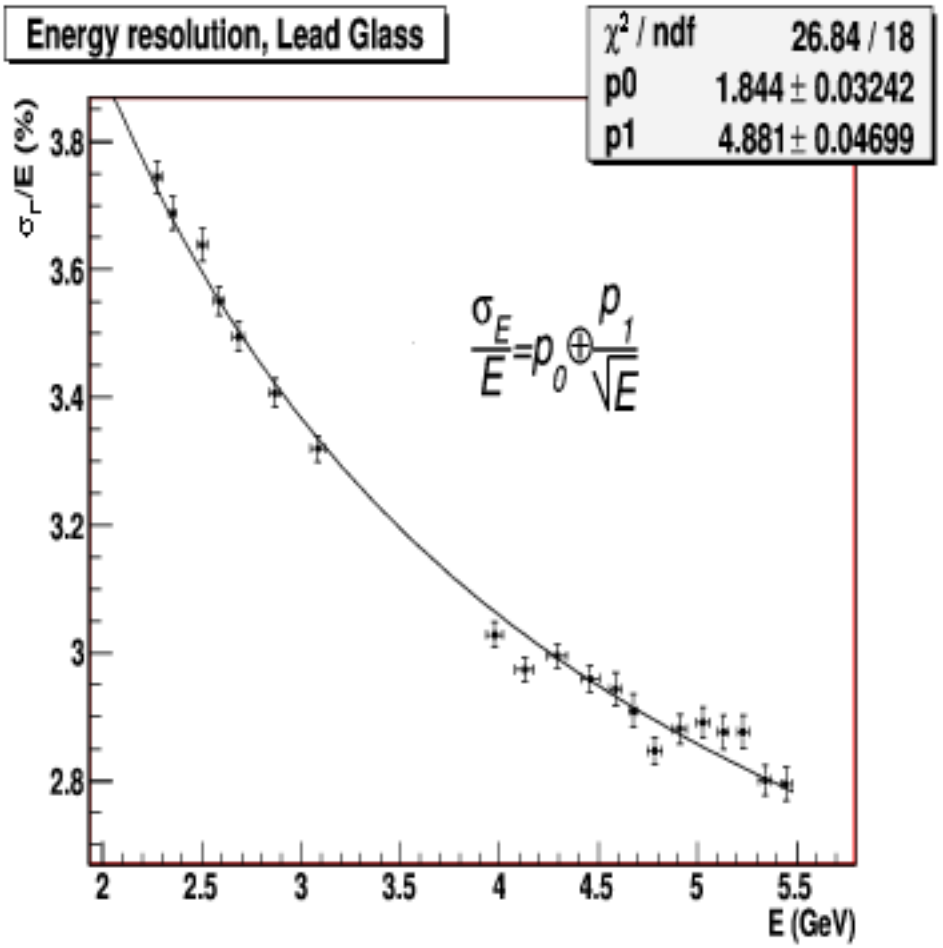

Figure 17: Measured energy resolution *versus* photon beam energy for the $PbWO_4$ part of the calorimeter.

π^0 decay width, it is necessary to know the photon flux to 1% or better. It should be noted that such a high precision measurement of the photon flux had not been previously attempted at Jefferson Lab Hall-B. As indicated by equation 10, the problem of cross section normalization is reduced to the determination of the number of electrons in tagging counters and measuring the absolute tagging ratio. The constant on line monitoring of the relative photon flux is also crucial for the precision tagged photon flux measurement.

4.6.1 Absolute tagging ratios

During *PrimEx* data taking in the Fall of 2004, specialized calibration runs were periodically performed to determine the absolute normalization of the photon flux. For a calibration run, the experimental target is retracted and a Total Absorption Counter (TAC) is placed in the path of the photon beam. To avoid the radiation damage to the TAC, the electron beam intensity is lowered to $\sim 70 - 80pA$. The low intensity of calibration runs enables the use of the Tagger Master OR (MOR) signal as the data acquisition trigger. The MOR signal is formed by OR-ing the timing information from all or any of the 61 T-counters. Using

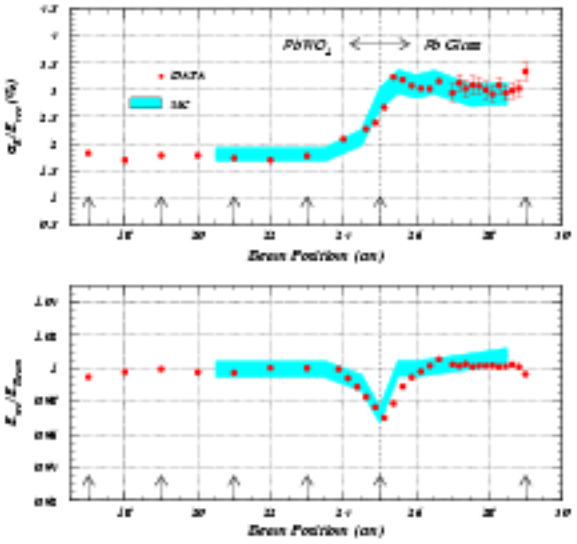

Figure 18: Beam test results for the transition region between $PbWO_4$ and lead glass modules. Top: energy resolution. Bottom: relative reconstructed energy *versus* position. The gray bands indicate Monte Carlo simulations.

the MOR trigger enables one to directly count the number of electrons that hit the tagging counters.

Absolute tagging ratios are defined for each of the T-counters as:

$$R^i_{absolute} = \frac{N^{TAC}_{\gamma e^1}}{N^i_e} \tag{12}$$

where N^i_e is the number of electrons registered in the T-counter i and $N^{TAC}_{\gamma e^1}$ is the number of photons registered by the TAC in coincidence with an electron in the T-counter i.

A number of possible systematic errors associated with the determination of the absolute tagging ratios were studied in our 2004 run. These included:

- Effects of incident electron beam intensity on absolute tagging ratios
- Effects of photon collimator size
- Effects of collimator position misalignment
- Effects of HYCAL scraping due to beam mis-steering
- Long and short term reproducibility of tagging ratios
- Effects of the pair spectrometer dipole field on the tagging ratios
- Absorption in the target

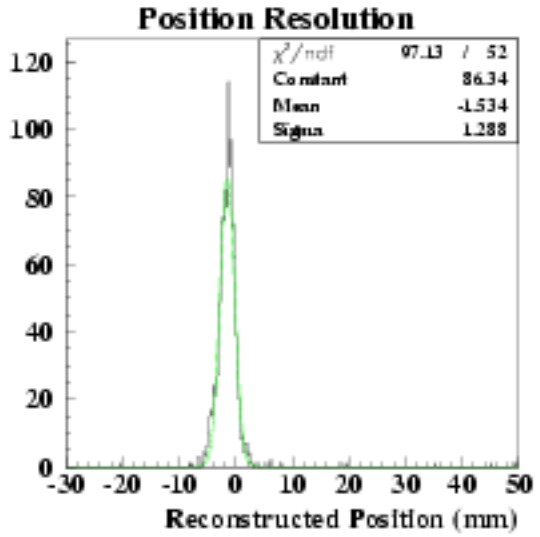

Figure 19: Distribution of reconstructed positions at the boundary between two lead tungstate crystal detectors.

The details of these studies are given in an appendix, with the general conclusion that the overall uncertainty in the flux determination, both systematic and statistical, was found to be 1%.

4.6.2 Relative tagging ratios measured with pair production

The Pair Spectrometer is an essential part of the em PrimEx experimental apparatus designed for relative in-situ monitoring of the photon flux. It uses the experimental target to convert a fraction of the photons into e^+e^- pairs. These are deflected in the field of a dipole magnet downstream of the target and are registered in plastic scintillator detectors on both sides of the beam-line. The relative tagging ratios per T-counter are defined as:

$$R^i_{relative} = \frac{N^{PS}_{e^+e^-e^i}}{N^i_e} \tag{13}$$

where N_{e_i} is the number of electrons registered in T-counter i and $N^{PS}_{e^+e^-e^i}$ is the number of e^+e^- pairs registered by PS in coincidence with an electron in T-counter i.

During our production data taking in the Fall of 2004, we utilized a random, (*i.e.* not related to the the beam), clock trigger set up to measure $R^i_{relative}$. The use of the random trigger enables a direct counting of number of electrons in the tagging counters and it gives the advantage of being insensitive to beam intensity variations.

4.7 Photon beam position monitor

A photon beam position detector was constructed by the collaboration that provided continuous real time photon beam position and profile information during the first experiment,

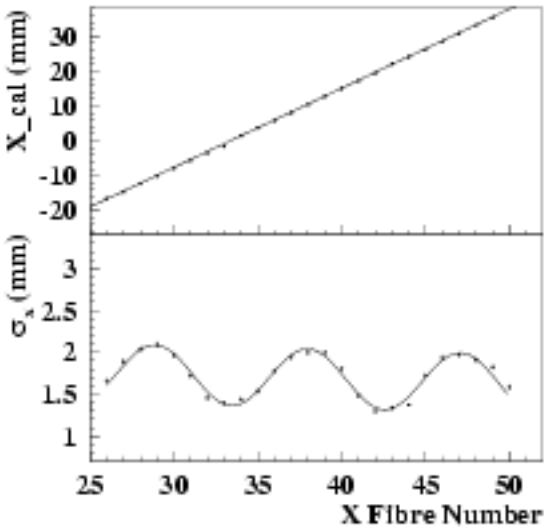

Figure 20: Reconstructed *versus* actual position (top) and position resolution (bottom) across the face of $PbWO_4$ crystal array.

as well as information in the data stream for off-line data analysis. This detector consists of two identical modules crossed at right angles to each other (as shown in figure 25) to give the beam profile along both x and y directions. Each module is a linear hodoscope of multi-channel Bicron scintillating fibers (the x module has 61 channels and the y module has 62) forming a plane perpendicular to the photon beam. This detector is mounted on a remote controlled table with x and y motion placed just behind the HYCAL in the nominal beam path. Each scintillation fiber has dimension of $2 \times 2 \times 13$ mm^3. The scintillating light from the fibers is transmitted through the light guide and is detected by four 16-channel R5600-M16 Hamamatsu PMTs. A compact electronics module provides 64 channels of amplifier and discriminators for anode signals, then converts them to ECL readout through a time-over-threshold circuit. The ECL signals are sent over to SIS3801-256-flat scalars and read into the EPICS system. During the run, the x and y beam profiles were displayed through a GUI for on-line beam control (shown in figure 26) and read into the DAQ for off-line analysis. This device performed beautifully during the experiment and provided an excellent beam diagnosis tool.

4.8 Data acquisition and trigger

The *PrimEx* data acquisition system must read out over 2200 channels of ADC and TDC information coming from five different detector systems. These include the HYCAL calorimeter, the HYCAL veto, the pair spectrometer, the total absorption counter, and the Hall B photon tagger. The digitization electronics will span at least three Fastbus crates which must be coordinated for proper event reconstruction.

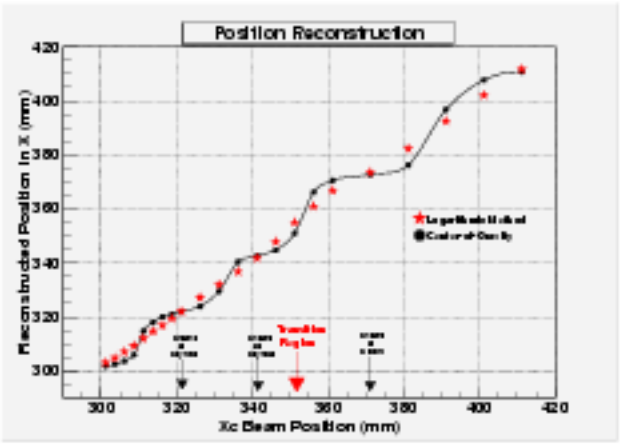

Figure 21: Reconstructed *versus* impact coordinate at the transition region of the HYCAL calorimeter.

The *PrimEx* data acquisition system is a CODA based Fastbus system utilizing the JLab designed Trigger Supervisor module. In addition to the three Fastbus crates, this system includes one CAMAC crate, one VME crate, and one hybrid VME/VXI crate. Electronics occupying six NIM crates are also needed for the first stages of the trigger. A big advantage of the CODA/Trigger Supervisor system is the ability to run in fully buffered mode. In this mode, events are buffered in the digitization modules themselves allowing the modules to be live while being readout. This significantly decreases the dead time of the experiment. All of the electronics needed for the *PrimEx* DAQ and trigger electronics has been procured and is on site at JLab.

4.8.1 Trigger

The *PrimEx* trigger is formed from the last stage dynode signals from HYCAL. The anode signals are sent directly to the Fastbus ADC modules via long RG58 cables. The trigger initially constructed for the 2004 *PrimEx* run would have looked for multiple clusters in HYCAL separated by at least 15 cm. This was done by fanning in strips of like detectors ($PbWO_4$ and Pb-glass are done separately) which span the calorimeter in both the horizontal and vertical directions. In the $PbWO_4$ region of the calorimeter the strips are either 7 or 8 detector units wide, and in the Pb-glass the strips are either 3 or 4 detector units wide. There are 7 such strips in the horizontal direction, and 7 strips in the vertical direction. Using strips in this fashion ensures at least 50% of the energy deposited in one cluster will be seen by a discriminator. Each strip was discriminated at a level of one half of the minimum energy π^o decay photon we wish to detect. This level was set to 0.5 GeV since we wish to accept all events with photon energies 1 GeV or higher. The 7 strips of each direction are taken to form a 14-bit word which was then used to access an address of a Memory Mapping Unit (CAEN C542). Patterns in which either (i) two non-adjacent strips fire in one direction or (ii) two adjacent strips fire in both directions would have created a trigger.

However, in the commissioning period preceding the 2004 run, it was discovered that reasonable trigger rates are obtained using a trigger based on the total energy sum in HYCAL.

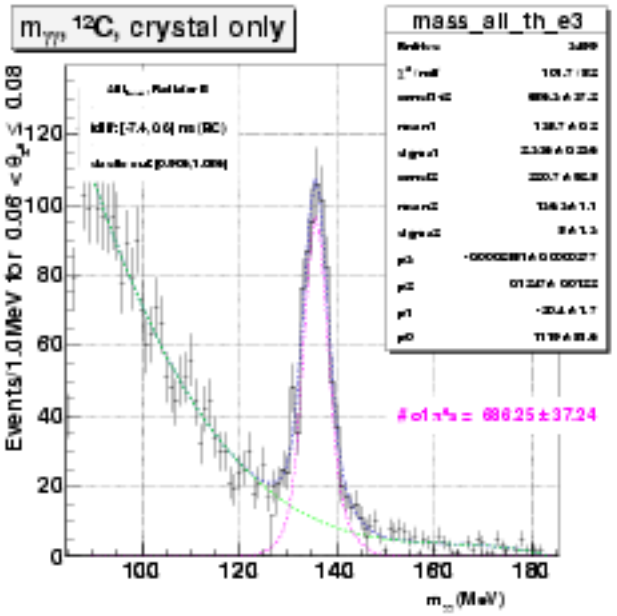

Figure 22: Distribution of two gamma invariant mass from the experimental data set for one production angle bin.

For this reason, it was decided to take data with the more conservative and conceptually simpler total energy sum trigger. By using the energy sums already established for the trigger strips, only one additional level of signal fan-in was required to form the total energy sum. The energy sum trigger threshold was set at approximately 2 GeV for the 2004 run, and the trigger rate for the ^{12}C running was a modest, by Hall B standards, $1.2kHz$. We propose to use the same total energy sum trigger for the next *PrimEx* run.

The UVA120 and 125 linear fan-in and discriminator modules were chosen for the *PrimEx* trigger electronics because of the large number of channels (36 for the UVA120 module) and the economic advantage over commercial modules. The specific needs of the *PrimEx* trigger required some special modifications to both the UVA120 and its sister module, the UVA125. One significant modification in the UVA120 design was to make both outputs inverting. This allows the module itself to be used as both a splitter and inverter for the dynode signals, eliminating the need for additional hardware. The UVA125 is used for the last stage of fan-in and discrimination, and has four separate sections. Each section has a 9-input linear fan-in and two built-in discriminators. The timing of the discriminators is determined by the discriminator with the lower threshold, making the timing properties better than single leading edge discriminators. The UVA125 modules can have the discriminator thresholds set via externally supplied voltages. These voltages will be supplied via a CAMAC DAC module (digital-to-analog converter) so that the thresholds may be adjusted remotely without making an access to the experimental hall.

The only user controlled part of the trigger is the DAC, which is housed in a CAMAC crate in Hall B. The DAC is used to set the threshold for the energy sum trigger. The CAMAC crate is controlled remotely over the internet, through a Kinetic Systems GPIB CAMAC controller and National Instruments GPIB E-Net device.

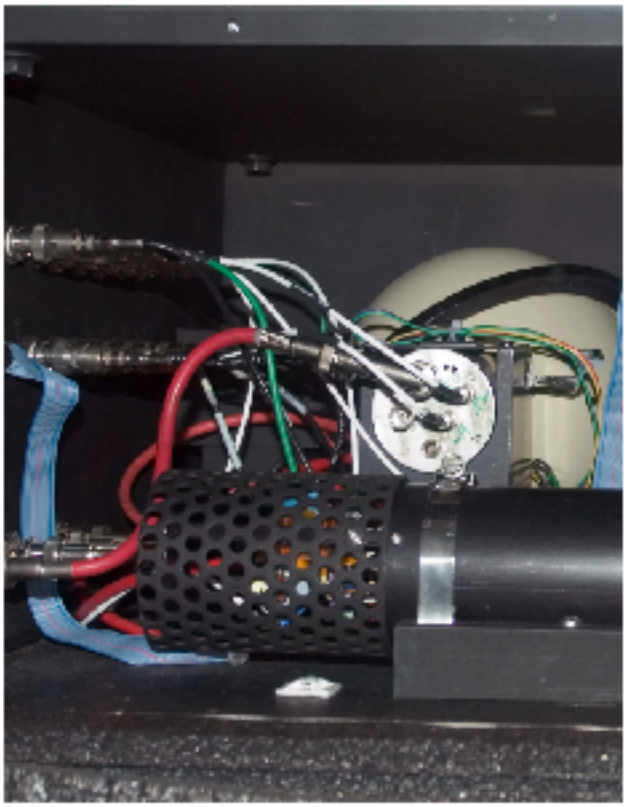

Figure 23: The light monitoring box mounted under neat of HYCAL.

5 Preliminary Results from the 2004 Run

5.1 π^o Photoproduction Cross Section Extraction

The *PrimEx* Collaboration has implemented three parallel data analysis procedures to extract the neutral pion lifetime. The primary considerations in event selection involve (1)HYCAL - Tagger timing information, (2) the invariant mass of the photons detected in the HYCAL, and (3), the elasticity of the candidate π^o events, where elasticity is defined as $\frac{E_{\gamma_1}+E_{\gamma_2}}{E_{tagger}}$.

The first analysis involves an event selection procedure which utilizes normalized probability distributions for each of the above mentioned quantities. In this analysis, the total probability of a valid event is given by the product of each of these probabilities as follows:

$$TotalProbability = Timing \times InvariantMass \times Elasticity \tag{14}$$

An example of such a likelihood spectrum is shown in figure 27. For pion candidate events which are in coincidence with multiple photons on the tagger, this enables the selection of the best photon. Extensive studies of the inefficiencies of this selection procedure have been performed and found to have negligible effect on the resulting yield.

With this event selection procedure, the correlation between elasticity and reconstructed invariant mass is examined, and a new quantity, termed the "hybrid mass" is defined for

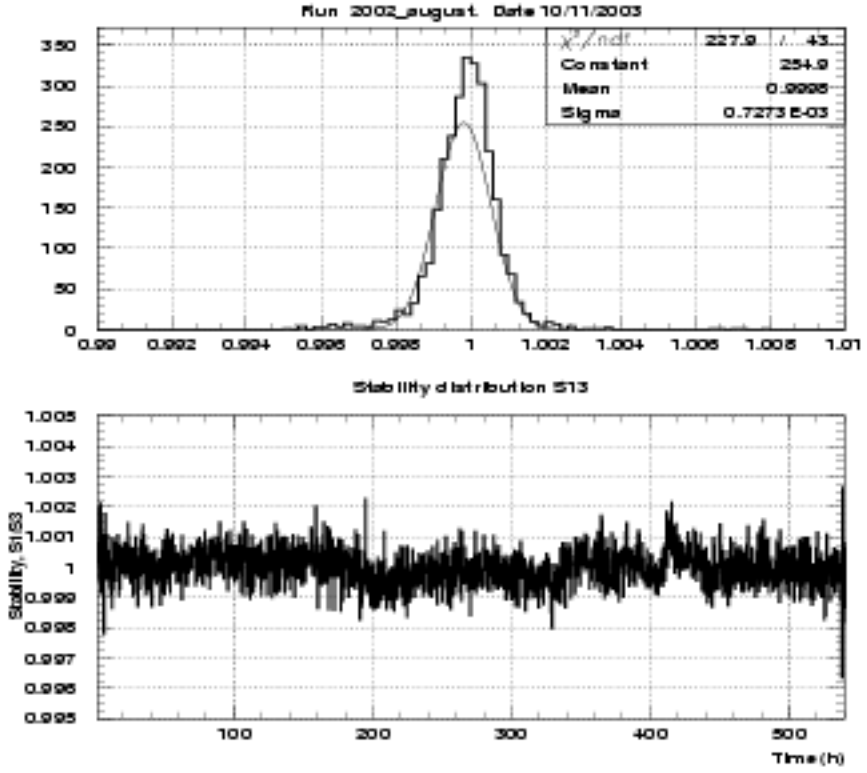

Figure 24: Stability of the light monitoring system.

each event. As indicated in figure 28, the hybrid mass is quantity which contains combined information on the elasticity and invariant mass.

A plot of the hybrid mass *versus* pion angle is shown in figure 29. A cut on the hybrid mass provides a clean separation of the pion events and the resulting angular distribution is shown in figure 30.

Dustin's analysis

Ilia's analysis.

5.2 Theoretical Calculations on Nuclear Form Factors and Backgrounds

5.3 Determination of $\Gamma_{\pi^o \to \gamma\gamma}$

5.4 Results of high precision calibration experiments

5.4.1 The absolute cross section for pair production

The *PrimEx* experimental setup provides a unique opportunity to verify the luminosity normalization procedure (including both photon flux and target thickness) by measuring

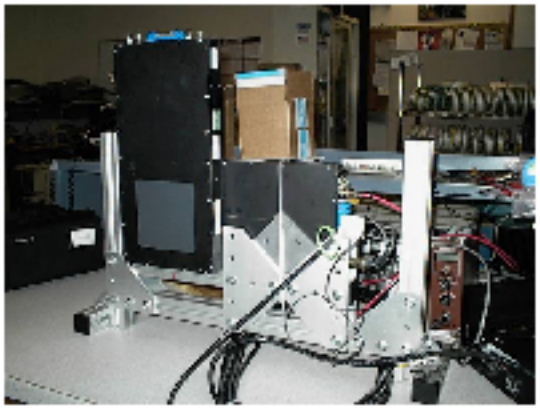

Figure 25: The *PrimEx* photon beam position detector.

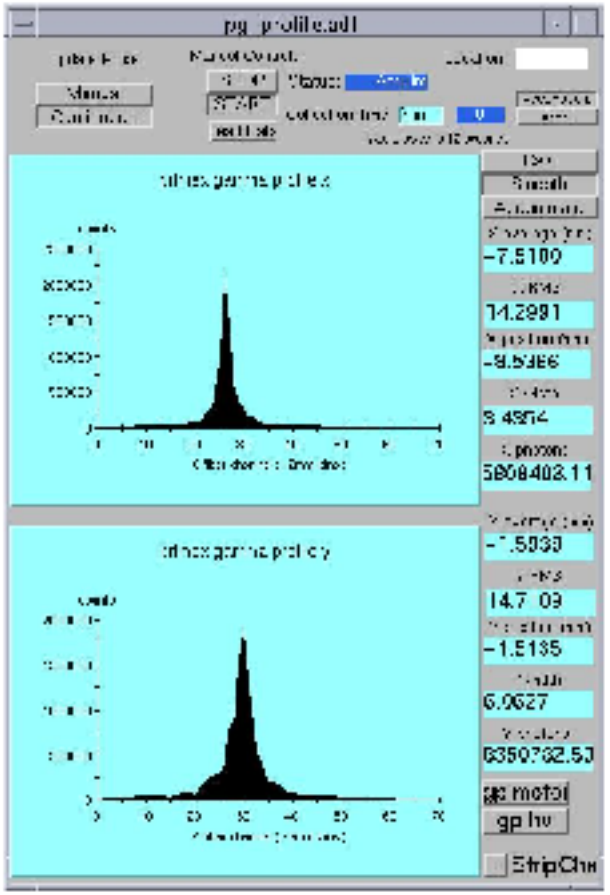

Figure 26: Photon beam position on-line display.

the absolute cross-section for a well known electromagnetic process, namely $(e^+\ e^-)$ pair-production, without any additional hardware development.

Cross-section calculations for the photo-production of e^+e^- – pairs on ^{12}C at photon energies of a few GeV and small momentum transfer $|\vec{Q}| \sim 10keV$ relevant for the PrimEx experiment were provided by A. Korchin[32]. A summary of different contributions included in the cross-section calculation are listed below in decreasing order of significance:

- Bethe-Heitler mechanism for pair production on the nucleus. To account for screening effects due to atomic electrons, two models for the atomic form factor (Thomas-Fermi-Moliere and Hartree-Fock) describing the charge distribution of electrons were considered. The Coulomb distortion effects have been included according to work of Bethe and Maximon (contribution to the e^+e^- cross-section of $\sim 80\%$).

- Pair production on atomic electrons taking into account the excitation of all atomic states and correlation effects due to the presence of other electrons and the nucleus (contribution of $\sim 20\%$).

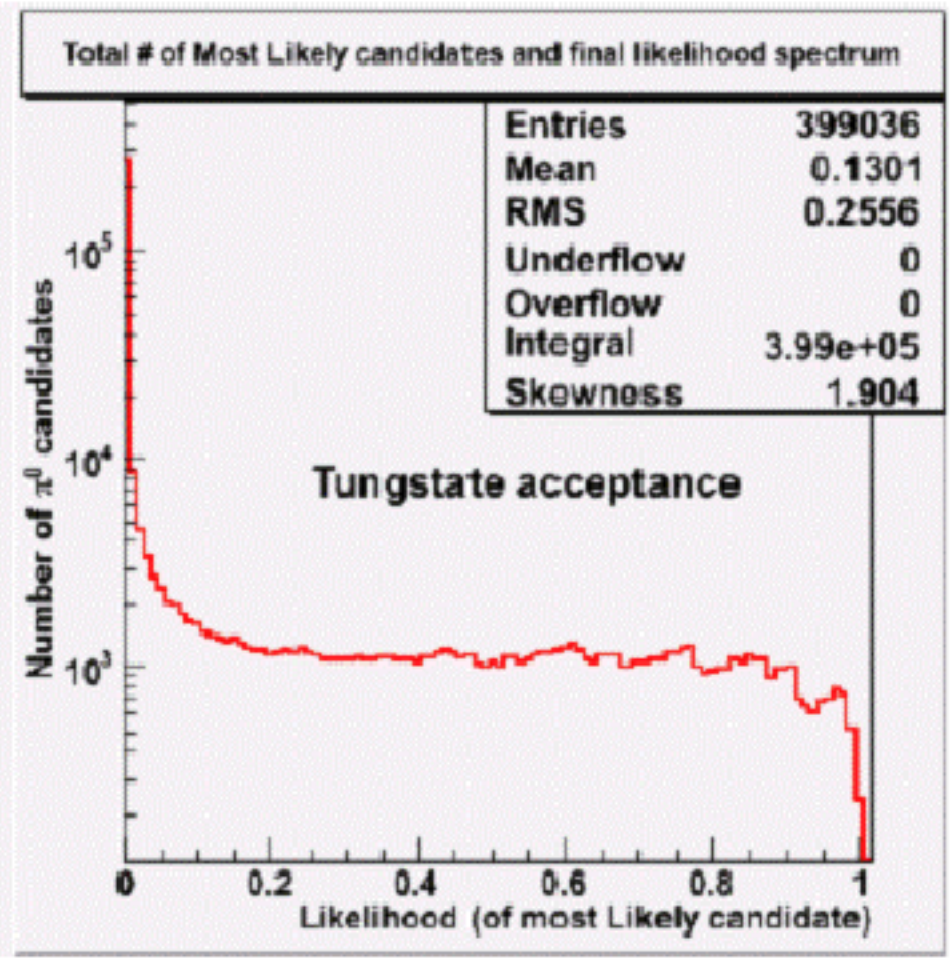
Total # of Most Likely candidates and final likelihood spectrum
Entries 399036
Mean 0.1301
RMS 0.2556
Underflow 0
Overflow 0
Integral 3.99e+05
Skewness 1.904
Tungstate acceptance
Number of π^0 candidates
10^5
10^4
10^3
0
0.2
0.4
0.6
0.8
1
Likelihood (of most Likely candidate)

Figure 27: .

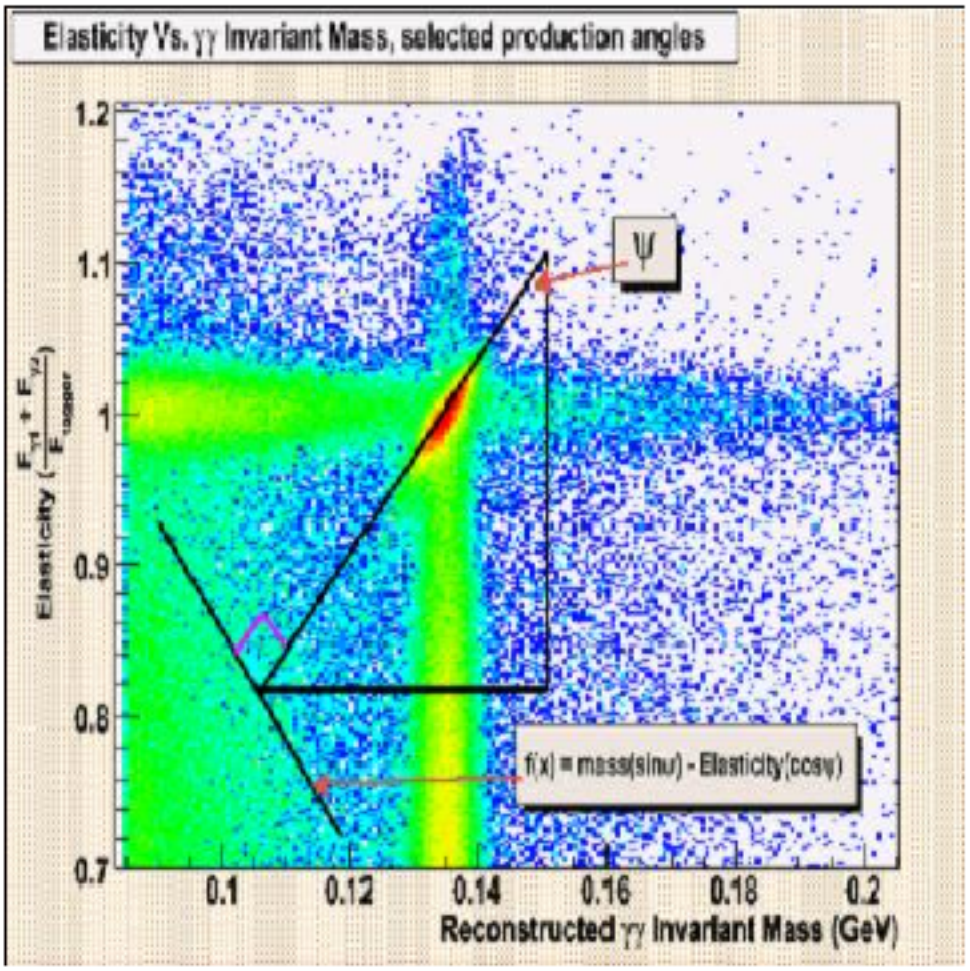
Elasticity Vs. γγ Invariant Mass, selected production angles
1.2
1.1
1
0.9
0.8
0.7
0.1
0.12
0.14
0.16
0.18
0.2
Reconstructed γγ Invariant Mass (GeV)
Ψ
f(x) = mass(sinω) - Elasticity'(cosω)

Figure 28:

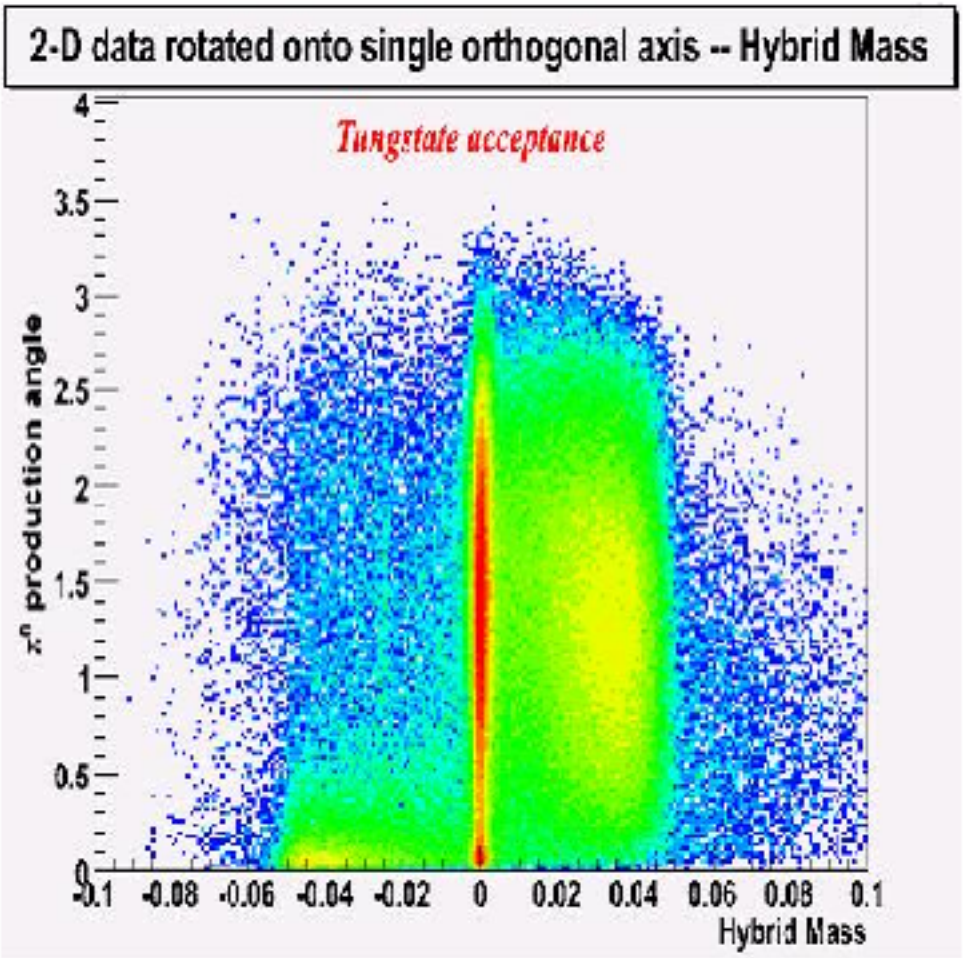
2-D data rotated onto single orthogonal axis -- Hybrid Mass
Tungstate acceptance
π^0 production angle
Hybrid Mass
4
3.5
3
2.5
2
1.5
1
0.5
0
-0.1
-0.08
-0.06
-0.04
-0.02
0
0.02
0.04
0.06
0.08
0.1

Figure 29:

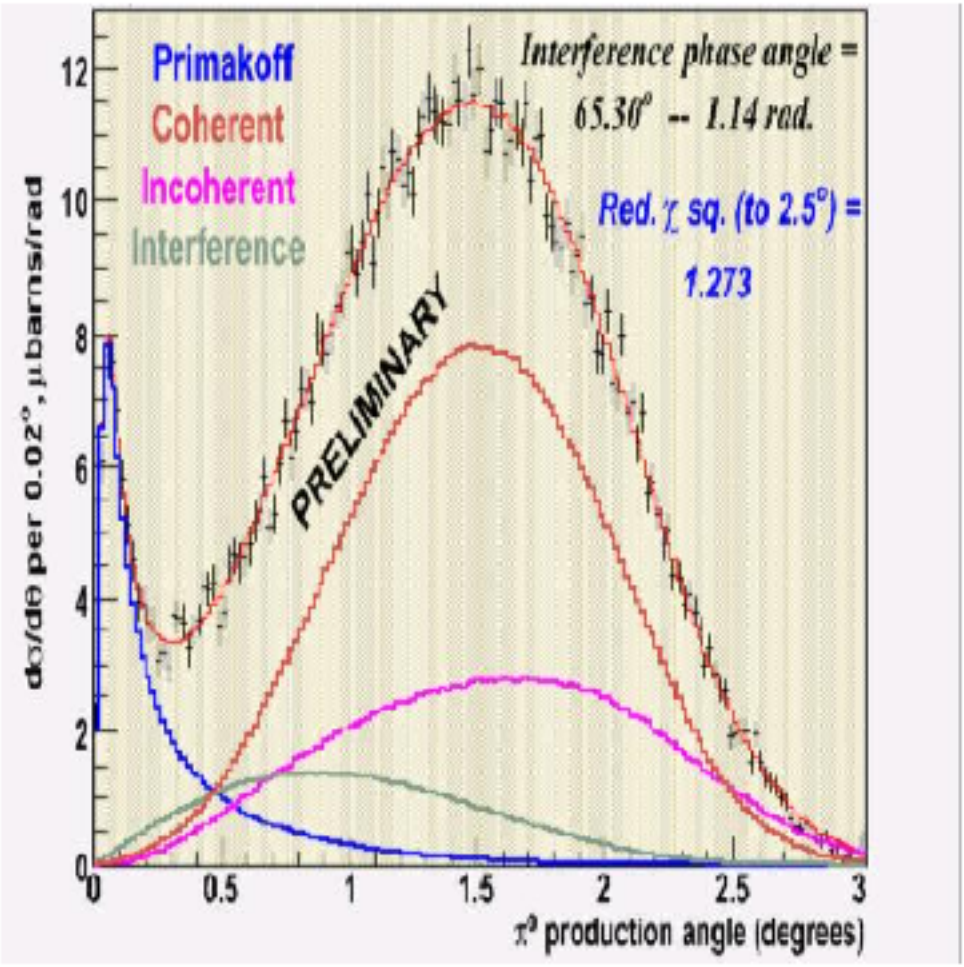
Primakoff
Coherent
Incoherent
Interference
Interference phase angle =
65.36° -- 1.14 rad.
Red. χ sq. (to 2.5°) =
1.273
PRELIMINARY
dσ/dθ per 0.02°, μbarns/rad
π⁰ production angle (degrees)
0
2
4
6
8
10
12
0
0.5
1
1.5
2
2.5
3

Figure 30:

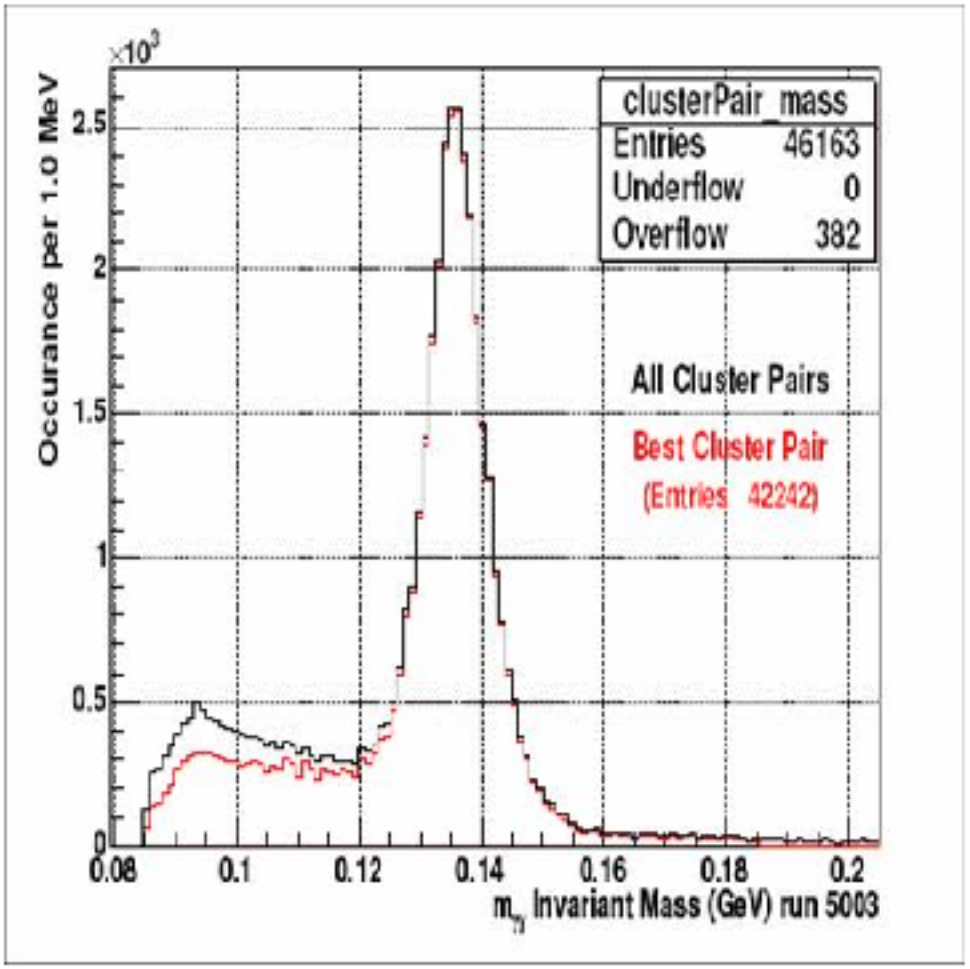
clusterPair_mass
Entries 46163
Underflow 0
Overflow 382
All Cluster Pairs
Best Cluster Pair
(Entries 42242)
Occurance per 1.0 MeV
×10³
2.5
2
1.5
1
0.5
0
0.08
0.1
0.12
0.14
0.16
0.18
0.2
m_γγ Invariant Mass (GeV) run 5003

Figure 31:

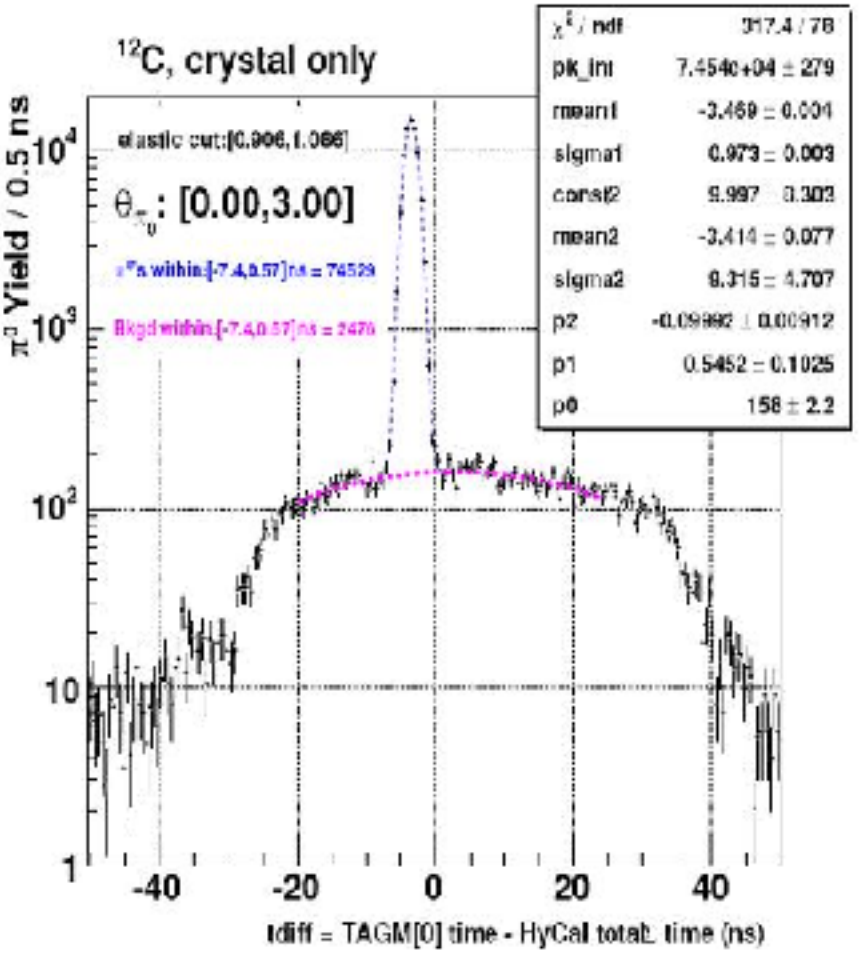
^{12}C, crystal only
elastic cut:[0.996,1.066]
θ_{π^0}: [0.00,3.00]
π^0s within:[-7.4,0.57]ns = 74529
Bkgd within:[-7.4,0.57]ns = 2470
χ^2 / ndf 317.4 / 78
pk_int 7.4540e+04 ± 279
mean1 -3.469 ± 0.001
sigma1 0.973 ± 0.003
const2 9.997 ± 3.303
mean2 -3.414 ± 0.077
sigma2 8.315 ± 4.707
p2 -0.09892 ± 0.00912
p1 0.5452 ± 0.1025
p0 158 ± 2.2
π^0 Yield / 0.5 ns
10^4
10^3
10^2
10
1
-40
-20
0
20
40
tdiff = TAGM[0] time - HyCal total time (ns)

Figure 32:

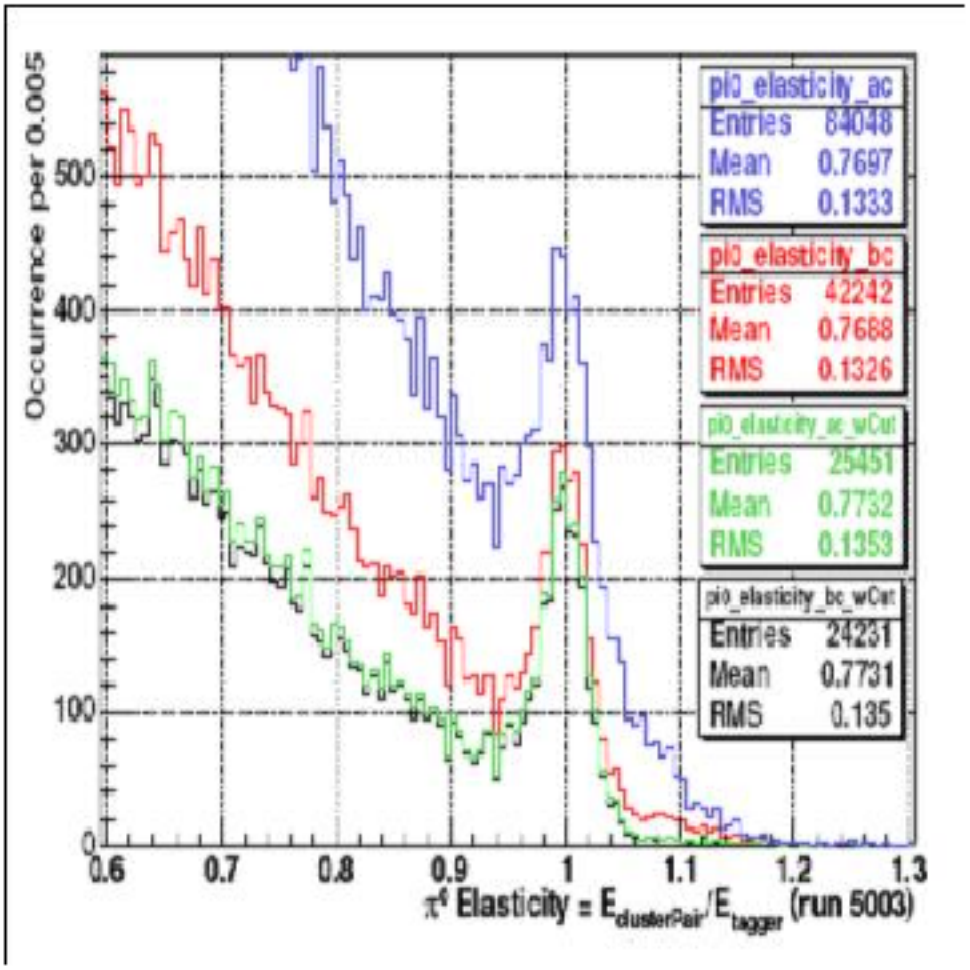
pi0_elasticity_ac
Entries 84048
Mean 0.7697
RMS 0.1333
pi0_elasticity_bc
Entries 42242
Mean 0.7668
RMS 0.1326
pi0_elasticity_ac_wCut
Entries 25451
Mean 0.7732
RMS 0.1353
pi0_elasticity_bc_wCut
Entries 24231
Mean 0.7731
RMS 0.135
Occurrence per 0.005
0
100
200
300
400
500
0.6
0.7
0.8
0.9
1
1.1
1.2
1.3
π⁰ Elasticity = E_clusterPair/E_tagger (run 5003)

Figure 33:

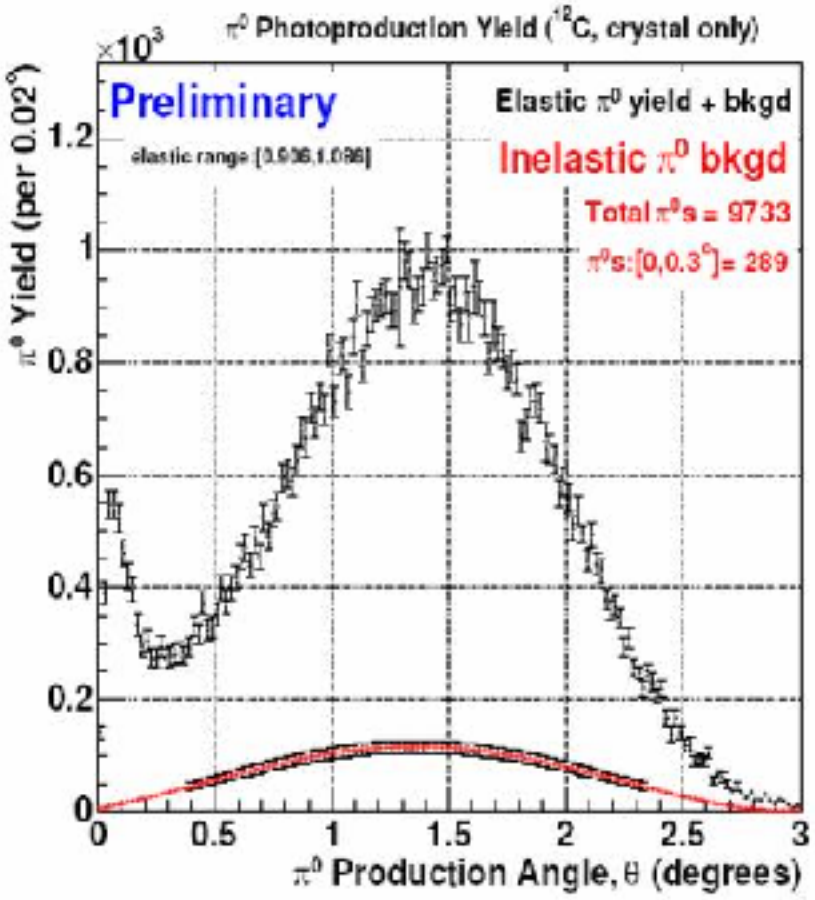
π^0 Photoproduction Yield (^{12}C, crystal only)
$\times 10^3$
Preliminary
elastic range [3.936,4.086]
Elastic π^0 yield + bkgd
Inelastic π^0 bkgd
Total π^0s = 9733
π^0s:[0,0.3°]= 269
π^0 Yield (per 0.02°)
π^0 Production Angle, θ (degrees)
0
0.2
0.4
0.6
0.8
1
1.2
0.5
1.5
2
2.5
3

Figure 34:

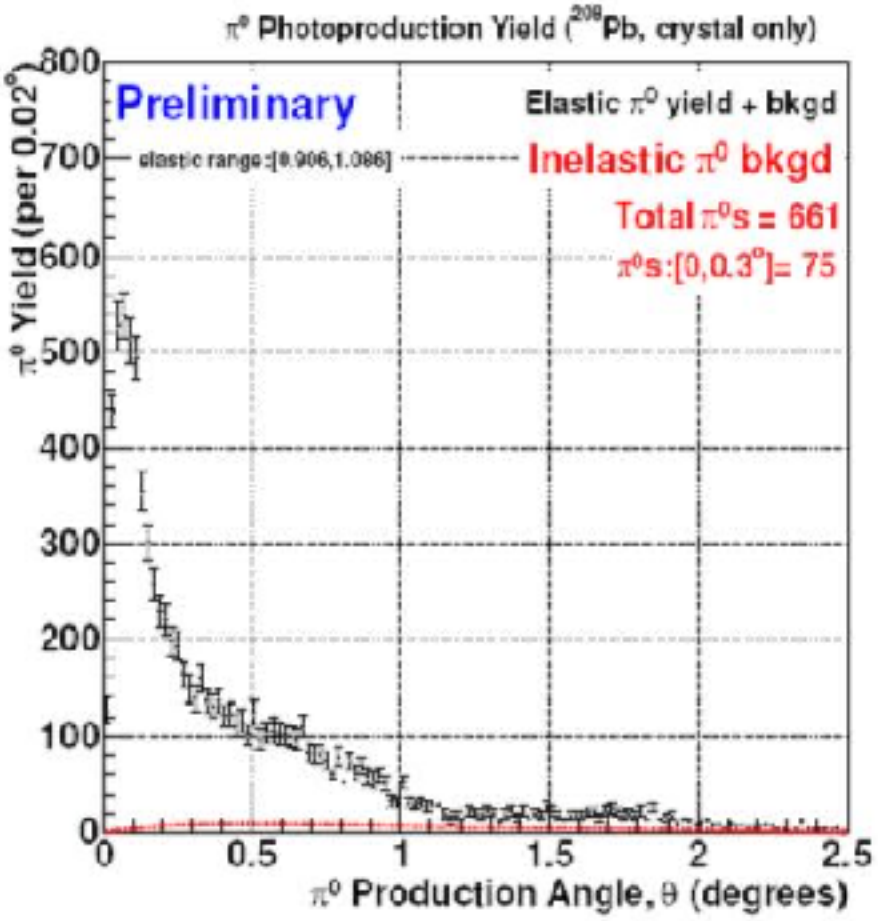
π⁰ Photoproduction Yield (208Pb, crystal only)
Preliminary
Elastic π⁰ yield + bkgd
elastic range:[0.906,1.086]
Inelastic π⁰ bkgd
Total π⁰s = 661
π⁰s:[0,0.3°]= 75
π⁰ Yield (per 0.02°)
π⁰ Production Angle, θ (degrees)
0
100
200
300
400
500
600
700
800
0
0.5
1
1.5
2
2.5

Figure 35:

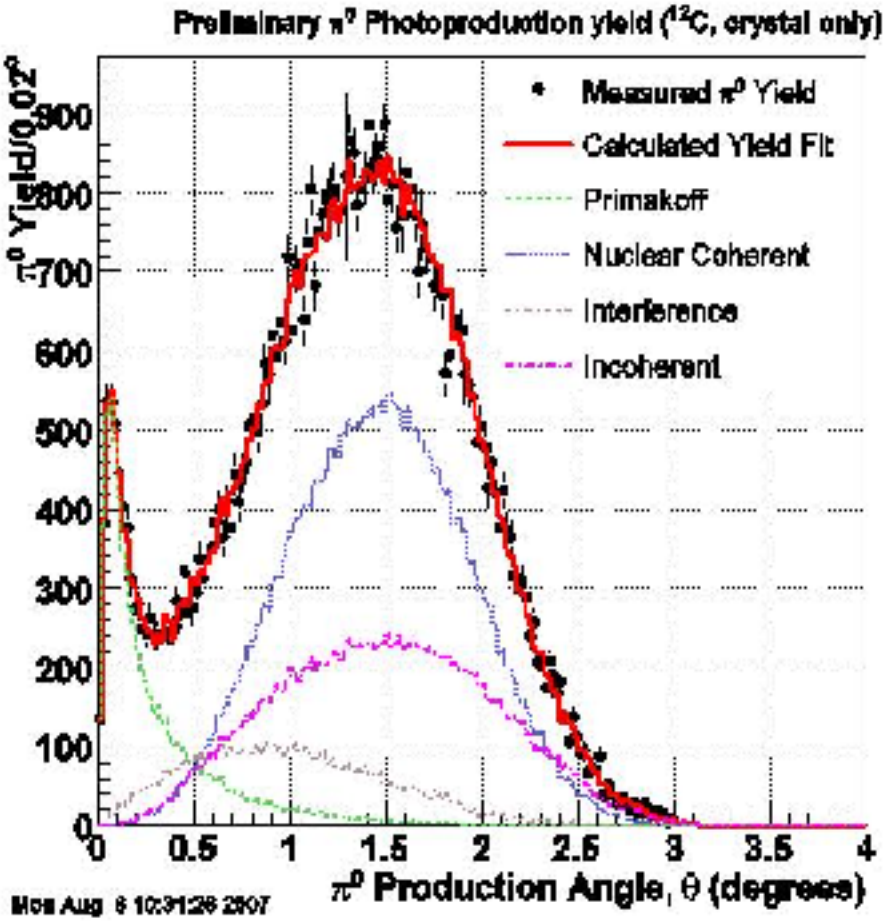
Preliminary π⁰ Photoproduction yield (¹²C, crystal only)
Measured π⁰ Yield
Calculated Yield Fit
Primakoff
Nuclear Coherent
Interference
Incoherent
π⁰ Yield/0.02°
π⁰ Production Angle, θ (degrees)
Mon Aug 6 10:31:26 2007

Figure 36:

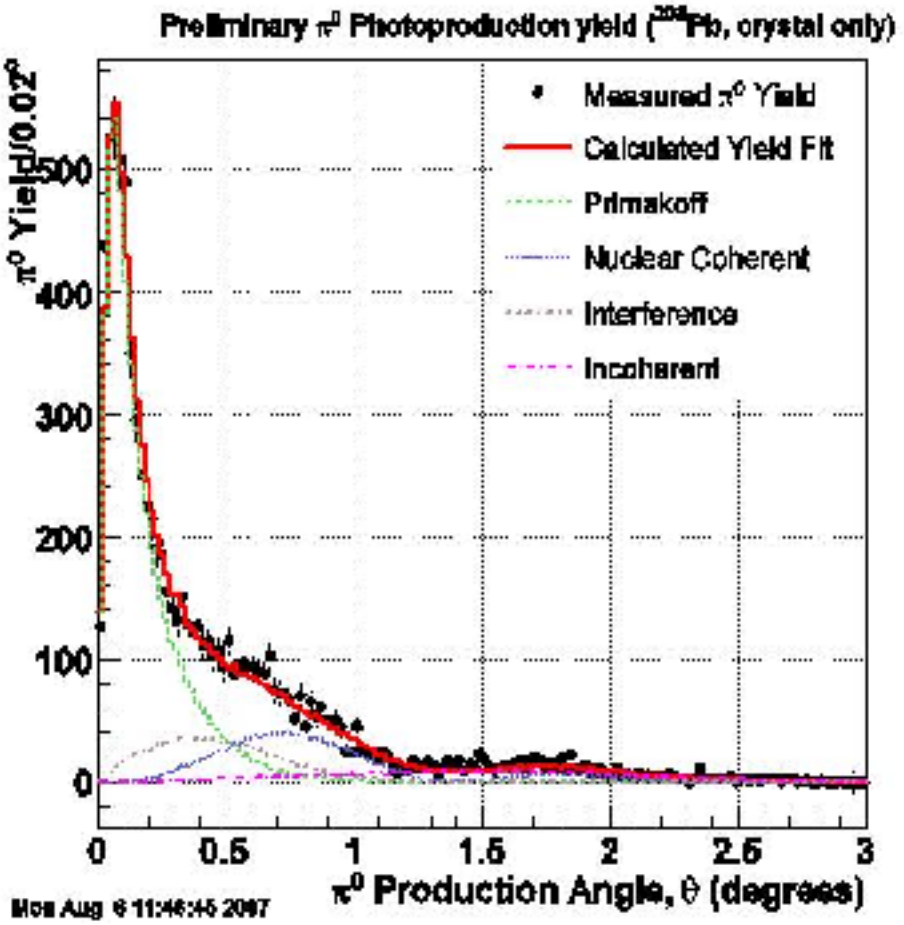
Preliminary π⁰ Photoproduction yield (²⁰⁸Pb, crystal only)
Measured π⁰ Yield
Calculated Yield Fit
Primakoff
Nuclear Coherent
Interference
Incoherent
π⁰ Yield/0.02°
500
400
300
200
100
0
0
0.5
1
1.5
2
2.5
3
π⁰ Production Angle, θ (degrees)
Mon Aug 6 11:46:45 2007

Figure 37:

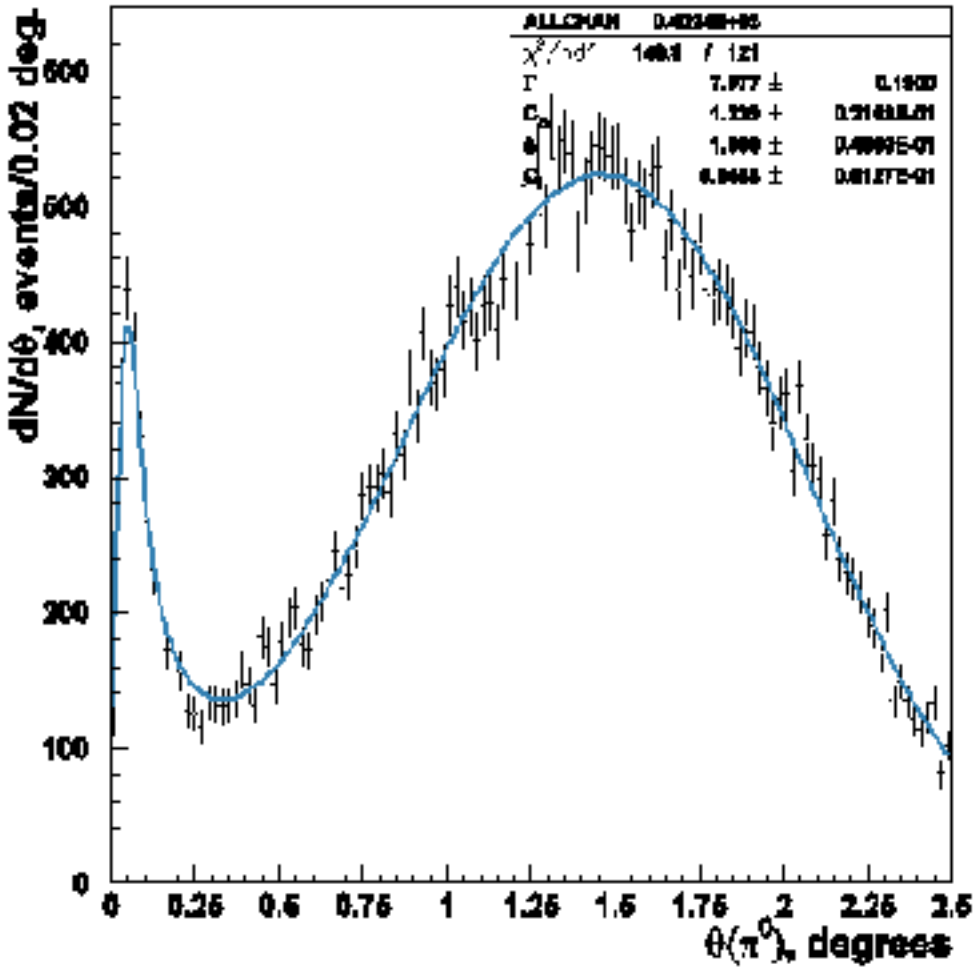
dN/dθ, eventi/0.02 deg.
θ(π⁰), degrees
0
100
200
300
400
500
600
0
0.25
0.5
0.75
1
1.25
1.5
1.75
2
2.25
2.5

Figure 38:

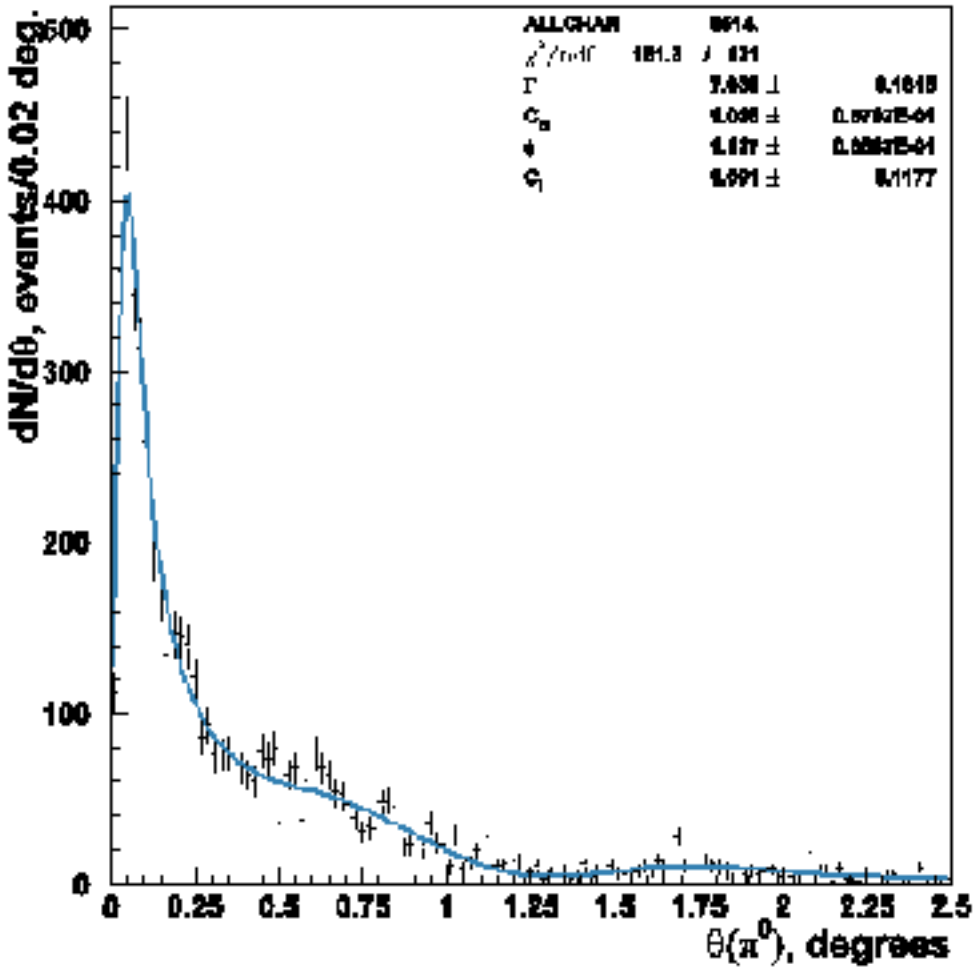
ALLCHAR
8614.
Γ
7.838 ±
0.1615
C_0
1.036 ±
ϕ
1.137 ±
C_1
0.991 ±
0.1177
dN/dθ, events/0.02 deg.
0
100
200
300
400
500
0
0.25
0.5
0.75
1
1.25
1.5
1.75
2
2.25
2.5
θ(π⁰), degrees

Figure 39:

- QED radiative corrections (of order α/π with respect to the dominant contributions): (i) virtual-photon loops and (ii) real-photon process $\gamma + A \rightarrow e^+ + e^- + A + \gamma'$, (contribution of $\sim 1 - 2\%$).

- Nuclear incoherent contribution – quasi-elastic, or quasi-free process on the proton $\gamma + p \rightarrow e^+ + e^- + A + p$ (contribution of $< 0.05\%$).

- Nuclear coherent contribution, *i.e.* virtual Compton Scattering, a two-step process – $\gamma + A \rightarrow \gamma^* + A \rightarrow e^+ + e^- + A$ (contribution of $\sim 10^{-5}\%$).

As an example, figure 40 shows the calculated energy distribution of electrons produced by $5.46 GeV$ photons on a ^{12}C target. The calculations based on three different models of atomic form factors are shown: Hartree-Fock (HF), Thomas-Fermi-Moliere (TFM) and a simpler monopole approximation introduced by Tsai. As one can see from the figure, the cross section slightly decreases compared to TFM if the HF form factor is used. The difference between the cross-section based on Hartree-Fock atomic form factor and the one based on Thomas-Fermi-Moliere model is of the order $< 1\%$ which is indicative of the accuracy of the calculations.

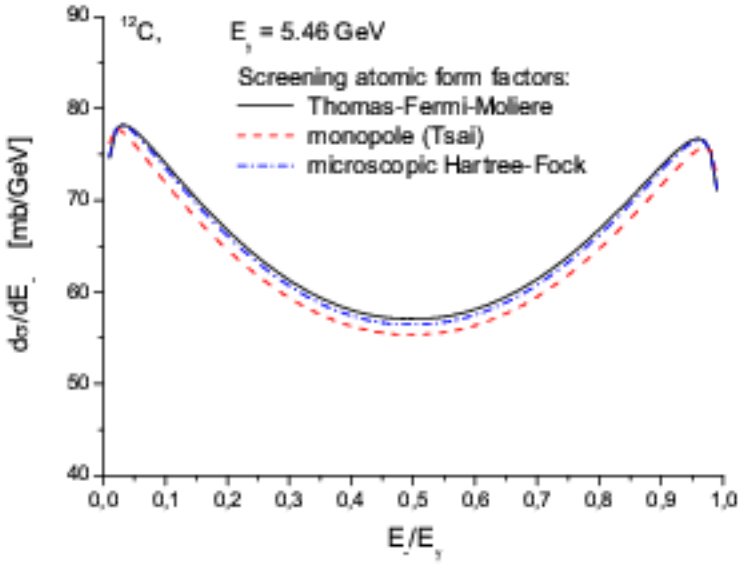

Figure 40: Calculated energy spectrum of electrons in pair-production on ^{12}C for $5.46 GeV$ photons.

A schematic of a pair-production event as seen by the *PrimEx* experimental setup (upstream of the tagger) is shown in Figure 41. For pair-production cross-section measurements, both the incident photon energy and timing information were determined by the tagger. The strength of the magnetic field of the PS dipole was lowered (to ~ 0.220 and $0.293\ Tesla \times m$) and the electron-positron pairs were swept into the calorimeter where the energy and position of the each particle was measured. The trigger signal, a coincidence between Tagger MOR and HyCal, recorded in a TDC provides timing information of the $e^+\ e^-$ - pair.

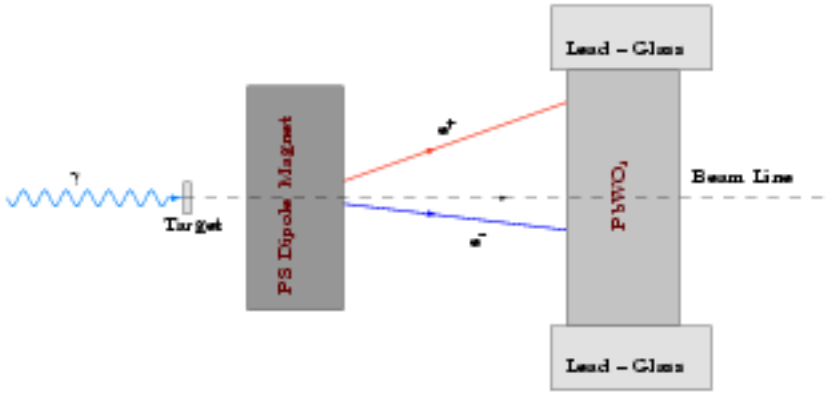

Figure 41: Schematic of a pair-production event as seen by the *PrimEx* experimental setup (top view).

Figure 42 shows distribution of X and Y coordinates and the energy position correlation for events with incident photon energy in the range $5.145 - 5.201 GeV$, *i.e.* energy bin 5 after a timing cut of $(-5\sigma, +8\sigma)$. The negative X coordinates correspond to positrons and the positive X coordinates represent electrons.

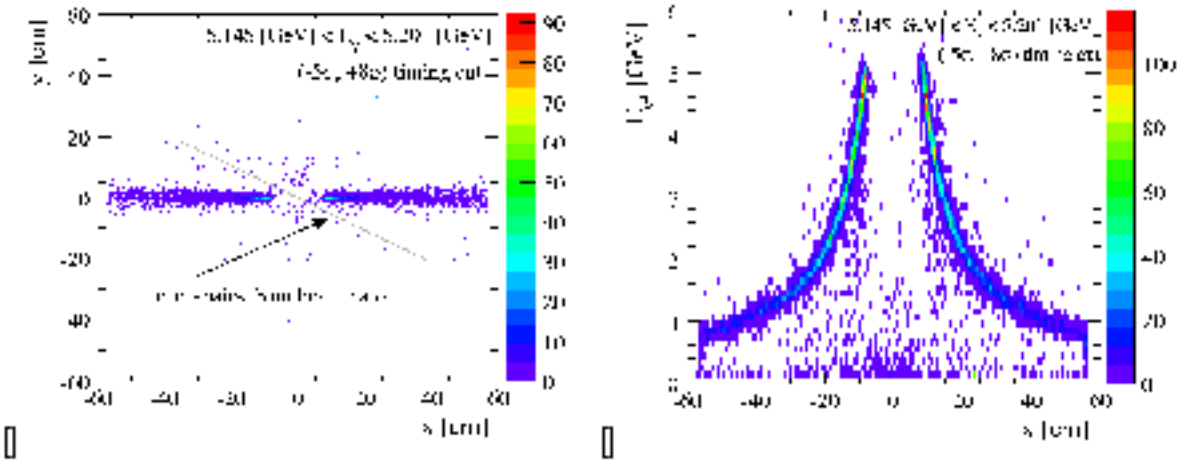

Figure 42: (a) Distribution of x and y coordinates of clusters reconstructed in HyCal. (b) Correlation of energy and deflection in the magnetic field for clusters reconstructed in HyCal.

In part (a) of Figure 42 one can see a ring of "Compton" photons around the central opening of the HyCal and a faint line with negative slope due to pair-production generated by the halo of the beam hitting the photon beam collimator upstream of the experimental target. The electrons and positrons created by the halo on the collimator are first deflected in the field of the permanent magnet in the vertical direction and then by the Pair Spectrometer dipole magnet in horizontal direction creating the sloped line.

To eliminate the e^+e^--pairs created by beam halo and most of the Compton photons, a cut on the y coordinate $|y| < 5cm$ was used. Pair production data were taken with various settings of Pair Spectrometer dipole. For the highest field setting of $\sim 0.293\ Tesla \times m$ momenta of $1.6GeV$ and less correspond to deflections in the field of the dipole of $\sim 37.17cm$ or more, *i.e* deflections into the outer Lead-Glass layer of the calorimeter. A cut of $E_{e\pm} > 1.695GeV$ on the lepton energy limits the analysis to the inner, high resolution lead-tungstate layer of the HyCal (which extends out to $\pm 35.275cm$) and enables comparison of data from runs with different field settings.

Compton electrons take most of the energy in the kinematic regime of the *PrimEx* experiment, thus a cut $E_{e\pm} > 1.2GeV$ would also eliminate a large amount ($\sim 59.9\%$) of Compton photons, some of which would otherwise be reconstructed in lead-tungstate part of the calorimeter. It is worth noting that the distributions of x and y coordinates for Compton photons are identical due to the azimuthal symmetry of Compton scattering. To subtract the background due to Compton scattering under the electron arm, a GEANT simulation involving detector resolution was performed and the resulting distribution was subtracted from the data with appropriate scaling factor.

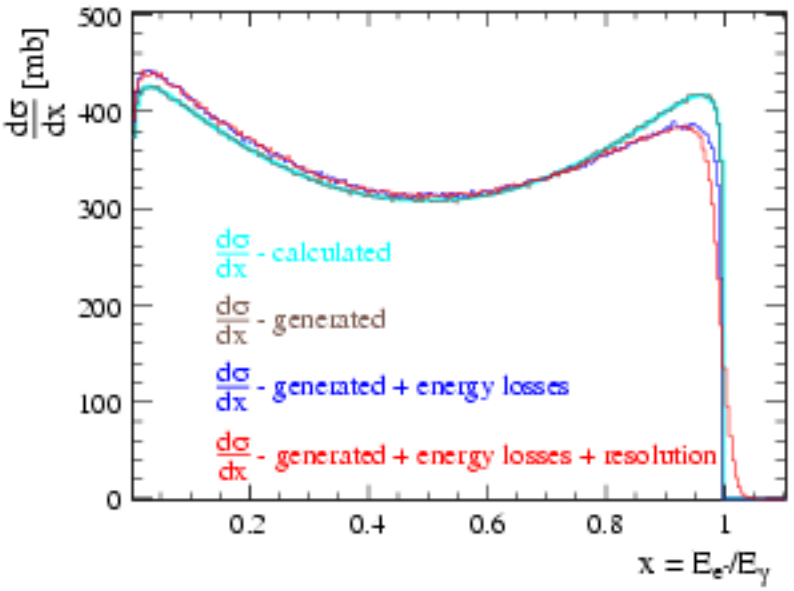

Figure 43: Absolute cross-section for pair-production differential in fraction of energy of photon taken by the electron for $E_\gamma = 4.91 - 5.46GeV$. The effect of energy losses in the target and the helium "buffer" is also shown as blue histogram.

The effects of secondary interactions (multiple scattering, Compton scattering, bremsstrahlung, *etc.*) in the target and experimental setup were simulated in GEANT by generating events according to theory and propagating them through the experimental setup. As seen in figure 43, for electrons or positrons with energy fraction $0.9 < x < 1.0$ the percent difference between calculated cross-section and the one modified by energy losses and detector resolution is changing rapidly. Hence, for this region of x one could expect up to $2 - 5\%$ descrepancy between experimental cross-sections and theory (modified by energy losses and

resolution) due to the uncertainty of the *GEANT4* calculation of the energy losses. To minimize the potential systematic errors it is preferable to compare the experiment and theory for $0.3 < x < 0.85$ where the effect of the energy losses on the cross-section is less than 5%.

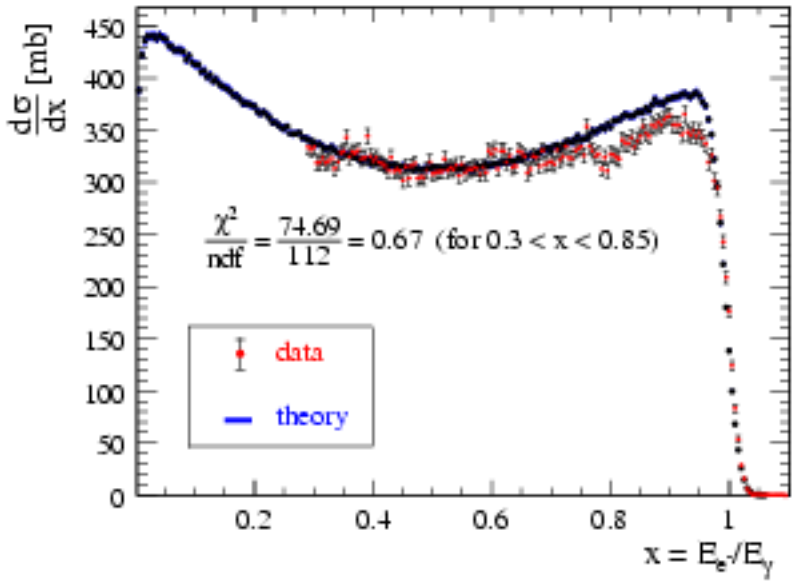

Figure 44: Differential cross-section for e^+e^--production extracted on electron arm.

Table 1 lists the theoretical and experimental pair production cross-sections for various runs integrated between x_{min} and x_{max}. Where x is the fraction of energy of the incident photon taken by the electron ($x = E_{e^-}/E_\gamma$).

Table 1: Pair production cross-section integrated between x_{min} and x_{max}.

Run Number	x_{min}	x_{max}	$\sigma_{experiment}[mb]$	$\sigma_{theory}[mb]$	$(1-\sigma_{experiment}/\sigma_{theory})[\%]$
5142	0.3	0.85	181.897	185.754	2.10
5314	0.3	0.85	188.568	185.754	−1.52
5142	0.4	0.85	149.311	152.7	2.22
5314	0.4	0.85	154.711	152.7	−1.32
5141	0.4	0.85	152.281	152.7	0.27

Table 2 summarizes the error on the experimental cross-sections listed in Table 1.

As seen above, he experimentally obtained cross-section for $0.3 < x < 0.85$ is in remarkable agreement with theory.

Table 2: Summary of errors.

	Effect	Error (%)
Statistical	Yield statistics	run dependent (~ 0.25)
	Photon flux ($R_{absolute}$ and electron counting)	run dependent (~ 0.37)
Systematical	Photon flux ($R_{absolute}$ and electron counting)	0.97
	Number of Carbon atoms in the target	0.05
	Background subtraction	0.15
	HyCal resolution	0.12
	Photon misidentification/double counting	0.06
	HyCal calibration	< 1.92
Total		$\sim \pm 0.44(stat.) \pm 2.16(sys.)$

5.4.2 Absolute cross section for electron Compton scattering

The key of the PrimEx experiment is to measure the absolute cross section of small angle π^o photoproduction from complex nuclei. The invariant mass and angle of the pion will be reconstructed by detecting two decay photons from the $\pi^o \rightarrow \gamma\gamma$ reaction in the HYCAL calorimeter. It is crucial to calibrate the overall systematic errors of the experimental setup by well known physics processes with similar kinematics and the same setup. We used atomic electron Compton scattering and the e^+e^- pair-production as tools to control systematic errors on absolute cross section measurement and the stability of the experimental setup.

The scattering of photons by free electrons $\gamma + e \rightarrow \gamma' + e'$ is one of the simplest and most basic quantum-electrodynamic processes that is experimentally accessible. The lowest order Compton scattering diagrams were first calculated by Klein and Nishina in 1929 [35], and by Tamma in 1930 [36]. There are two types of corrections to the basic Klein-Nishina formula which must be considered when studying Compton scattering at energies above 0.1 GeV. These are radiative corrections, and double Compton scattering contributions. The interference between the basic first-order single Compton scattering amplitude and the radiative and double Compton scattering amplitudes have been studied extensively in the literature [37]-[39], [40]-[41], and the errors on theoretical calculation are less than 1%. The total Compton cross section and forward cross section on ^{12}C with radiative and double Compton corrections calculated by different numeric methods[45][46] are compared as shown in figure 45 and figure 46. In the case of total cross section it is also compared to *NIST* values. They are in good agreement within 0.5%. As a result, Compton scattering provides an excellent mean to control the systematic error of PrimEx experiment on the cross section

measurement, including the photon flux, target thickness, and HYCAL calorimeter detection efficiency.

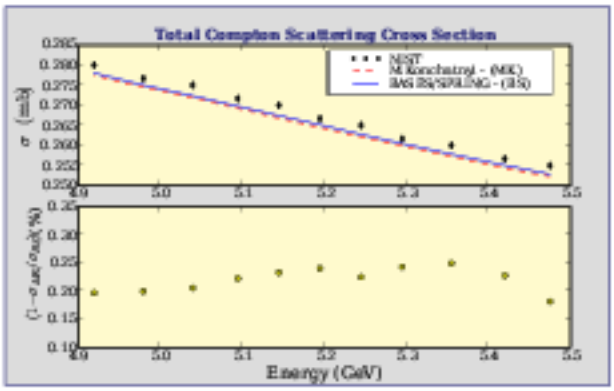

Figure 45: Comparison of theoretical calculations on Compton total cross with radiative corrections by different methods. The bottom plot shows the deviation between two different calculations is less than 0.3%.

Figure 46: Radiated Klein-Nishina cross section integrated over HYCAL solid angle.

The Compton data taken periodically once a week during our experiment in 2004. The pair-spectrometer magnet was off in order to detect both scattering photons and electrons in the HYCAL, and the lower beam intensity was used due to higher Compton cross section comparing with the π^0 production. The rest of the setup was the as same as the π^0 production runs. Detection of a Compton event is shown schematically in Figure 47. The energy and positions of the scattering photon and electron measured from the calorimeter, along with the beam energy determined by the photon tagger, provided a full kinematics on Compton event selection.

There are three groups in the collaboration analyzed the Compton data independently. The results of different analysis are in good agreement within their error bars. The preliminary result from one of the groups will be described in detail as below.

The Compton data set in this analysis were collected on a 5% R.L. carbon target with incident photon beam energies of 4.85 - 5.45 GeV. To select Compton events, the data were processed in two stages: (1) reduced skim data files, where loose cuts were applied on the raw data, and (2) Compton events selection, where optimized set of cuts were applied on skim data.

The cuts in the stage one included:

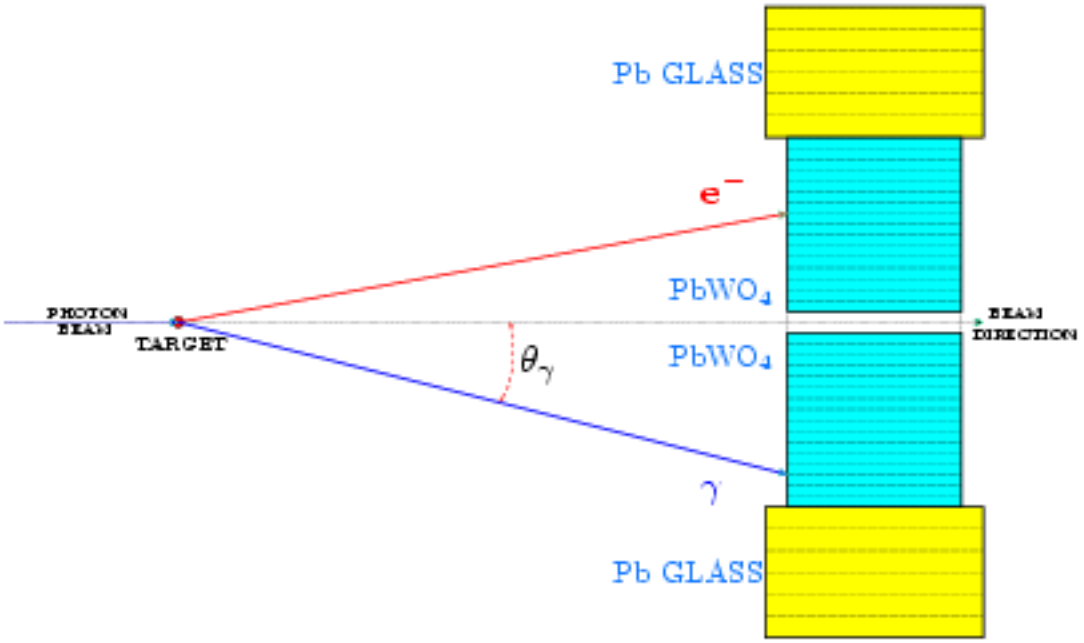

Figure 47: Detection of a single Compton event in HYCAL.

- |tdiff| $<$ 20 ns, where tdiff is the coincidence time between the photon tagger and HYCAL total sum,
- Total energy deposited on HYCAL $\sum_i E_i > 3.5$ GeV,
- $E_i > 0.5$ GeV, where $i = e', \gamma'$

The cuts in the stage two included:

- |tdiff| $<$ 5.35 ns - 5σ coincident timing cut,
- $\Delta\phi < 25^o$ - 5σ coplanarity of e',andγ' cut,
- 4.154 cm $<$ $|x_i|$ $<$ 33.232 cm - HYCAL fiducial cut, $i = e', \gamma'$,
- 4.150 cm $<$ $|y_i|$ $<$ 33.200 cm - HYCAL fiducial cut, $i = e', \gamma'$,
- -0.6 GeV $< E_{TAG} - E_0(E_1,x,y) <$ 1.2 GeV - momentum conservation cut,
- 625 cm $< z_v <$ 825 cm - interaction vertex cut,
- $R_{min} >$ 16.0 cm - minimal separation of scattering e and γ on HYCAL,
- *criss-cross* cut aimed at removing the pair production background.

where z_v is the distance from the target to HYCAL calculated by using two cluster coordinates on the calorimeter; $E_0(E_1,x,y)$ is the initial photon energy derived from the knowledge

of the energy of the higher energy cluster and the position information of both clusters on HYCAL. The GEANT Monte Carlo simulation indicates that the air production background shown in figure 48 mainly come from the collimator located upstream of the PrimEx target. The permanent magnet located between the collimator and the target bent the trajectories of electrons and positrons to HYCAL. Without the presence of magnetic field the pairs would had been undetected through the central opening in the calorimeter. About 25% of statistics were lost due to the cut to eliminate the pair production background. We plan to solve this problem in the future runs by increasing the magnetic field or replacing the permanent magnet with an active magnet. The last two cuts are shown in the figure 48.

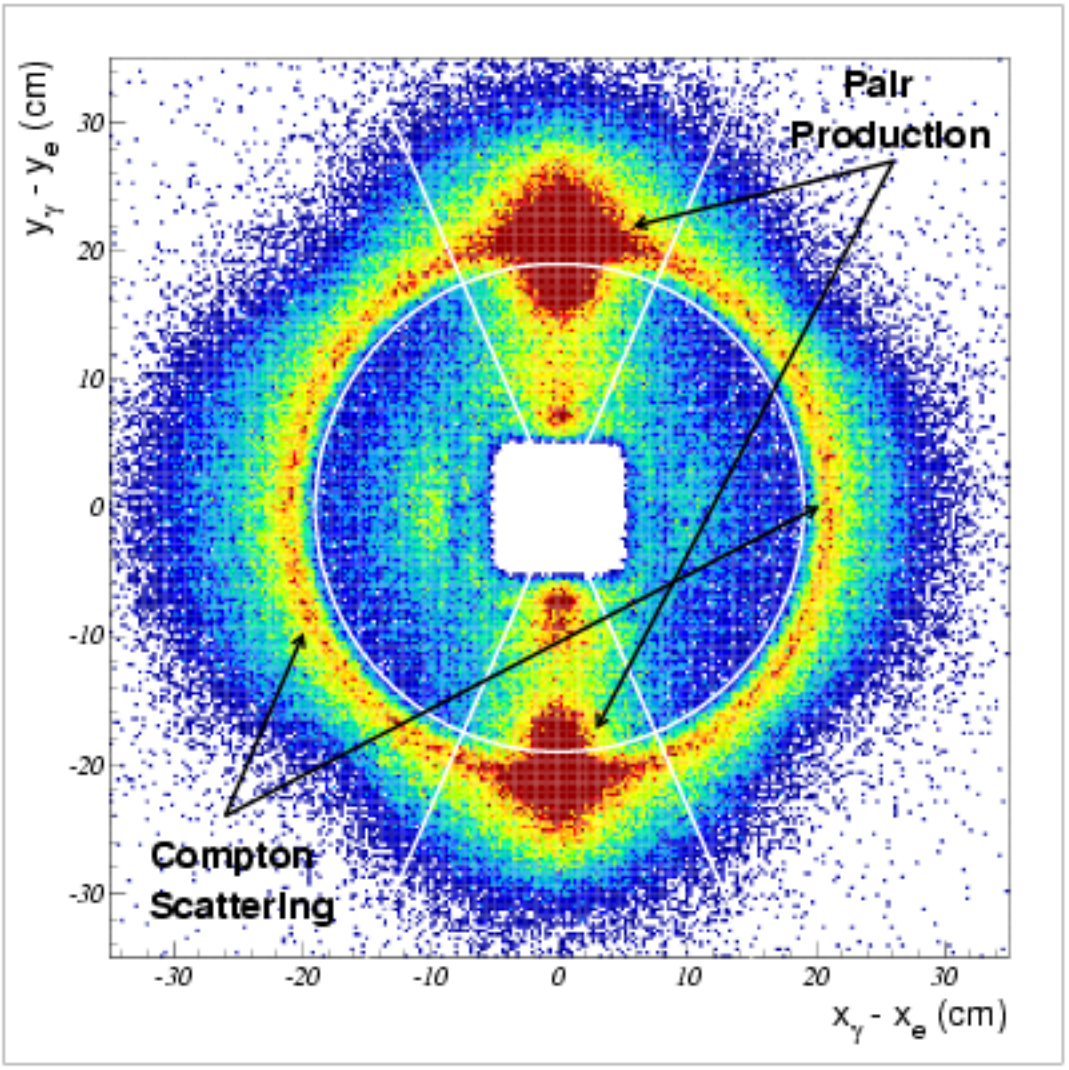

Figure 48: Event selection. Shown in the plot are two geometric cuts: (1) minimum separation cut - white circle, (2) *criss-cross* cut, white lines, that aims at removing pair production background events.

To extract final Compton yield, the elasticity distribution ($\Delta E = E_0 - (E'_\gamma + E_e)$, where E_0, E'_γ and E_e are measured energy of incident photon, scattering photon and electron) of the events, selected by using the cuts described above, were fitted with the signal and background

distributions for every $\sim 1\%$ energy bin defined by one photon tagger T-counter. The signal distribution is generated by Monte Carlo simulation based on well known theoretical angular distribution of Compton scattering including the radiative correction and double Compton contribution, detector resolution and acceptance. The same Monte Carlo program was also used in π^0 data analysis. The shape of the background is modeled with the out-of-time events selected from the data using the same cuts described above except for timing, which was changed to $|\text{tdiff}| > 5.35$ ns. Monte Carlo and background distributions were then fit to the data using maximum likelihood, as shown in figure 49. This two-parameter fit maximizes likelihood function by finding the best overall strengths for the signal and background. Then the yield is obtained by the number of events in the data after background subtraction.

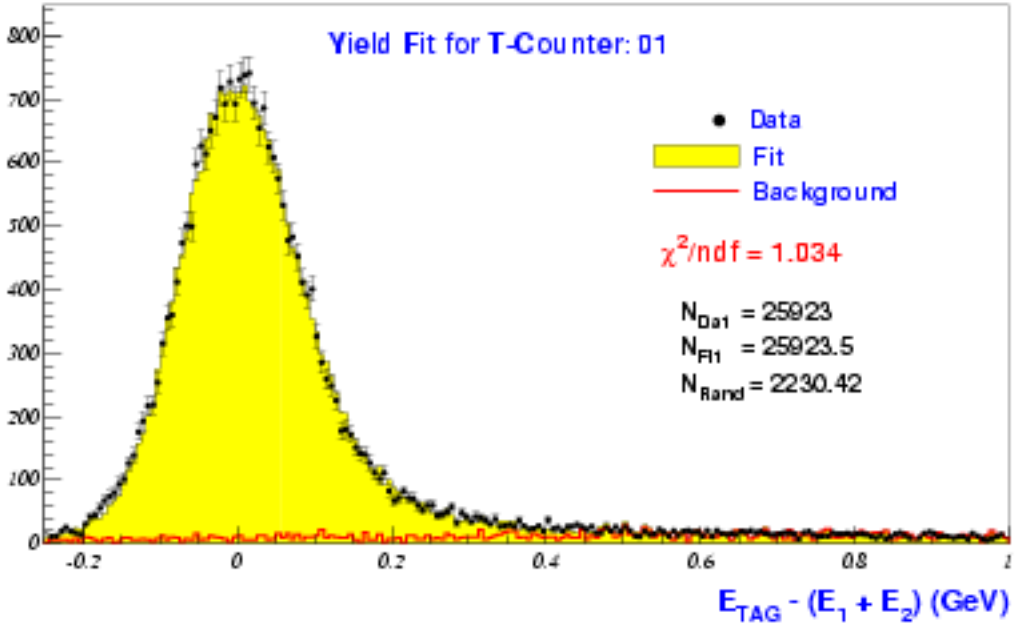

Figure 49: Yield fit, with background shown, for T counter 1.

From the extracted yield combining with luminosity and detector acceptance, the preliminary results of total Compton cross section and average differential cross section in forward direction were obtained, see Figures 50 and 51. Both measured total cross section and forward differential cross section are consistently agree with theory predictions within ?%.

Various systematic error studies are performed for each measurement point with $\sim 1\%$ energy resolution defined by one tagger T-counter. It includes contributions listed below. The result of the systematic studies is detailed in Table 3. The average systematic error of one data point is 1.37%.

- incident photon flux,
- target composition and thickness,
- coincidence timing,
- coplanarity,

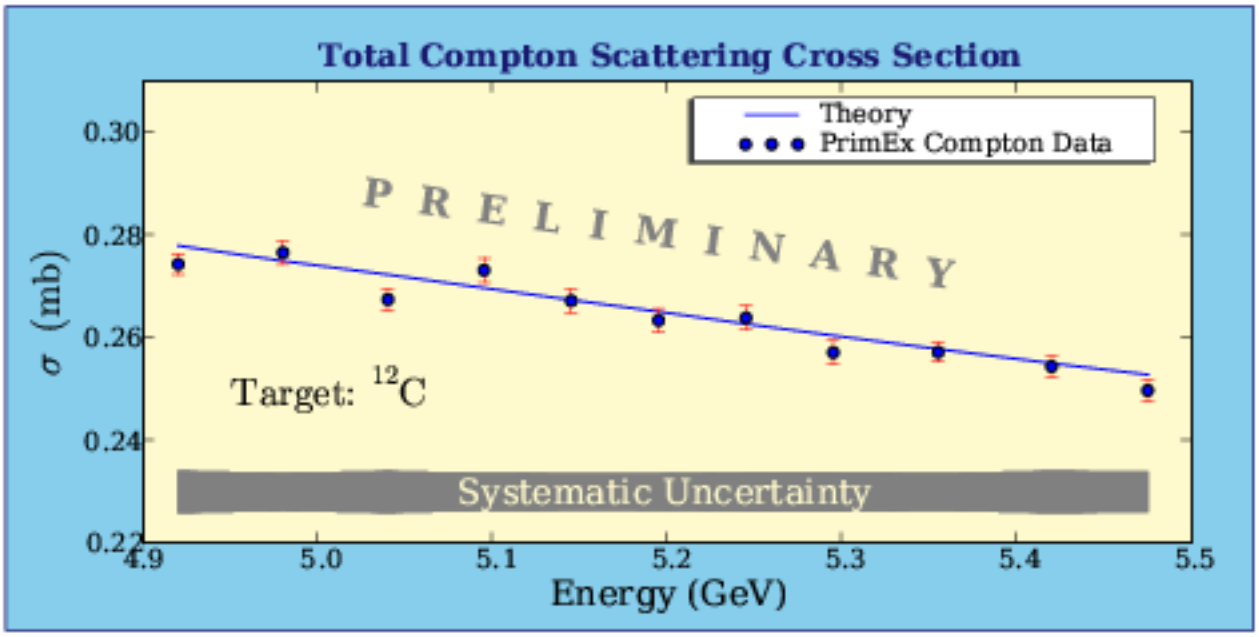

Figure 50: Total Compton cross section. The band on the plot represents the systematic uncertainty of the measurement. The energy resolution for each point is about 1%.

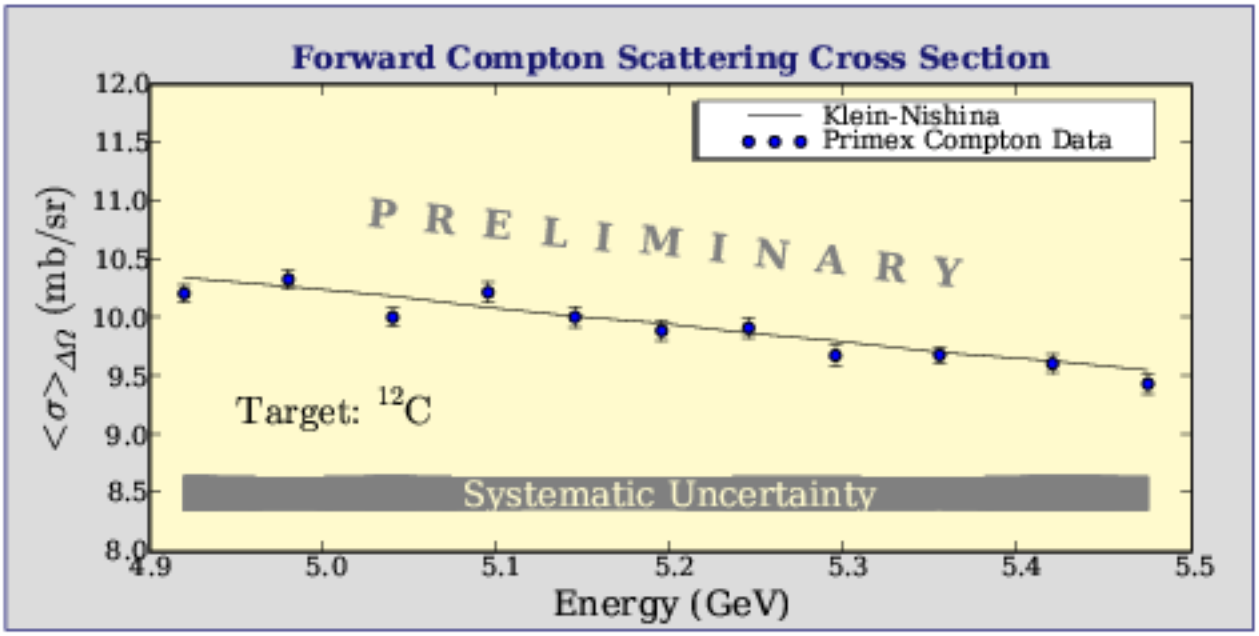

Figure 51: The forward Compton cross section averaged over the HyCal acceptance. The band on the plot represents the systematic uncertainty of the measurement.

- the dependence of the cross section on radiative tail cut,
- geometric cuts stability,
- signal-background separation,
- yield fit stability.

TCtr	Flux	Tgt	ΔT_{coin}	$\Delta\phi$	Rad. Tail	Geom.	Sg/Bg	Fit	Syst.	Stat.	Total
1	1.0	0.05	0.09	0.17	0.001	0.62	0.78	0.075	1.43	0.90	1.72
2	1.0	0.05	0.01	0.18	0.010	0.68	1.01	0.075	1.59	0.84	1.83
3	1.0	0.05	0.01	0.13	0.095	0.53	0.60	0.075	1.29	0.73	1.55
4	1.0	0.05	0.03	0.17	0.340	0.31	0.74	0.075	1.35	0.92	1.65
5	1.0	0.05	0.13	0.18	0.033	0.71	0.52	0.075	1.36	0.86	1.64
6	1.0	0.05	0.08	0.17	0.310	0.30	0.40	0.075	1.18	0.85	1.50
7	1.0	0.05	0.03	0.19	0.120	0.60	0.24	0.075	1.22	0.87	1.53
8	1.0	0.05	0.03	0.17	0.130	0.65	0.41	0.075	1.28	0.86	1.58
9	1.0	0.05	0.08	0.16	0.230	0.35	1.05	0.075	1.52	0.80	1.77
10	1.0	0.05	0.03	0.21	0.027	0.56	0.60	0.075	1.31	0.79	1.59
11	1.0	0.05	0.06	0.21	0.160	0.42	1.07	0.075	1.55	0.74	1.77

Table 3: Systematic uncertainties for each T-counter. All values are in %. Statistical error accounts for yield and photon flux fluctuations.

To increase the statistics, every two T-counts are combined together. The extracted total Compton cross sections are shown in figure 52. Both systematic and statistical errors of each data point are described in Table 4. The average total error is 1.41% for each point with ~2% energy resolution.

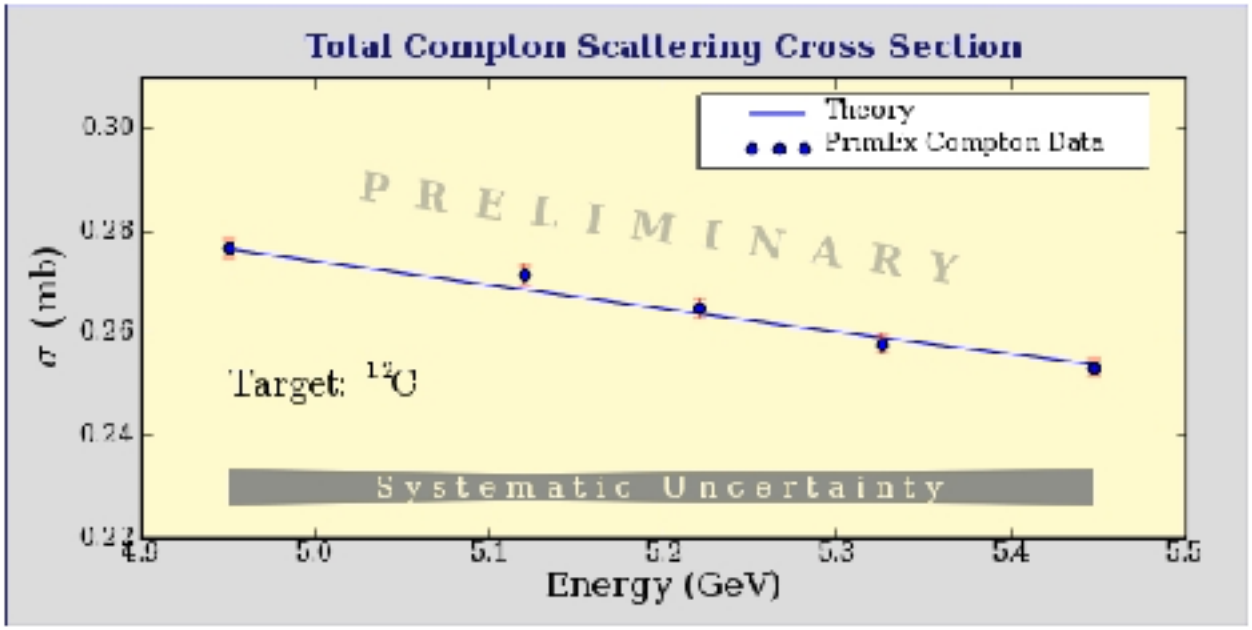

Figure 52: Total Compton cross section. The band on the plot represents the systematic uncertainty of the measurement.

In addition, by measuring Compton cross section periodically allows one to monitor the stability of the experimental setup. Figure 53 shows the total Compton cross section

TCtr	Flux	Tgt	ΔT_{coin}	$\Delta\phi$	Rad. Tail	Geom.	Sg/Bg	Fit	Syst.	Stat.	Total
1–2	1.0	0.05	0.03	0.065	0.098	0.91	0.48	0.063	1.44	0.61	1.56
3–4	1.0	0.05	0.03	0.065	0.098	0.68	0.42	0.063	1.29	0.57	1.41
5–6	1.0	0.05	0.03	0.065	0.098	0.46	0.40	0.063	1.18	0.60	1.32
7–8	1.0	0.05	0.03	0.065	0.098	0.33	0.37	0.063	1.13	0.61	1.28
10–11	1.0	0.05	0.03	0.065	0.098	0.85	0.36	0.063	1.37	0.54	1.47

Table 4: Systematic uncertainties for combined two T-counters. All values are in %. Statistical error accounts for yield and photon flux fluctuations.

changes over the run numbers. The measured values at latter runs consistently higher than predicted values, which can be directly associated with the beam leakage from other hall during the latter period of the experiment identified by the pair-production luminosity monitoring technique described in this proposal.

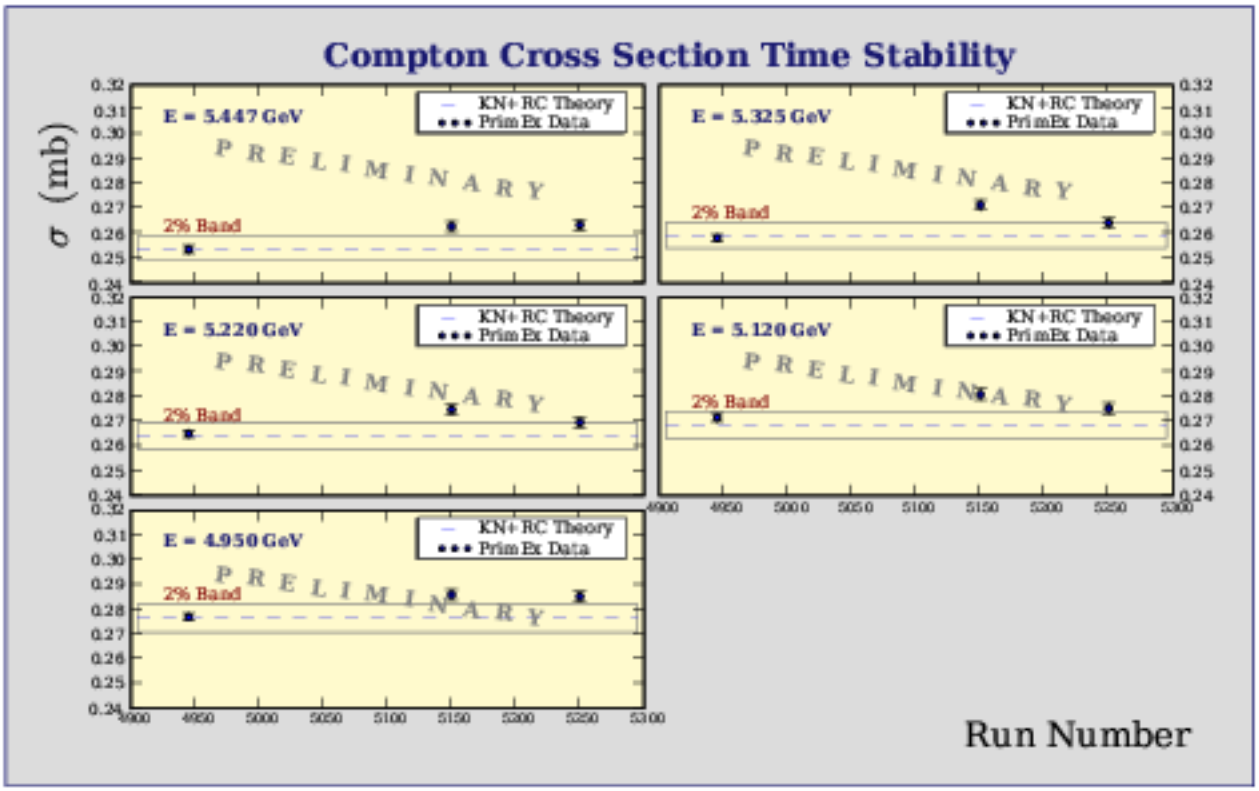

Figure 53: Total Compton cross sections change over the run numbers.

In conclusion, the total cross section and forward differential cross section of Compton scattering in 4.85 - 5.45 GeV energy range were measured with PrimEx setup. They are in excellent agreement with theory predictions with ?% precision. For each data point with a energy resolution of 2% defined by two T-counters, the average systematic error is 1.28%, the statistical error is 0.59%, and the average total error is 1.41% (see Table 4). Since Compton scattering in this energy range completely mimic the π^0 lifetime experiment, the precision obtained from the Compton measurement demonstrates that the PrimEx experimental setup has the capability to measure the absolute cross section π^0 production with a 1.4% accuracy.

6 Plans for a future run

6.1 New improvements

6.2 Run time and schedule

Calibration and setup checkout	6 days
TAC (normalization) runs	1 day
Empty target (both Compton and π^o)	2 days
Compton and e^+e^-	4 days
^{208}Pb production running	6 days
^{12}C production running	7 days

7 Summary

We are requesting the continued support of the Jefferson Laboratory management for our efforts to perform a precision test of the axial anomaly in quantum chromodynamics. The fundamental importance of this experiment is evidenced by the fact that in anticipation of the results, three independent theoretical calculations on the decay rate have been performed. The calculations based on both next-to-leading order chiral theory and QCD sum roles have indicated an increase in the width from the leading order. In our view, this provides an increased impetus to perform a measurement of this width with a precision commensurate with the theoretical knowledge. The *PrimEx* Collaboration is at present the only collaboration in a position to perform these measurements.

The Collaboration has designed, developed and constructed a multi-million dollars experimental setup which was commissioned during the first *PrimEx* run in 2004. The preliminary result from this data set has reached the error bar of $\sim 3\%$ on the π^0 lifetime. The analysis result indicates that the collaboration has the capability to control the systematic error. In order to reach our final goal of 1.4% precision, we are requesting for n days of 6 GeV beam time in Hall B. This will be one of very few fundamental tests of QCD can be performed at low energy region.

References

[1] See *e.g.* Dynamics of the Standard Model, J.F. Donoghue, E. Golowich, and B.R. Holstein, Cambridge University Press (1992).

[2] J.S. Bell and R. Jaciw, Nuovo Cimento 60A, 47 (1969). S.L. Adler, Phys. Rev. 177, 2426 (1969).

[3] R.M. Barnett *et al.*, Review of Particle Physics, Phys. Rev. D54,1 (1996).

[4] J. Bijnens, A. Bramon and F. Cornet, Phys. Rev. Lett. 61 (1988) 1453.

[5] J.F. Donoghue, B.R. Holstein, Y.C.R. Lin, Phys. Rev. Lett., vol. 55, (1985), 2766; J.F. Donoghue, B. Wyler, Nucl. Phys., B316, (1989), 289.

[6] H. Leutwyler, Phys. Lett. **B378** (1996) 313 and hep-ph/9602255.

[7] J. L. Goity, A. M. Bernstein, J. F. Donoghue, and B. R. Holstein, manuscript in preparation; J. L. Goity, talk at Baryons 2002.

[8] B. Ananthanarayan and B. Moussallam, preprint hep-ph/0205232.

[9] B.L. Ioffe and A.G. Oganesian, Phys. Lett. B647, (2007) 389.

[10] H. Leutwyler, private communication.

[11] B. Moussallam, Phys. Rev. **D51** (1995) 4939.

[12] G. von Dardel *et al.*, Phys. Lett., vol. 4, no. 1, (1963), 51.

[13] D.A. Williams *et al.*, Phys. Rev. D, vol. 38, no. 5, (1988), 1365.

[14] H.W. Atherton *et al.*, Phys. Lett., vol. 158B, no. 1, (1985), 81.

[15] H. Primakoff, Phys. Rev. 81, 899 (1951).

[16] A.M. Bernstein, Nucl. Phys. A623 (1997) 178c.

[17] G. Bellettini et al., Il Nuovo Cimento, vol. 66, no. 1, (1970), 243.

[18] V.I. Kryshkin *et al.*, Sov. Phys. JETP, vol. 30, no. 6, (1970),1037.

[19] G. Bellettini *et al.*, Il Nuovo Cimento, vol. 40, no. 4, (1965), 1139.

[20] A. Browman *et al.*, Phys. Rev. Lett., vol. 32(1974) 1067.

[21] A. Browman et al., Phys. Rev. Letts., vol. 33, no. 23, (1974), 1400.

[22] Available at the *PrimEx* web site: http://www.jlab.org/primex/

[23] A. Gil and E. Oset, Nucl. Phys. A580, (1994) 517.

[24] K. Mork and H. Olsen, Phys. Rev., vol 140, number 6B, (1965), B1661.

[25] Compact Muon Solenoid Technical Proposal, CERN/LHCC 94-38, LHCC/P1, (1994).

[26] R.Y. Zhu, et. al. IEEE Transactions on Nuclear Science, v.45, no.3,(1998).

[27] *PrimEx* Conceptual Design Report, 2000 (http://www.jlab.org/primex/).

[28] Compact Muon Solenoid Technical Proposal, CERN/LHCC 94-38, LHCC/P1 (1994).

[29] K. Mengel *et al.* IEEE Trans. Nucl. Sci. **45**, 681-685 (1998).

[30] R.Y. Zhu, *et al.* IEEE Trans. Nucl. Sci. **45**, 686-691 (1998).

[31] A. Gasparian, Calorimetry in Particle Physics, 208-214, Pasadena 2002.

[32] A. Korchin, Kharkov Institute of Physics and Technology, Kharkov 61108, Ukraine, private communication, 2007.

[33] A.V. Dolgopolov, *et al.* Preprint IHEP, IHEP-98-25, Protvino (1998)

[34] S. Danagoulian, The Light Monitoring System, PrimEx Note 53.

[35] O. Klein and Y. Nishina, *Z. Phys.*, **52**, 853 (1929).

[36] I. Tamm, *Z. Phys.*, **62**, 545 (1930).

[37] I.M. Brown and R.P. Feynaman, *Phys. Rev.*, **85**, 231(1952).

[38] Till B. Anders, *Nucl. Phys.*, 87, 721 (1967).

[39] K.J. Mork, *Phys. Rev.*, **A4**, 917 (1971).

[40] F. Mfandl and T.H.R. Skyrme, *Proc. R. Soc. London*, **A215**, 497 (1952).

[41] M. Ram and P.Y. Wang, *Phys. Rev. Lett.*, **26**, 476 (1971); *ibid.* **26**, 1210(E)(1971).

[42] A. H. Compton, Bull. Natl. Res. Counc. (U.S) 20, 19 (1922); *Phys. Rev.*, **21**, 483 (1923).

[43] G. Bellettini et al., *Il Nuova Cimento*, **66**, no. 1, 243 (1970).

[44] A. Browman et al., *Phys. Rev. Lett.*, **33**, 1400 (1974).

[45] Mykhailo Konchatnyi, PrimEx Note 37, http://www.jlab.org/primex/.

[46] A. Tkabladze, M. Konchatnyi, and Y. Prok, PrimEx Note 42, http://www.jlab.org/primex/.

8 Appendix I: Previous Experiments

8.1 The direct method

A direct measurement of the π^o lifetime can be made by observation of the decay distance between the production and decay points. This has proven difficult because of the high spatial resolution which is required due to the short lifetime, $\tau \simeq 10^{-16}$ sec. To be able to discern distinct production and decay points, one must take advantage of relativistic time dilation to have the pion survive long enough in the laboratory frame. Additionally, good knowledge of the energy distribution of the produced pions is necessary in order to extract the lifetime via this method.

The most recent result employed direct method was carried out at the CERN SPS in 1985 (shown in figure 1). In this experiment, a 450 GeV/c proton impinged upon two tungsten foils whose separation was variable. The first foil served as the π^o production target, and the second foil converted the π^o decay photons to electron-positron pairs, and the positrons were subsequently detected. By measuring the positron rates for three different foil spacings ranging from 5 to 250μm, the authors were able to determine the lifetime. The dominant

systematic errors arise from uncertainties in the π^o spectrum which was not measured but was assumed to be the arithmetic mean of the π^+ and π^- spectra. In addition, corrections had to be made for the Dalitz decay of the π^o's, conversion of the photons in the π^o production target, prompt positron and photon production, and positrons from the decay of η's. A pion lifetime of $\tau_{\pi^o} = (0.897 \pm 0.022 \pm 0.017) \times 10^{-16}$ seconds was reported[14], corresponding to a width of $\Gamma_{\pi^o} = (7.34 \pm 0.18 \pm 0.11)$ eV.

It is interesting to note that this experiment, the most precise of those performed to date, gives a result which is smaller than the leading order chiral anomaly prediction[1, 2]. Furthermore, with the latest calculations based on both next-to-leading order chiral theory and QCD sum roles described above, the discrepancy between this measurement and theory widens to more than three standard deviations. The experiment proposed here will directly address this discrepancy.

8.2 Measurements using $\gamma\gamma$ collisions

The π^o width has been measured using electron-positron collisions at DESY via $e^+e^- \rightarrow e^+e^-\gamma^*\gamma^* \rightarrow e^+e^-\pi^o \rightarrow e^+e^-\gamma\gamma$ [13]. The incident leptons are scattered at very small angles and are not detected in the final state. In so doing, they radiate quasi-real photons that couple to the π^o which is subsequently identified in an invariant $\gamma\gamma$ mass spectrum. The photons were detected using the Crystal Ball detector which consists of a large array of NaI(Tl) crystals providing 93% solid angle coverage. Contributions to the systematic error included luminosity normalization, detector efficiencies, cosmic ray rejection, and beam-gas collisions. The latter effect arises from the production of π^o's via the interaction of the leptons with the residual gas in the beam pipe. The resulting width obtained was $\Gamma_{\pi^o} = (7.7 \pm 0.5 \pm 0.5)$ eV, very close to the prediction of the anomaly but with a relatively large error. The value obtained in this experiment is the same as the Particle Data Book average but was not included in this average[3].

8.3 Measurements using the Primakoff effect

The Primakoff effect, *i.e.* photopion production from the Coulomb field of a nucleus[15], has been used in a number of experiments to study the π^o lifetime [44, 43, 18, 19]. The production of π^o's in the Coulomb field of a nucleus by real photons is essentially the inverse of the decay $\pi^o \rightarrow \gamma\gamma$, and the cross section for this process thus provides a measure of the π^o lifetime.

Using bremsstrahlung beams of energy 4.4 GeV and 6.6 GeV at Cornell, Browman *et al.*[44] measured the Primakoff cross sections on several nuclei, and obtained a total decay width of $\Gamma_{\pi^o} = (8.02 \pm 0.42)$ eV. However, as was pointed out in [16, 13] the quoted error, does not have any contribution from uncertainties in the luminosity or detection efficiency (see table 1 of [44]), and is an underestimate. An analogous measurement of the η width[20] using the Primakoff effect employing a very similar setup and analysis procedure is not in agreement with other experiments.

The other two Primakoff measurements shown in figure 1 were performed with bremsstrahlung beams of 1.5 and 2.0 GeV at DESY[43] and 1.1 GeV at Tomsk[18]. From figure 1 it can be seen that the DESY measurement is high compared to the theoretical prediction

and the Particle Data Book average. Although both of these measurements have relatively large errors they were included in the Particle Data Book average[3]. An older Primakoff experiment performed with 0.95 and 1.0 GeV bremsstrahlung beams at Frascati[19] has not been included in the Particle Data Book average and is not shown in figure 1.

In view of the strong interest in the subject, the dispersion of the previous results, and the recent availability of high intensity, high energy tagged photon beams, a high precision, state-of-the-art measurement of the π^o lifetime is needed. In past several years, PrimEx collaboration has developed an experimental setup combining existing Hall B tagged photon facility at TJNAF with a newly developed a state-of-the-art, high resolution electromagnetic colorimeter. It will enable a measurement which will offer three distinct advantages over previous measurements involving bremsstrahlung beams: (1) the quasi-monochromatic nature of the tagged beam will enable a clean kinematical separation of the Primakoff mechanism from various background processes, (2) the tagging technique will enable significantly better control of systematic errors associated with the photon flux normalization, and (3) high resolution and high efficiency electromagnetic calorimeter will enable precise measurements on the invariance mass and production angle of the π^0's. The first PrimEx experimental data set was collected in Hall B in fall 2004. The preliminary result is $\Gamma(\pi^0 \rightarrow \gamma\gamma) = 7.93 + -2.1\%(stat) + -2.0\%(sys)$ eV. More beam time is requested in this proposal to reach our final goal of $\sim 1.4\%$ precision.

9 Appendix II: Systematic Effects Relating to Photon Flux Determination

9.1 Effects of incident electron beam intensity on absolute tagging ratios

Due to rate limitations of the TAC, the absolute tagging ratios can be measured only at beam intensities which are $\sim 10^3$ times lower than the intensity of a regular production run. It is important to demonstrate that the tagging efficiencies obtained at beam intensities of $\sim 80pAmps$ are valid when applied to the data collected at the high beam intensities of about 80 to 130 $nAmps$. To investigate this, during our running period in Fall of 2004 we had normalization runs with various beam intensities ($40 - 120pAmps$).

Figure 54 (top) shows the absolute tagging ratios as a function of T-counter number measured at different beam intensities. An artificial shift was introduced on the horizontal axis in order to be able to distinguish the different measurements. As a result, one has 11 groups of 4 points (one group per T-counter). The weighted average was calculated for each of the 11 groups. Figure 54 (bottom) shows the percent deviation of each measurement from the mean value for the relevant group. No significant systematic dependence of tagging ratios on the incident beam intensity was detected when varying the beam intensity from $40pAmps$ to $120pAmps$.

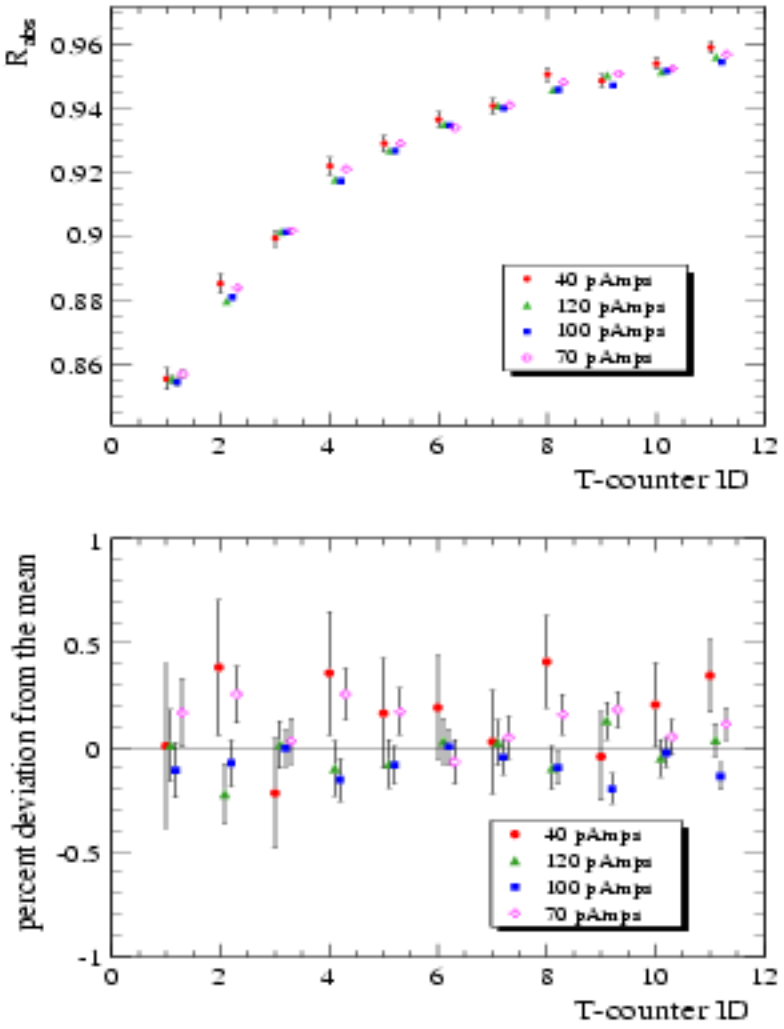

Figure 54: (top) Absolute tagging ratios plotted as a function of T-counter number for runs with different beam intensities, (bottom) The percent deviations from the mean for tagging ratio measurements made at different beam intensities for the first 11 T-counters.

9.2 Effects of collimator size

A decision was made for *PrimEx* to run with very loose collimation of the bremsstrahlung photon beam to cut out the beam halo. Together with careful monitoring of the beam position, collimation should increase the stability of the luminosity by keeping the photon beam focused at one spot on the target and thus reducing the effects of possible non uniformity of the target thickness.

Two different sizes of copper collimators were available for this purpose. In Figure 55 (top) the relative tagging ratios are plotted versus T-counter ID for data taken with 2 different collimators. For reference purposes, a result with no collimation is also plotted. For these measurements, the statistical error on each point is on the order of 0.15%. As can be

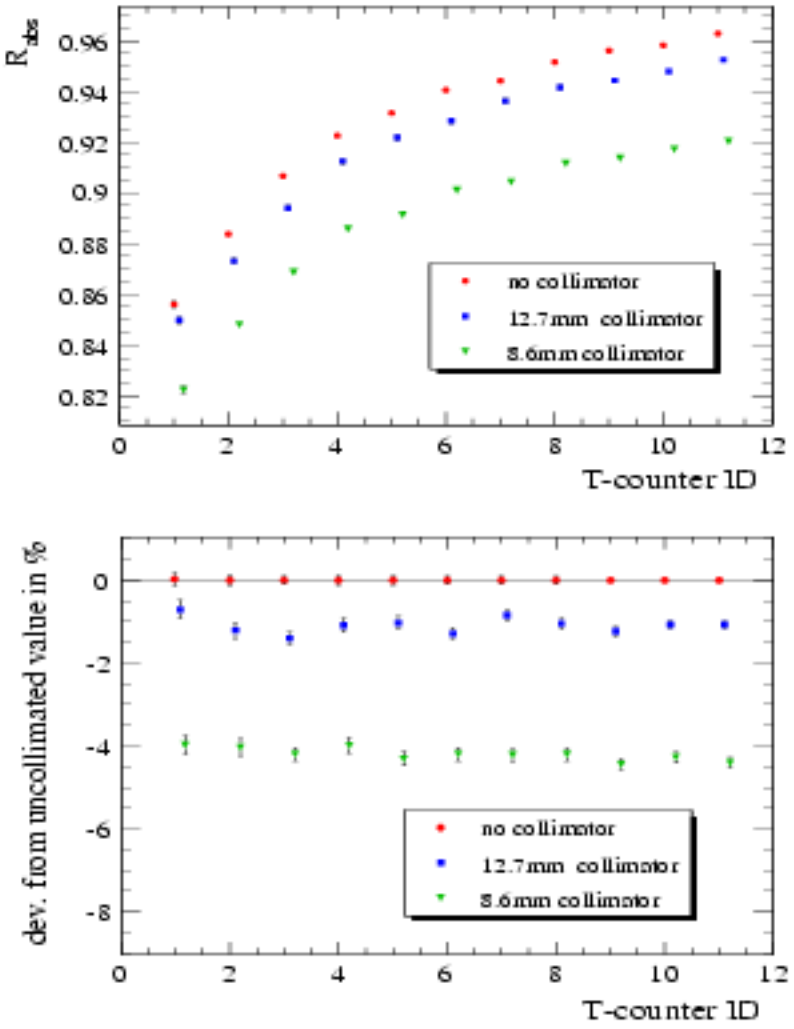

Figure 55: (top) R_{abs} measured for three different collimator sizes, (bottom). Percent deviation from the uncollimated value.

seen from Figure 55 (bottom), the $12.7mm$ collimator cuts out $\sim 1\%$ of the photon beam and $8.6mm$ collimator cuts out $\sim 4\%$ of the photon beam.

9.3 Effects of collimator position misalignment

Figure 56 shows the position of the collimator on its ladder versus run number. The entire running period can be divided up into two groups of runs – group 1) with run numbers from 4100 to 4295 with collimator at $7.075in$ and group 2) with run numbers from 4502 to 5447 with collimator at $7.02in$. Keeping in mind the required precision of 1% on the photon flux, it is important to investigate the extent to which the tagging ratios are affected by this shift.

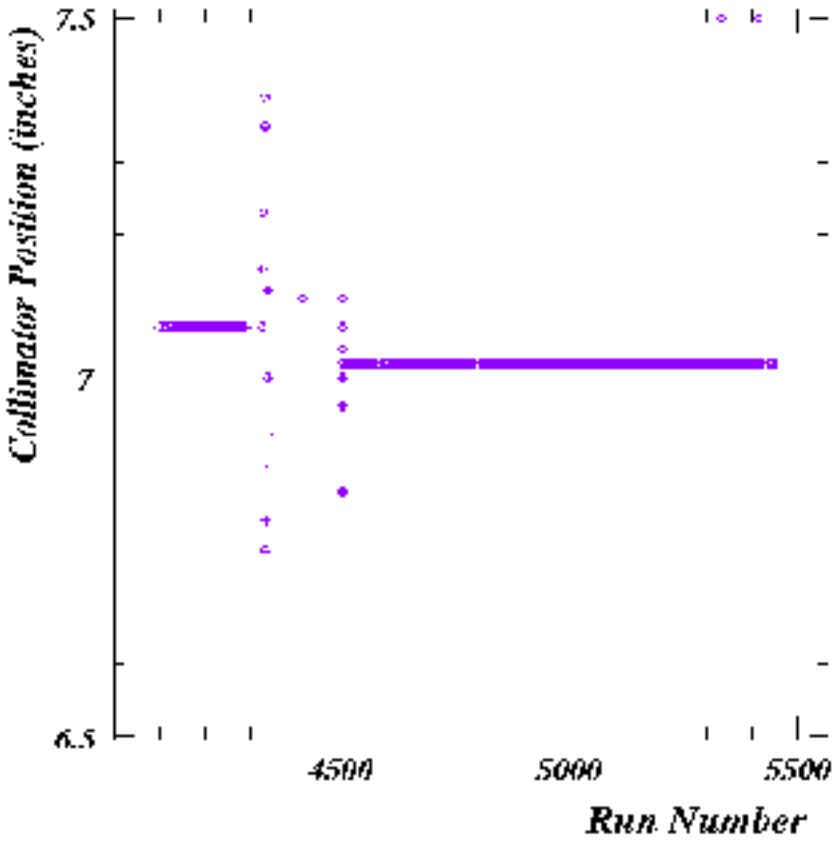

Figure 56: Collimator position vs. run number.

The tagging ratios measured for 5 different positions are shown on Figure 57 (top). Figure 57 (bottom) shows the percent deviation of tagging ratios, measured at different positions of the collimator, from the value which was measured with the collimator in its nominal position (*i.e.* at $7.02in$). From Figure 57 (bottom) one can easily see that the shift in collimator position from $7.02in$ to $7.15in$ ($\sim 3.3mm$) lowers absolute tagging ratios by about 0.34%. One can also see that larger shifts in collimator position result in $\sim 1.2\%$ or more reduction in $R_{\rm abs}$.

9.4 Effects of HyCal scraping due to beam mis-steering (uncollimated beam)

The space between the Pair Spectrometer dipole vacuum window and the face of HyCal is taken up by a helium bag. The HyCal has a central opening to allow the uninteracted beam particles to pass through. A **G**amma **P**rofiler (GP) was installed directly behind the calorimeter to monitor the shape and the position of the photon beam during the experiment. Ideally, one would place the TAC at the position of the target, but given the technical constraints in the case of *PrimEx*, the TAC was mounted on the same moving platform as the GP behind HyCal and was placed in the path of the photon beam interchangeably

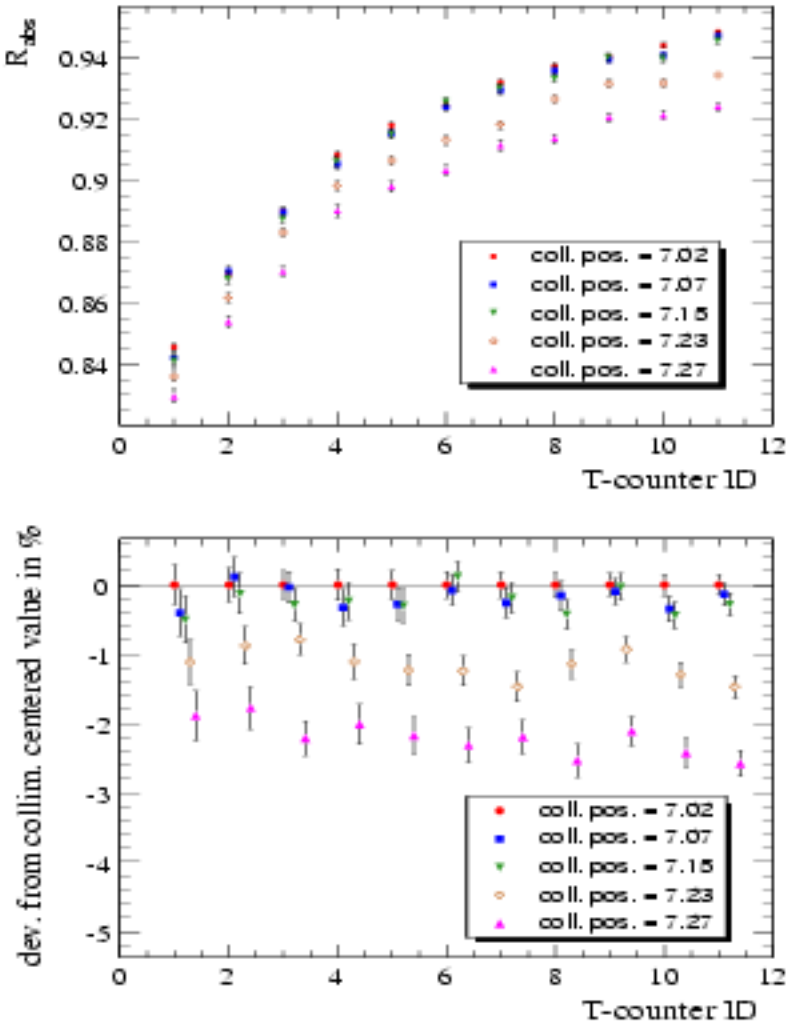

Figure 57: (top) R_{ab}, measured for 5 different collimator positions measured in inches. (bottom) Percent deviation from the measurement taken with collimator in its nominal position ($7.02in$).

with the GP to perform a normalization run. In this configuration, the photons must travel through a $4.15 \times 4.15cm^2$ central opening in HyCal before they can be registered in the TAC. Consequently, it is necessary to evaluate to what extent the size of the HyCal central opening and the alignment of the photon beam with respect to the HyCal axis affect the results of normalization runs. For this purpose the direction of the photon beam was purposefully altered and the tagging ratios were measured. To allow for larger artificial shifts in beam position, the collimator was retracted during this study. Due to the fact that this investigation was done with uncollimated beam it places an upper limit on the amount of the photon beam that can be cut by HyCal due to scraping. Because the GP was mounted on the same moving platform as the TAC, photon beam position measurements were possible

only before and after a normalization run. In light of this, the study described in this section should be considered only as qualitative exercise.

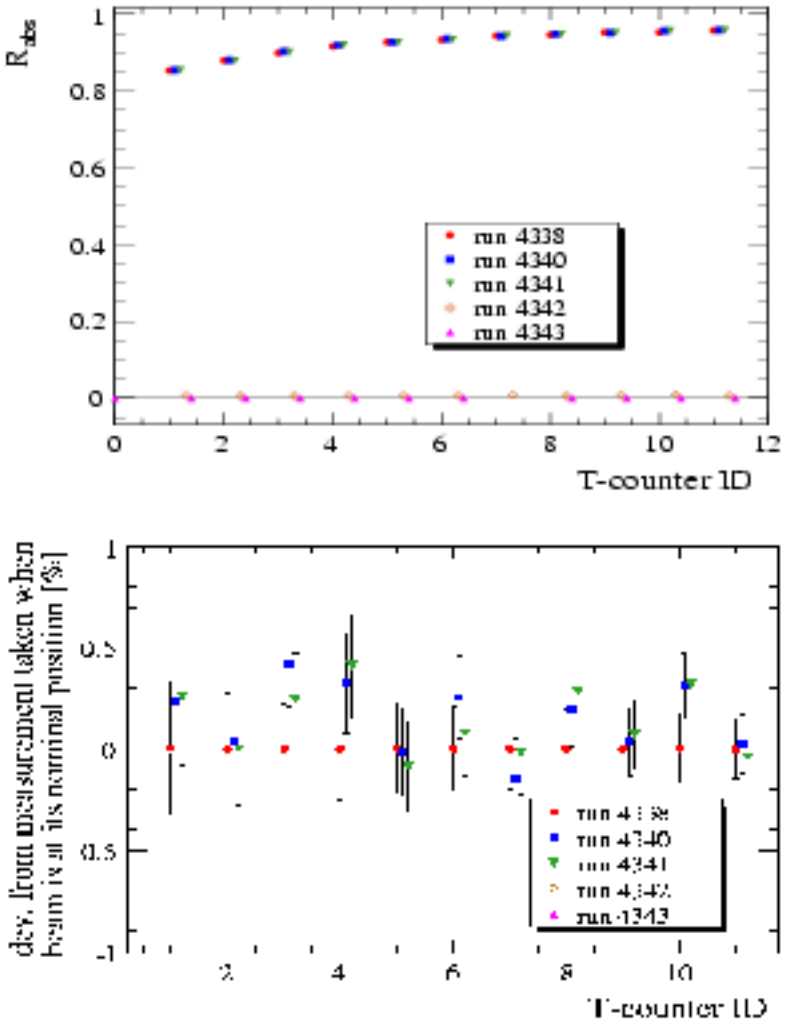

Figure 58: (top) R_{abs} measured for five different beam angles. (bottom) Percent deviation from the uncollimated value.

It was determined that in the absolute coordinate system of the GP, the nominal photon beam position is: $x_{av} = -0.83mm$ and $y_{av} = -1.45mm$. Figure 58 (top) shows several measurements of tagging ratios with different beam positions. Run 4338 was taken with the beam at its nominal position. For run 4340 the beam was steered a little over $5mm$ in positive y direction to $(-0.93, 4.09)$. For run 4341 the beam was at $(-6.54, -1.23)$. During

run 4342 beam was at $(-9.45, -1.52)$ – *i.e.* about $8.5mm$ off of its nominal position. For run 4343 the beam was at $(5.12, -1.44)$ – *i.e.* about $6mm$ off of its nominal position.

This qualitative study indicates that the HyCal and the beam were not positioned ideally with respect to each other. Runs 4342 and 4343 indicate that a $\sim 8.5mm$ shift in the beam position in the negative direction has the same effect on the tagging ratios as a $\sim 6mm$ shift in the positive direction along the x axis. Also runs 4340 and 4341 indicate a slight increase ($\sim 0.23\%$) in tagging ratios when the beam is steered $5mm$ in the positive y direction or $5mm$ in the negative x direction.

9.5 Long and short term reproducibility with uncollimated beam

To test our ability to perform a consistent measurement of the absolute tagging ratios, $R_{absolute}$, we had back-to-back normalization runs which were taken only $20 - 25$ minutes apart. The pair spectrometer magnet was operating at $\sim 900 Amps$.

As can be seen from Figure 59, the study shows that all four runs agree within the limits of required precision and statistical errors. Figure 60 (top) shows the absolute tagging ratios measured for the first 11 T-counters. These runs were taken roughly four and a half hours and 5 days apart from each other. Figure 60 (bottom) shows the percent deviation of the tagging ratio for each T-counter from the relevant average value. The statistical error for each point is on the order of 0.2%. As seen from the plots, all three measurements are in very good agreement with each other (better than 0.3%). Note that since all three measurements were taken with different settings of the Pair Spectrometer dipole, this study also shows that there is no detectable dependence of absolute tagging ratios on the magnetic field of the PS dipole when using an uncollimated photon beam.

9.6 Effects of the PS dipole field with collimated beam

As was already demonstrated in Section 9.5, the PS dipole field has no measurable effect on the tagging efficiencies in the case of an uncollimated photon beam. Due to technical difficulties with the PS power supply, the normalization runs were performed at different values of the magnetic field of the PS dipole, and the production data for *PrimEx* were taken with a $12.7mm$ collimator, it is important to investigate the effect of the magnetic field on the tagging ratios measured for a collimated beam. The results of these studies are summarized in figure 61.

9.7 Absorption in the target

Some of the photons are absorbed in the target without producing a π^0. Special TAC runs with a carbon target placed in the beam were performed to study this effect. Figures 62 and 63 show a comparison of tagging efficiencies measured for target in runs to those measured for target out runs for measurements performed without and with photon beam collimation. Both studies yield consistent results indicating that $\sim 3\%$ of photons are lost in the target.

Since *PrimEx* is aiming for a $\sim 1.5\%$ level absolute cross-section measurement, one has to correct the yields for absorption of photons in the target. The main reaction of interest for *PrimEx*, $(\pi^0 \rightarrow \gamma\gamma)$ and the consistency check reactions (Compton effect and e^+e^- production) are affected by the photon absorption in the target at different levels. In the case of Compton and Primakoff effects, not only the primary photon but also the secondary photons can be absorbed in the target. Since Compton scattering or π^0–production can happen anywhere along the longitudinal direction of the target, the result of this study can be used to set an upper limit on the effect of photon absorption.

10 Appendix III: Target thickness determination

We propose to use two targets in this experiment, ^{12}C and ^{208}Pb. The carbon target is approximately 380 mil thick (5% R.L.) and uses Highly Ordered/Oriented Pyrolitic Graphite (HOPG) as the target material. The lead target is a rolled metal target approximately 12 mils thick (5% R.L.) and uses 99% enriched ^{208}Pb as the target material. The uncertainties in the effective areal densities of the carbon and lead targets are 0.05% and 0.43%, respectively. Both targets were utilized in the first *PrimEx* run. In this section the methodology for mapping the effective areal densities of the targets $(atoms/cm^2)$ and the estimated errors are described. Most details of the analysis can be found in *PrimEx* note #28.

A micrometer with precision of $\pm$ 0.05 mils was used to make a map of the thickness of the HOPG target. Figure64 shows the micrometer map points, and the measured thicknesses in the central region of the target are also shown. The thickness varies by approximately 0.04% over the central region of the target. The mass density of the HOPG material was measured using the water immersion technique. HPLC grade water was used, which is submicron filtered, packed under inert gas, and has a maximum limit of impurities of 1 ppm. Corrections were made for the temperature dependence of the water density. A microgram scale was used to weight the target block in air and in the water. The mass densities of two identical HOPG blocks were measured three consecutive times, and the results are shown in figure 65. The HOPG mass density used in calculating the areal density of the target was the average of the first five measurements (trial #6 was excluded), and the error in mass density is taken from trial #3.

Two corrections were applied to ρT to obtain the effective areal density of the target. The first correction is for impurities in the target, which can produce neutral pions through the Primakoff process. The second accounts for the attenuation of the incident photon beam in the target. The NIST XCOM data base was used to calculate the effect of incident beam absorption. Magnetic Primakoff production from ^{13}C is very small compared to Coulomb

Primakoff production, and can be neglected. The final result for the effective number of ^{12}C $atoms/cm^2$ in the target is: $N_{eff}(Z=6) = 1.0461 \times 10^{23} atoms/cm^2 \pm 0.05\%$.

The lead target was manufactured by Oak Ridge National Laboratory, and is a rolled foil of isotopically enriched ^{208}Pb, with 99% purity. The thickness of the target is approximately 12 mils, which corresponds to 5% radiation length. Because the target is a thin foil that can be easily damaged, direct measurements of foil thicknesses using a micrometer were considered risky. For this reason, an alternative method was devised which utilized x-ray attenuation to measure the foil thickness. X-rays from the 60 keV line in ^{241}Am were collimated to a spot size of approximately 2 mm in diameter. X-rays that passed through the target were detected in a 1 inch diameter NaI detector located behind the target foil. By comparing the attenuation of x-rays through the foil at various points, the thickness at these points can be determined. X-Y stepper motors were used to scan the lead target over the ^{241}Am source, and a map of x-ray attenuation *versus* target (x,y) was obtained. Two target scans were performed; the first was a run with 200 mil step sizes, and then a second run about a month later with 100 mil steps. Since the x-ray absorption constant for lead is not known with sufficient accuracy for our needs, the constant was measured at four off-center points on the target. This was done by taking x-ray attenuation and micrometer measurements at those points during the 200 mil and 100 mil step runs. Figure 66 shows the results of the study. For a given step size, the four measurements of x-ray absorption agree. However, there is a shift when comparing the results with the 200 mil step versus the 100 mil step size. To keep the analysis consistent, the 200 mil absorption constant was applied to the 200 mil step data, and the 100 mil absorption constant was applied to the 100 mil step data. The consistency of the analysis can be checked by verifying that the target thicknesses obtained in both scans agree within errors. The target thickness map from the 100 mil step scan is shown in Figure 67. The plot indicates a plateau near the center of the foil. The apparent increase in thickness at the very corners of the data is most likely caused by the target frame. Figures 68 and 69 show crosscuts through the lead target along the y and x axes, respectively. Results from both the 100 mil and 200 mil step scans are shown on the plots, and there is good agreement between the two data sets. The crosscuts clearly indicate a plateau near the center of the target that extends out to a radius of 200 mil. During the 2004 *Primex* run, the target ladder was positioned so that the beam went through the center of the lead target to take advantage of the relatively uniform target thickness in this area of the target. The areal density of the lead target was calculated using the average of lead mass densities listed in the literature. Corrections were applied to account for the effects of impurities in the target, and for attenuation of the incident beam. The result is $N_{eff}(Z=82) = 9.875 \times 10^{20} \pm 0.43\% atoms/cm^2$.

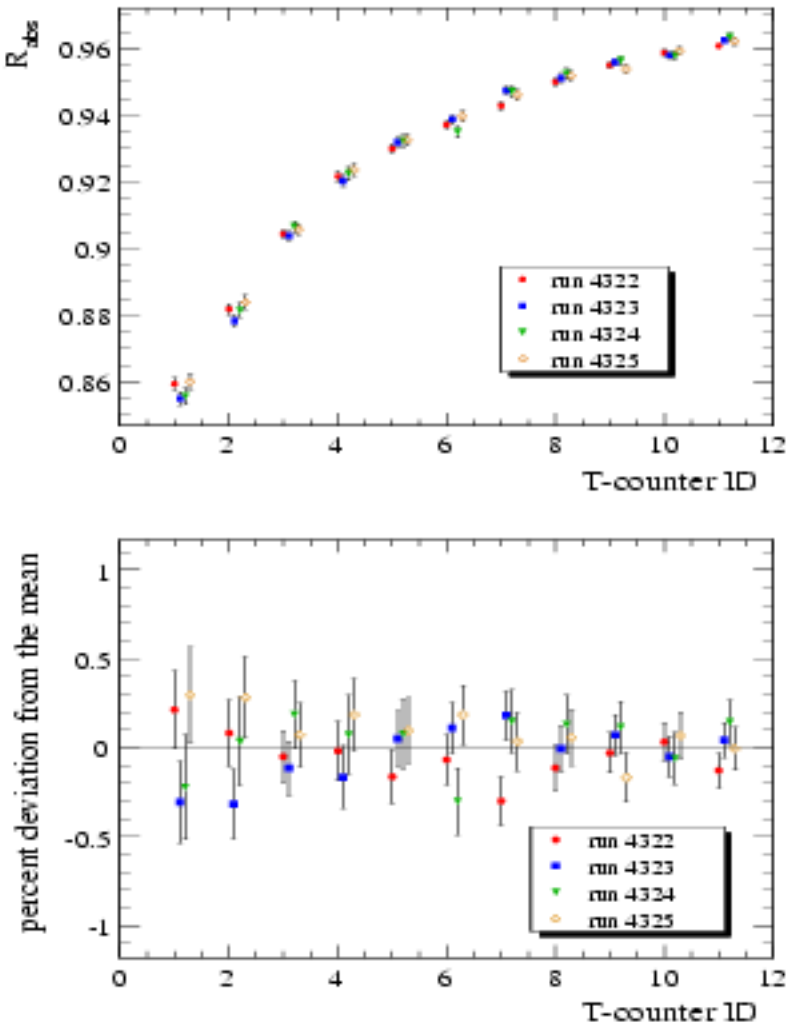

Figure 59: (top) R_{abs} measured for four consecutive runs. (bottom) Percent deviation from the mean.

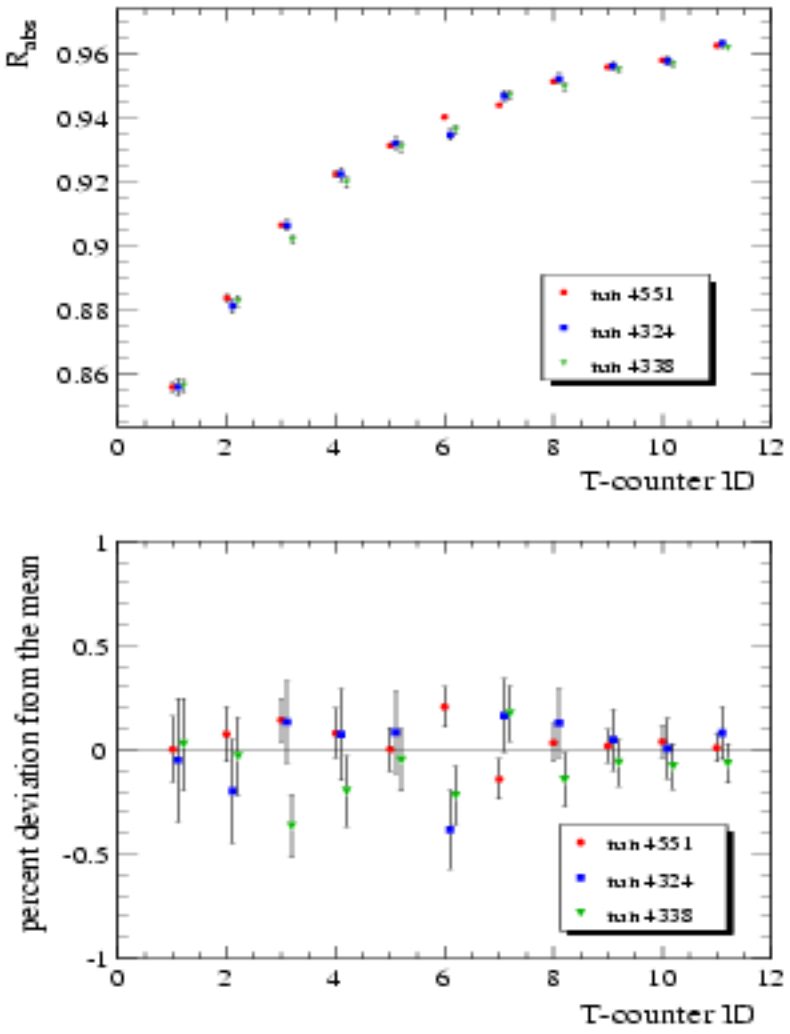

Figure 60: (top) R_{abs} measured for three runs which were separated in time during our data taking. (bottom) Percent deviation from the mean.

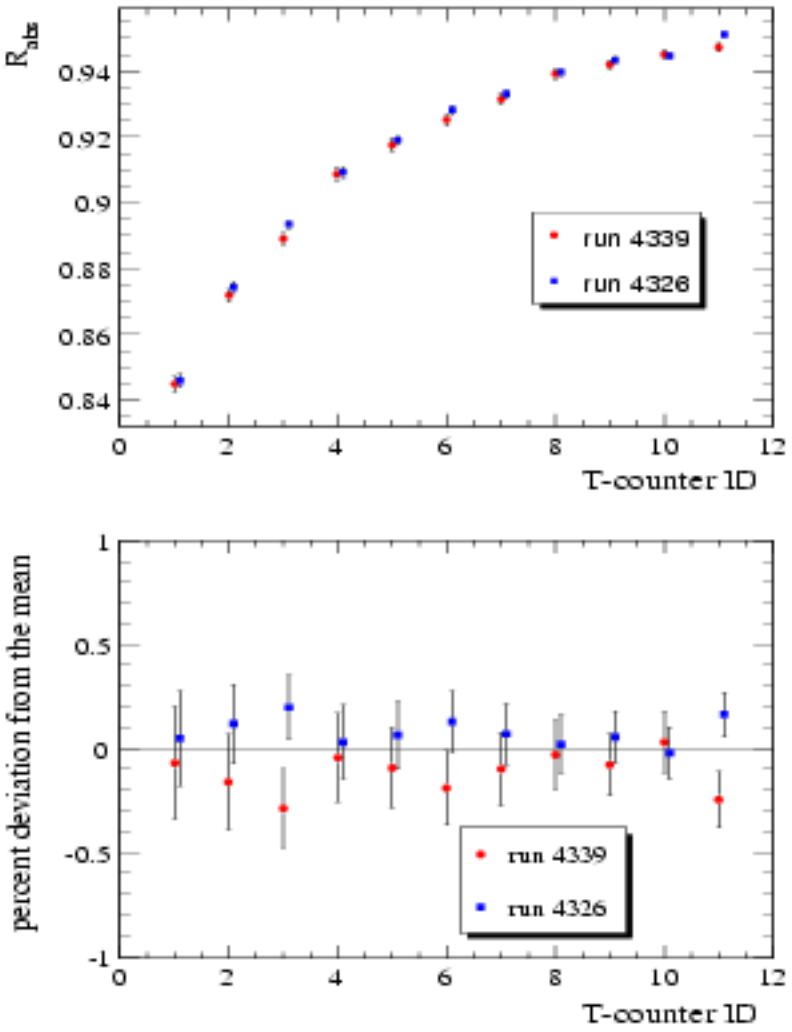

Figure 61: (top) R_{abs} measured for two runs which were taken with different settings of the PS dipole magnet. (bottom) Percent deviation from the mean value.

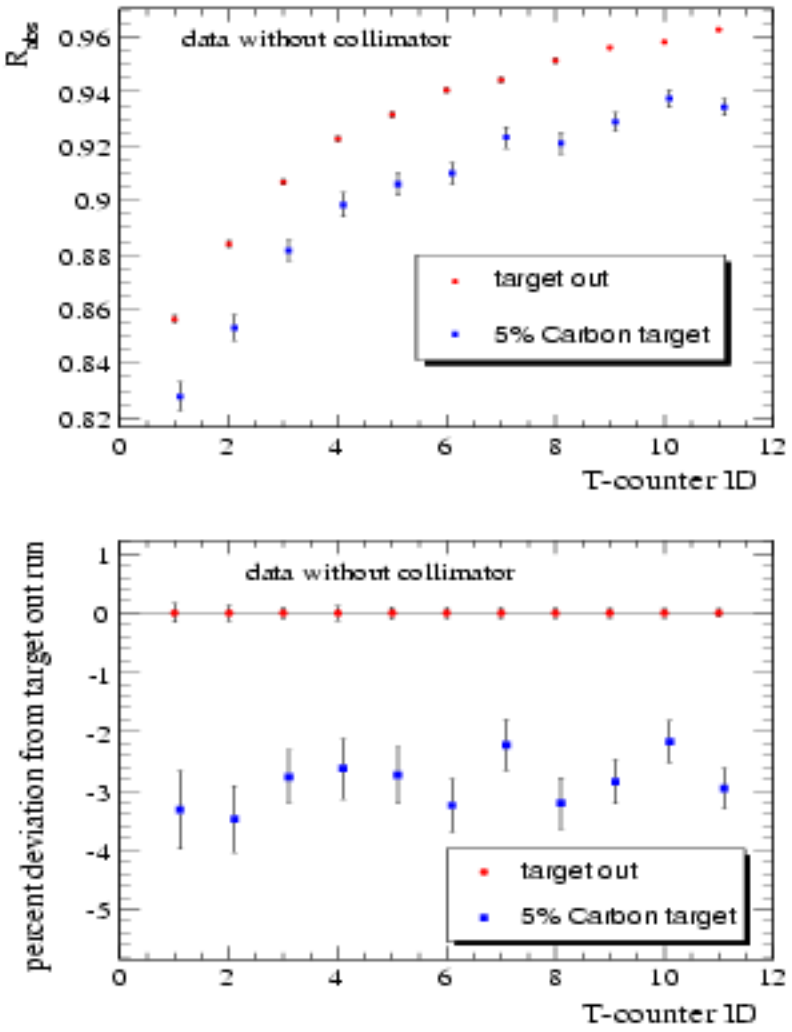

Figure 62: (top) R_{abs} measured for runs which were taken with target in and target out. (bottom) Percent deviation from the measurement obtained with physics target out; no photon collimation.

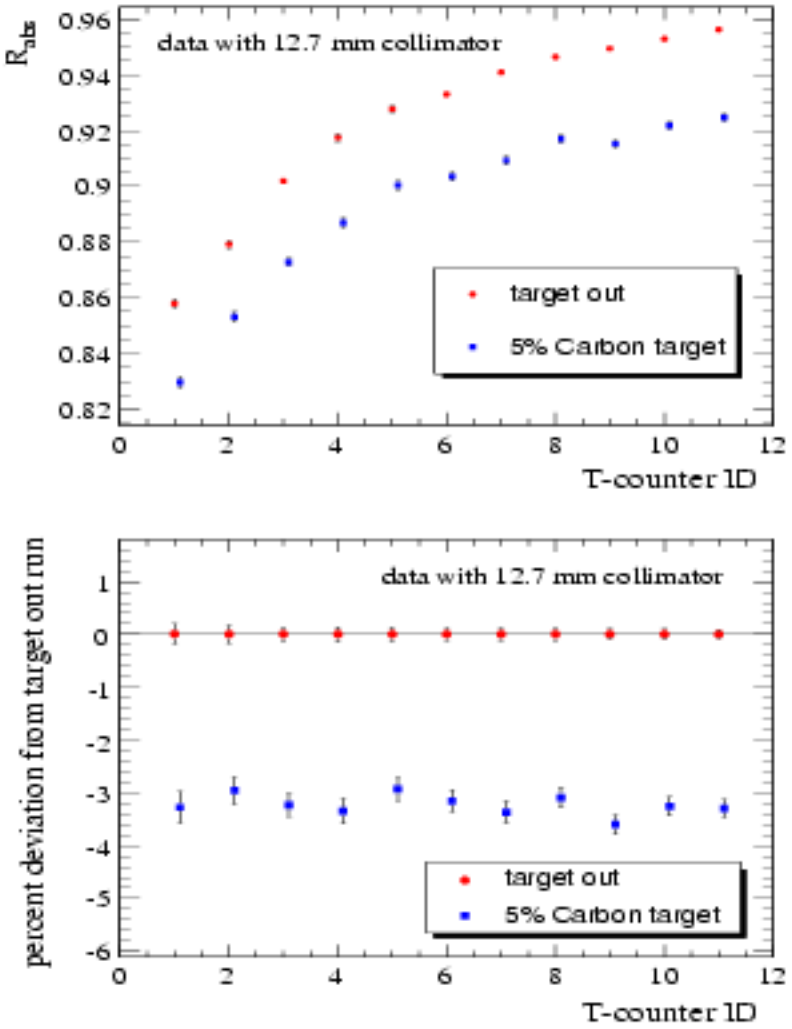

Figure 63: (top) R_{abs} measured for runs which were taken with target in and target out. (bottom) Percent deviation from the measurement obtained with physics target out; with photon collimation.

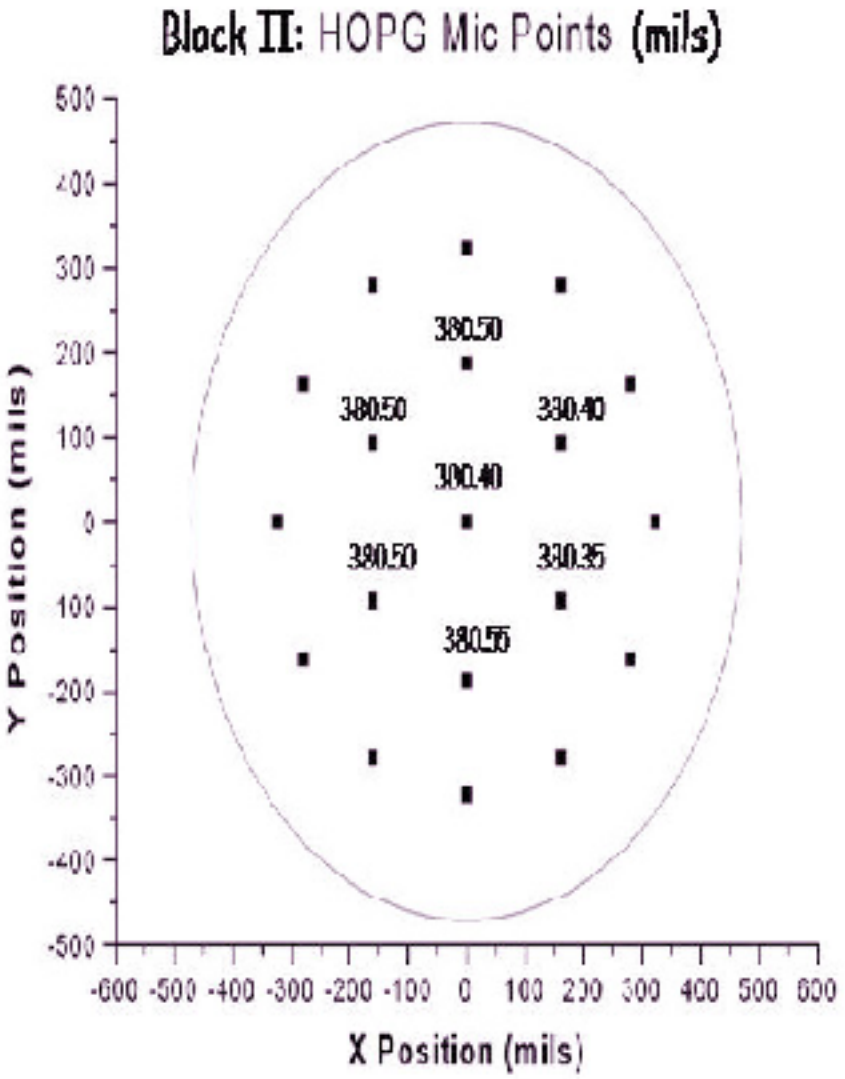

Figure 64: Thicknes map of the HOPG target. Units are in mils.

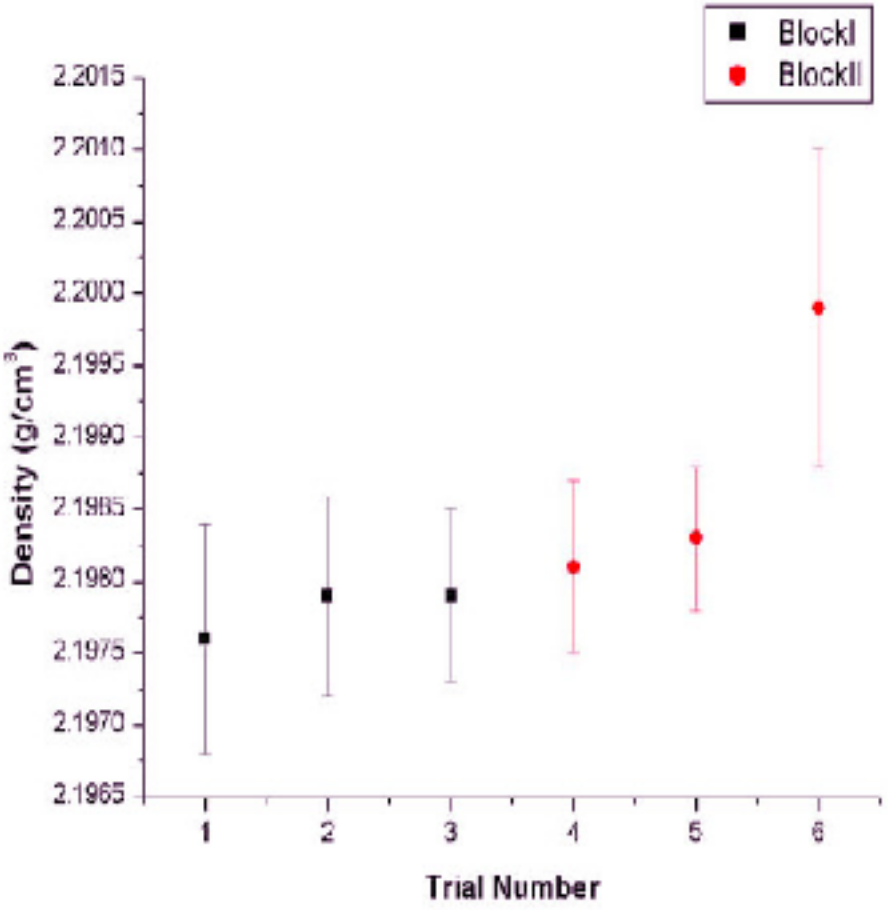

Figure 65: HOPG density measurements.

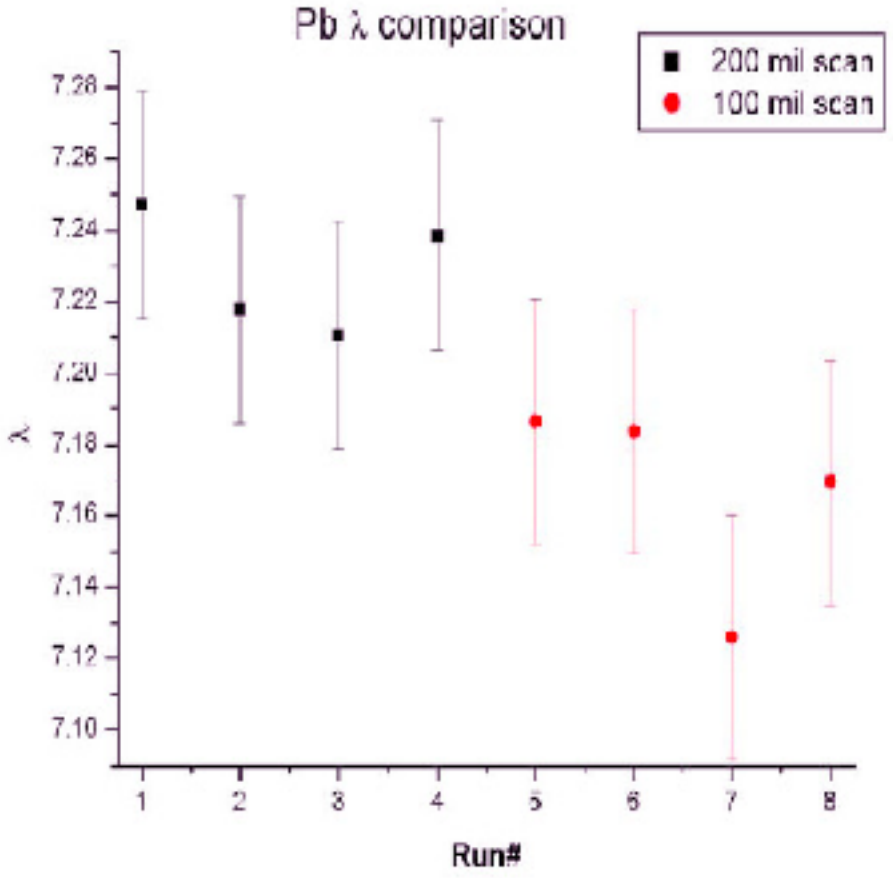

Figure 66: Measured x-ray absorption constants for the lead target.

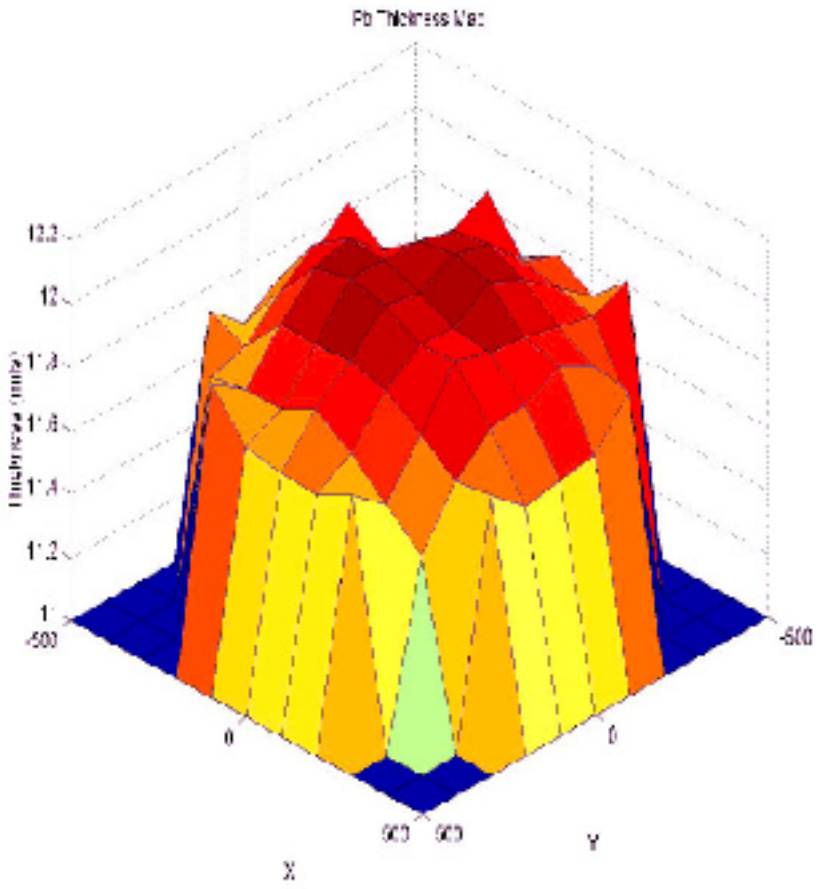

Figure 67: Lead target thickness map measured on a 100 mil grid.

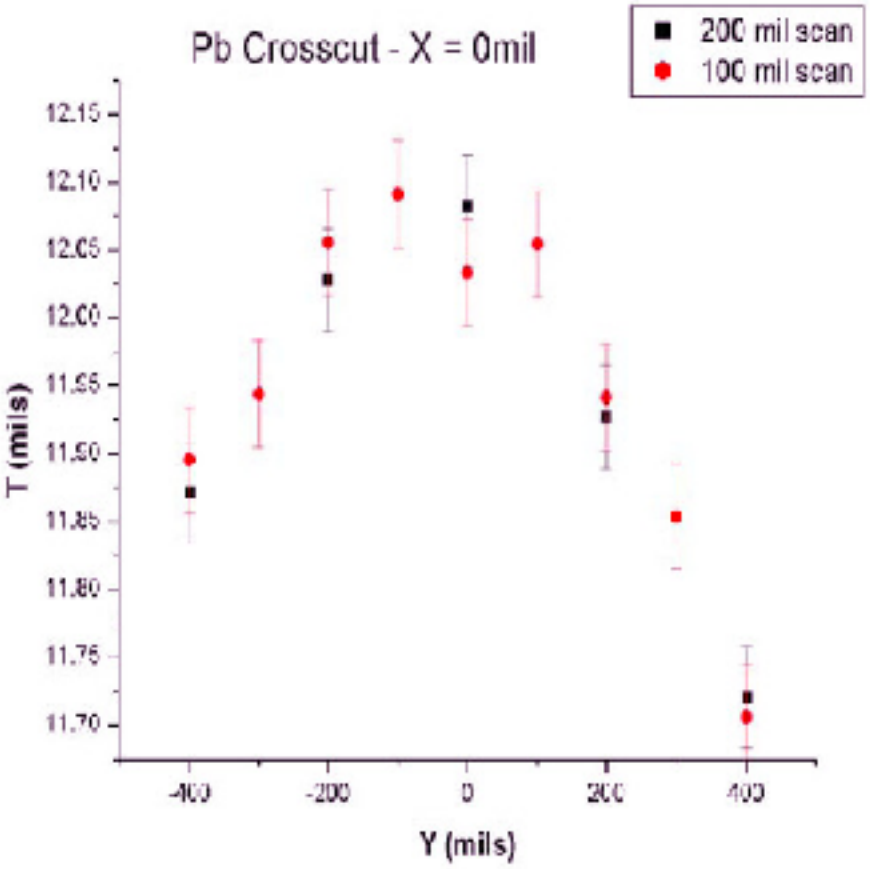

Figure 68: Crosscut of the lead target along the y axis.

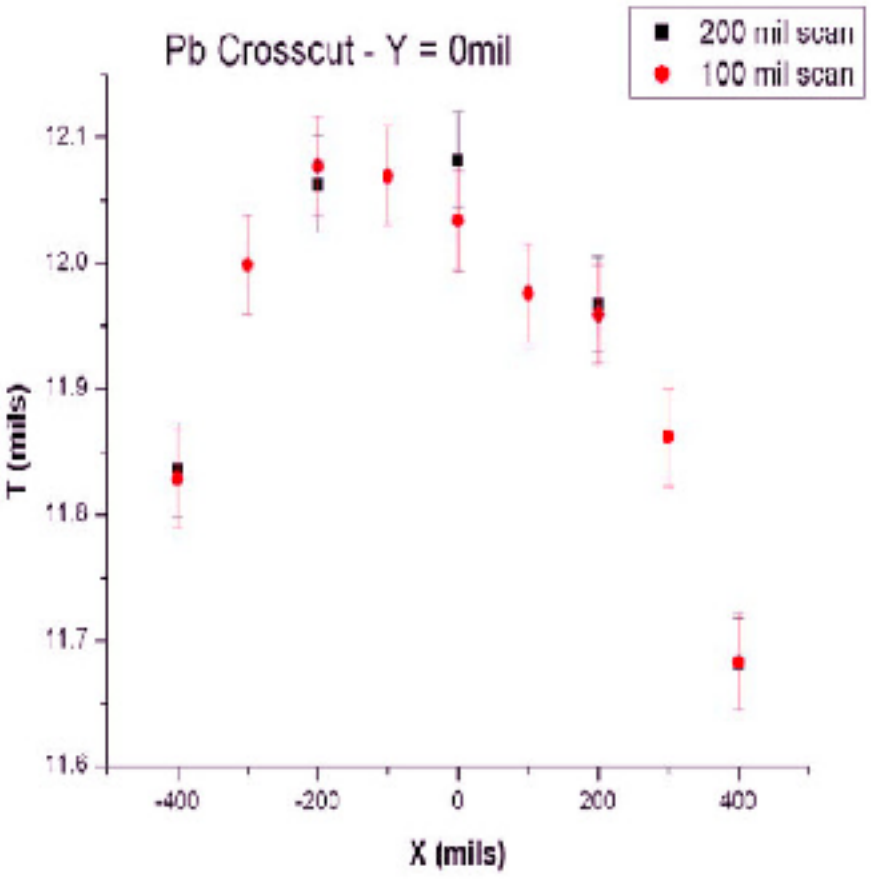

Figure 69: Crosscut of the lead target along the x axis.